Review Vol. 10, No. 1 / March 2018 / Advances in Optics and Photonics 43

Advances in Optics and Photonics

AlGaN photonics: recent advances in materials and ultraviolet devices

DABING LI,[1,*] KE JIANG,[1,2] XIAOJUAN SUN,[1] AND CHUNLEI GUO[3,4]

[1]State Key Laboratory of Luminescence and Applications, Changchun Institute of Optics, Fine Mechanics and Physics, Chinese Academy of Sciences, Changchun 130033, China
[2]University of Chinese Academy of Sciences, Beijing 100039, China
[3]The Guo China-US Photonics Laboratory, Changchun Institute of Optics, Fine Mechanics and Physics, Chinese Academy of Sciences, Changchun 130033, China
[4]The Institute of Optics, University of Rochester, Rochester, New York 14627, USA
*Corresponding author: lidb@ciomp.ac.cn

Received June 5, 2017; revised November 12, 2017; accepted November 14, 2017; published January 17, 2018 (Doc. ID 297047)

AlGaN-based materials own direct transition energy bands and wide bandgap and thus can be used in high-efficiency ultraviolet (UV) emitters and detectors. Over the past two decades, AlGaN-based materials and devices experienced rapid development. Deep ultraviolet AlGaN-based light-emitting diodes (LEDs) with improved efficiency of 20.3% (at 275 nm) have been produced. An electron beam (EB)-pumped AlGaN-based UV light source at 238 nm, output power of 100 mW, and power conversion efficiency (PCE) of 40% has also been fabricated. UV stimulated emission from AlGaN multiple-quantum-wells laser diodes (LDs) using electrical pumping at room temperature has also been achieved at a wavelength of 336 nm. Compared with GaN-based blue and green LEDs and LDs, the efficiency of AlGaN-based UV LEDs and LDs is lower. Further optimization and improvements in both structure and fabrication are required to realize high-performance devices. In AlGaN-based UV photodetectors (PDs), gain as high as 10^4 orders of magnitude has been reported using the separated absorption and multiplication region avalanche photodiode structure but is still far from detecting the weak signal, and thus UV single-photon detectors with high detectivity is challenging. Recently, there has been extensive work in the nonlinear optical properties of AlGaN and AlGaN-based passive devices, such as waveguides and resonators. However, how to minimize the scattering and defect-related absorption needs to be further studied. In this review, first, approaches used to grow an AlGaN epilayer and p-type doping are introduced. Second, progress in AlGaN-based UV LEDs, EB-pumped light sources, LDs, PDs, passive devices, and the nonlinear optical properties are presented. Finally, an overview of potential future trends in AlGaN-based materials and UV devices is given. © 2018 Optical Society of America

OCIS codes: (230.0250) Optoelectronics; (230.3670) Light-emitting diodes; (230.5160) Photodetectors; (140.2020) Diode lasers
https://doi.org/10.1364/AOP.10.000043

AlGaN photonics: recent advances in materials and ultraviolet devices

Dabing Li, Ke Jiang, Xiaojuan Sun, and Chunlei Guo

1. INTRODUCTION

UV radiation, which is an important component of solar radiation, can be divided into three bands, comprising the UV-A band (320–400 nm), the UV-B band (280–320 nm), and the UV-C band (100–280 nm). UV radiation affects not only the survival and continuing development of humankind, but also has a variety of important applications, including high-resolution light sources, phototherapy, disinfection, sterilization, deodorization, organic decomposition, photo catalysis, gas sensing, optical dialysis dosage monitoring, and the identification of hazardous biological agents. Due to the outstanding optoelectronic properties in the UV band and deep ultraviolet (DUV) band, AlGaN material has received extensive attention recently.

As the ternary alloy of GaN and AlN material, AlGaN has a similar crystal structure as GaN and AlN, namely wurtzite (WZ) structure, zinc blende (ZB) structure, and rock-salt structure, as shown in Figs. 1(a)–1(c), respectively. At room temperature (RT) and atmospheric pressure, WZ is the most stable AlGaN crystal structure, with hexagonal-close-packed metal atoms and nitrogen atoms nesting to each other. The atom layers are arranged as the sequence of ……AaBbAaBb….., as shown in Fig. 1(f). In the structure cell, each metal atom is located at the center of a regular tetrahedron and four nitrogen atoms are at the corresponding apexes, while each nitrogen atom is in the same structure as the metal atoms, respectively, as shown in Figs. 1(d) and 1(e). According to crystal lattice classification, the WZ structure belongs to the hexagonal crystal system with a space group of p63mc. There are two independent lattice constants, namely $\boldsymbol{a}$ and $\boldsymbol{c}$. The included angle between $\boldsymbol{a}$ axes is 120°, and that between the $\boldsymbol{a}$ axis and $\boldsymbol{c}$ axis is 90°. Additionally, the ideal lattice constant rate $\boldsymbol{c/a}$ equals to 1.633. Usually, the Vergard law as Eq. (1) shows is used to estimate the lattice constant of AlGaN material with the Al component of $\boldsymbol{x}$ [1]. The noncentrosymmetric structure and electronegativity difference between metal atoms in AlGaN crystal directly determine the optical, electrical, and optoelectronic properties:

$$a_{\mathrm{Al}_x\mathrm{Ga}_{1-x}\mathrm{N}} = a_{\mathrm{AlN}} \times x + a_{\mathrm{GaN}} \times (1 - x). \tag{1}$$

The crystal structure and electron configuration of a semiconductor material determine the energy band structure, and thus the optoelectronic properties and applications. Based on the crystal structure of WZ (Al)GaN, the energy band structures are shown in Fig. 2 [2,3]. The first Brillouin zone in reciprocal space of WZ AlGaN is displayed in Fig. 2(a). The axes $\boldsymbol{k_x}$, $\boldsymbol{k_y}$, and $\boldsymbol{k_z}$ are orthogonal to each other in reciprocal space and the special symbols stand for the highly symmetrical positions, where the electron behaviors like relaxation, scattering, and transition are closely related to the optoelectronic properties of the semiconductor materials. The band structure along the high-symmetry lines calculated by using the empirical pseudopotential method without considering the crystal-field effect and the spin-orbit coupling effect in the first Brillouin zone of GaN and AlN are exhibited in Figs. 2(b) and 2(c) [2].

As we can see, both GaN and AlN are direct bandgap materials, and the maximum energy of the valance band and minimum energy of the conduction band are both at the Γ point, namely the center of the first Brillouin zone. Generally, at RT, the energy bandgaps of GaN and AlN are 3.4 eV and 6.2 eV, respectively. In addition, Eq. (2) is always used to calculate the energy bandgap of AlGaN material with Al component of $\boldsymbol{x}$,

$$E_g(\mathrm{Al}_x\mathrm{Ga}_{1-x}\mathrm{N}) = E_g(\mathrm{AlN}) \times x + E_g(\mathrm{GaN}) \times (1-x) - b \times x \times (1-x), \quad \textbf{(2)}$$

where $E_g(\mathrm{Al}_x\mathrm{Ga}_{1-x}\mathrm{N})$, $E_g(\mathrm{AlN})$ and $E_g(\mathrm{GaN})$ stand for the energy bandgap of AlGaN, AlN, and GaN, and the bowing parameter $\boldsymbol{b}$ is experimentally determined [4]. Except for Γ valley, there are also minimal values such as A and M-L valleys in GaN and K and M-L valleys in AlN, respectively, between which the electron relaxation and scattering will significantly impact the electrical properties of (Al)GaN. Furthermore, as the noncentrosymmetry of the WZ (Al)GaN structure, there exists strong spontaneous and piezoelectric polarization, which induces a crystal-field split-off subband near the Γ point in the first Brillouin zone, as shown in Fig. 2(d) [3]. The symbol Δcr stands for the crystal-field split-off energy. As we can see, with increasing Al content from GaN to AlN, the Δcr changes from a positive value to a negative one. Additionally, when considering both crystal-field and spin-orbit coupling effects, the valance bands maximum of GaN and AlN split into three subbands, namely the heavy hole (HH), light hole (LH), and crystal-field split-off hole (CH) bands, as shown in Fig. 2(e) [3]. The symbol Δso stands for the spin-orbit coupling energy, namely the energy difference between the HH and LH bands. Conclusively, as shown in Fig. 2(f), when the centrosymmetric ZB structure changes into a noncentrosymmetric WZ structure within AlGaN, at the center of the first Brillouin zone, the triplet state Γ15 splits into a doublet state Γ6 and a singlet state Γ1, corresponding to HH, LH subbands and CH subband, respectively. Further, as the Al component increases, the CH subband shifts up while the HH and LH subbands shift down, relatively, and the corresponding Δcr changes from a positive value to a negative one, respectively. Later, it will be found that this subband structure can

Figure 1

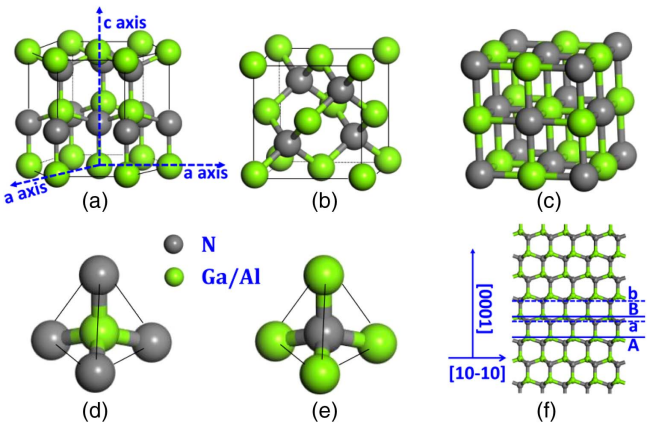

(a) Wurtzite structure, (b) zinc blende structure, and (c) rock-salt structure of AlGaN. (d) Metal atoms locate at the center of a regular tetrahedron, and four nitrogen atoms are at the corresponding apexes. (e) Nitrogen atoms locate at the center of a regular tetrahedron, and four metal atoms are at the corresponding apexes. (f) The arrangement of atoms along the [0001] direction.

considerably influence the AlGaN-based light-emitting devices. Some physical constants of GaN and AlN are listed in the following Table 1; the counterparts of AlGaN materials can refer to the values in the table to some degree.

Taking the advantages of AlGaN materials of the direct wide bandgap character, great progress has been made in UV optoelectronic active devices, such as LEDs, EB-pumped light sources, LDs, and PDs, using AlGaN materials. Additionally, based on the noncentrosymmetric crystal structure of WZ AlGaN, passive nonlinear optical devices, such as optical limiters [10], ultrafast nonlinear autocorrelation systems [11], and all-optical switchings [12], also attract much more attention. Compared with traditional solid-state light sources, AlGaN-based UV-LEDs have numerous advantages, including short wavelength operation, small size, compact structure, operational stability, high efficiency, low power consumption, low operating voltage, environmental

Figure 2

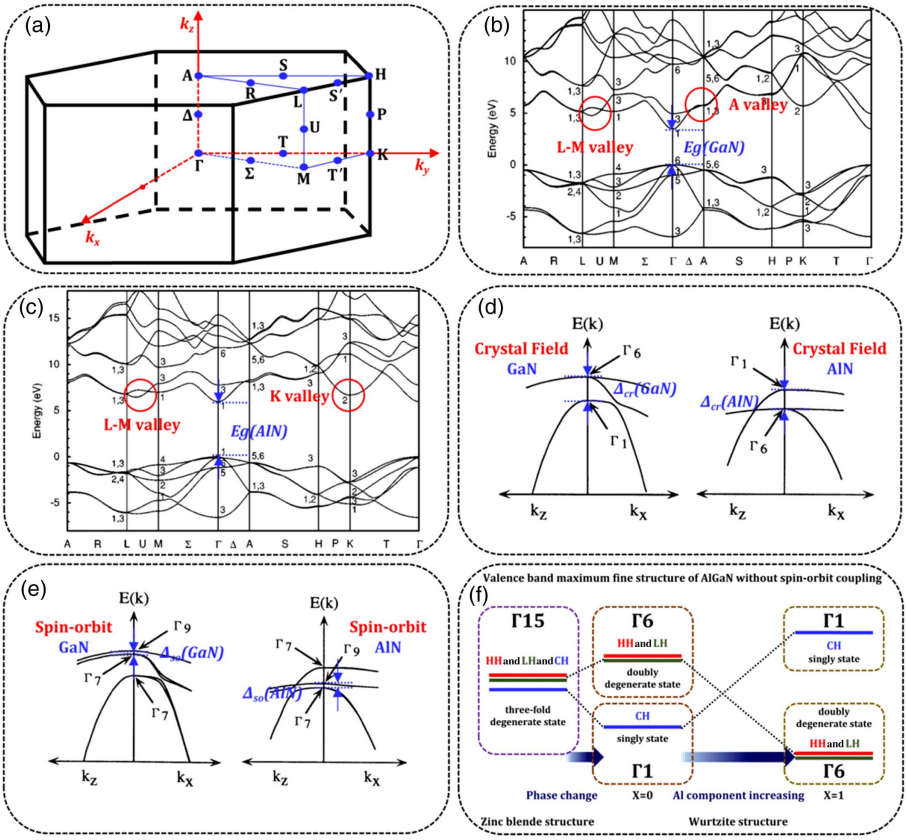

(a) First Brillouin zone in reciprocal space for the WZ AlGaN structure. (b) and (c) are the band structure along high-symmetry lines calculated by using the empirical pseudopotential method (EMP) without considering the crystal-field effect and the spin-orbit coupling effect in the first Brillouin zone of GaN and AlN. Figure 5 reprinted with permission from Fritsch *et al.*, Phys. Rev. B **67**, 235205 (2003). Copyright 2003 by the American Physical Society. (d) The valence band maximum of GaN and AlN without considering spin-orbit coupling effects. (e) The valence band maximum of GaN and AlN considering both the crystal-field and spin-orbit coupling effects. Figure 6 adapted with permission from Suzuki *et al.*, Phys. Rev. B **52**, 8132–8139 (1995). Copyright 1995 by the American Physical Society. (f) The valence band maximum changes as the Al content increases.

Table 1. Basic Physical Constants of GaN and AlN

Physical Constants	Units	GaN		AlN		Refs.
Space group	–	$C_{6V}^4P6_3mc$		$C_{6V}^4P6_3mc$		–
Lattice constants (a)	nm	3.189		3.112		[5]
Lattice constants (c)	nm	5.158		4.982		
Bandgaps ($T = 300$ K)	eV	3.4		6.2		
Electron effective masses	m_0	0.18		0.27		[3]
Hole effective masses	m_0	$m_{hh}^{\perp}$	1.61	$m_{hh}^{\perp}$	10.42	
		$m_{lh}^{\perp}$	0.14	$m_{lh}^{\perp}$	0.24	
		$m_{\text{split}}^{\perp}$	1.04	$m_{\text{split}}^{\perp}$	3.81	
		$m_{hh}^{\parallel}$	1.76	$m_{hh}^{\parallel}$	3.53	
		$m_{lh}^{\parallel}$	1.76	$m_{lh}^{\parallel}$	3.53	
		$m_{\text{split}}^{\parallel}$	0.16	$m_{\text{split}}^{\parallel}$	0.25	
Δso	meV	0.008		0.019		[6]
Δcr	meV	10		−169		[7]
Raman shift peak E_2 (high) position ($T = 300$ K)	cm^{-1}	567		657		[8]
Static dielectric constants		8.9		8.5		[9]
Elastic coefficients c_{33}	GPa	398		373		[5]
Elastic coefficients c_{31}	GPa	106		108		
Spontaneous polarization coefficients	C/m^2	−0.029		−0.081		
Piezoelectric polarization coefficients e_{33}	C/m^2	0.73		1.46		[9]
Piezoelectric polaroid coefficients e_{31}	C/m^2	−0.49		−0.60		

friendliness, and long lifetimes, which make them suitable for application in the UV radiation field. EB-pumped AlGaN-based UV light sources have simple structures without a p-type layer, which allows them to bypass the difficulties of p-type doping of AlGaN. It is thus possible to realize DUV light sources with high power and high efficiency because of their low resistance. AlGaN-based UV-LDs with their unique high spatial and temporal coherence properties have many merits, including high light beam quality, high power density, and high modulation speeds, which can be widely used in applications of precision laser processing, high-density data storage, nanopattern-type photolithography, medical diagnostics, disinfection, biochemical technology, gas sensing, and materials science. AlGaN-based UV-PDs, which offer the advantages of small size, stable operation, low operating voltages, high sensitivity, high efficiency, and the ability to function in solar-blind regions, can be applied in both military and civilian fields like early missile warning, non-line-of-sight communications, fingerprint identification, flame detection, and environmental monitoring. The applications of nonlinear optical devices based on AlGaN materials are still limited due to the low AlGaN quality and the comparatively weak nonlinear optical effects. However, as the improvement of AlGaN crystalline quality and the UV active devices especially the light-emitting devices with high output power, the application field of AlGaN-based nonlinear optical devices will become wider.

Though AlGaN-based UV devices have bright prospects for use in these applications, there are still numerous challenges in both material growth and device fabrication. First, it is difficult to obtain high-quality AlGaN material, and the crystalline quality of the material deteriorates with increasing Al content. The main reasons for the poor crystalline quality are a lack of lattice-matched substrates for growth and the presence of pre-reactions or parasitic reactions between the trimethylaluminum (TMAl) precursors and NH_3 used in growth of the material. Second, it is difficult to achieve high p-type conductivity in Mg-doped AlGaN because of the material's strong self-compensation effect, low solubility, and high activation energy [13–17]. Additionally, the difficulties with AlGaN materials lead to poor performance in AlGaN-based UV devices.

In the following sections, as shown in Fig. 3, four main parts will be reviewed. The approaches that have been used to improve the crystalline quality and p-type doping

efficiency of AlGaN materials are introduced. Subsequently, the energy band structures, optical anisotropy properties of AlGaN materials, and the current research progress in AlGaN-based UV devices, including LEDs, EB-pumped light sources, LDs and PDs, are presented. Moreover, as attention to nonlinear optical properties and passive devices of AlGaN increases, the research progress in this field is involved. Finally, an overview of the future trends in AlGaN UV devices is provided.

2. IMPROVEMENT OF ALGAN QUALITY

The first report on the properties of bulk crystalline AlN was published in 1960 [18], and the AlN film was first demonstrated in 1964 [19]. The original techniques used for AlN epitaxial growth included hydride vapor phase epitaxy (HVPE) and reactive sputtering. The substrates that were used included sapphire, Si, SiC, and quartz. In 1971, the metalorganic compound TMAl was first used to prepare AlN by metalorganic chemical vapor deposition (MOCVD) [20]. In 1976, the direct current (DC) UV electroluminescence of low-resistivity n-type AlN films was first observed, with its broad emission range extending from 215 nm into the blue end of the spectrum [21].

AlGaN films were first grown to serve as buffer layers for the growth of GaN or AlN epilayers [22,23]. Subsequently, the use of AlGaN was attempted in p-type doping applications because of the difficulties of p-type doping in GaN and AlN [24]. As a result, it became possible to achieve effective radiative recombination in the UV bands using n- and p-type AlGaN films. Following the progress in epitaxial techniques, the quality of the AlGaN films was improved by adopting molecular beam epitaxy (MBE) [25] and MOCVD techniques [26]. Additionally, the quality of AlGaN films grown on

Figure 3

Diagram of the review. AlGaN growth methods, doping methods, devices, and nonlinear optical properties will be introduced. SL-D, CO-D, δ-D, PI-D, and 3D-D mean superlattices doping, codoping, δ-doping, polarization-induced doping, and three-dimensional doping. 2-NL-M, 3-NL-M, and EN-NL mean second-order nonlinear coefficients measurements, third-order nonlinear coefficients measurements, and the method of enhancing nonlinear optical effects of III-N. The surrounding pictures depict the representative information.

sapphire substrates by MOCVD was improved through use of AlN as a buffer layer in 1988 [27]. In 1990, GaN/AlGaN heterostructures were prepared on sapphire substrates by MOCVD at atmospheric pressure, and the surface morphology of the GaN/AlGaN heterostructure was investigated in an attempt to achieve crack-free surfaces [28].

Dislocations usually act as the nonradiative recombination center in AlGaN-based active devices, thus the quality of AlGaN is crucial to the device performance. Figure 4 illustrates the relationship between the internal quantum efficiency (IQE) and the dislocation density (DD) in AlGaN multiple quantum wells (MQWs) under weak excitation with an excess carrier density of 1×10^{18} cm^{-3} [29]. According to Fig. 4, the IQE is lower than 5% when the DD is higher than 10^{10} cm^{-2}, but the IQE exceeds 60% if the DD is lower than 10^{8} cm^{-2}. It is particularly difficult to obtain high-quality AlGaN materials, and the crystalline quality tends to deteriorate with increasing Al content [30]. On the one hand, the Al atom has a high adhesion coefficient and a low surface migration velocity, which introduces three-dimensional (3D) island-like growth modes and results in high DD levels in AlGaN epilayers. On the other hand, the presence of pre-reactions or parasitic reactions between TMAl and NH_3 also results in high DD levels and a reduction in AlGaN quality.

AlN is a proper substrate for AlN or AlGaN growth though GaN substrate is available in the market. The reasons are as follows: (1) GaN substrate is not so good for the growth of AlGaN because the AlGaN will endure the tensile stress on the GaN substrate; (2) AlN has a wider bandgap and lower absorption than GaN, and AlGaN grown on AlN has an atomically flat surface without pitting [31]. However, bulk AlN substrates with large diameters are not currently available for commercial applications. In 2013, a freestanding AlN single crystal was grown in a radio-frequency-heated furnace by physical vapor transport (PVT), and high-quality bulk AlN was produced with low defect densities [etch pit density (EPD) ≤ 100 cm^{-2} at the center, and EPD $\approx 10^{4}$ cm^{-2} at the edge], but the crystal size was small (10 mm $\times$ 10 mm $\times$ 12 mm) [32]. Later, various research organizations [32–38] had reported their progress made in the growth of bulk AlN and 50 mm (2 inch) bulk AlN with DD as low as 10^{3} cm^{-2} had been obtained by HEXATECH INC using PVT [36]. Since AlN bulk substrate with large area is hard to fabricate, AlN templates attract more attention as the substitution, which can be grown on sapphire substrates by HVPE [39,40] and MOCVD [41,42].

Figure 4

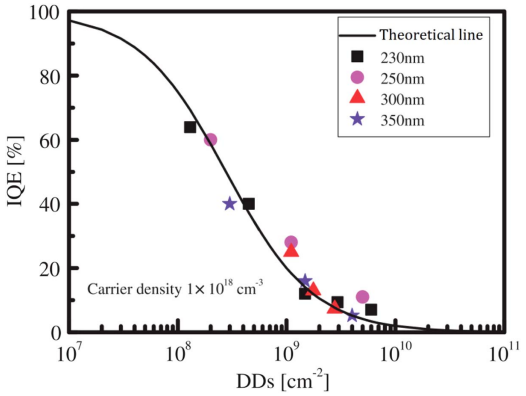

IQE as a function of DD in an underlying layer under weak excitation with excess carrier density of 1×10^{18} cm^{-3}. Reprinted from Ban *et al.*, Appl. Phys. Express **4**, 052101 (2011). © IOP Publishing. Reproduced with permission. All rights reserved.

Table 2. Recent Progress in AlN and AlGaN Growth Quality

Organizations	Techniques	Material	XRD (arc sec)	DD (cm^{-2})	Year	Refs.
Leibniz Institute for Crystal Growth (IKZ), Germany	PVT	Bulk AlN 10 mm × 10 mm × 12 mm	(0002): 21	Center: 100 Edge: 10^4	2013	[32]
North Carolina State University, USA	PVT	Bulk AlN 10–15 mm	(0002): 12 (10–12): 22	$<10^4$	2011	[33,34]
Ludwig Maximilians University, Germany	PVT	Bulk AlN 28 mm	(0002): 72 (10-13): 200	$2–5 \times 10^5$	2013	[35]
HEXATECH INC.	PVT	Bulk AlN 50 mm	(0002): <100	10^3	2017	[36]
Ioffe Physical-Technical Institute, Russia	Sublimation sandwich method (SSM)	Bulk AlN 50 mm	(0002): 70–120	10^4	2013	[37]
Crystal IS, Inc., USA	Sublimation- recondensation technique	Bulk AlN 50 mm	(0002): 28 (10–12): 32	$<10^4$	2008	[38]
Nitride Solutions Inc., USA	On sapphire substrate, by HVPE	AlN	(0002): 130 (10–12): 516	2.95×10^9 (Calculated by XRD)	2015	[40]
Mie University, Japan	On annealed AlN/sapphire template	AlN	(0002): 16 (10–12): 154	4.7×10^8 (by TEM)	2016	[41]
	On grooved AlN/sapphire template by ELOG	AlN	(0002): 148 (10–10): 385	5×10^7	2011	[60]
	Annealing of sputtered AlN/sapphire substrate	AlN	(0002): 49 (10–12): 287	9.2×10^8 (Calculated by XRD)	2016	[61]
Sensor Electronic Technology, Inc, USA	On grooved AlN/sapphire template by MEELOG	AlN	(0002): 157 (10–12): 291	2.6×10^8	2008	[62]
RIKEN, Japan	On patterned Si	AlN	(0002): 620 (10–12): 1141	$10^8–10^9$	2016	[63]
Institute of Semiconductors, China	On NP AlN/sapphire template by ELOG	AlN	(0002): 69.4 (10–12):319.1	1.1×10^9 (Calculated by XRD)	2014	[64]
Peking University, China	On NPSS	AlN	(0002): 171 (10–12): 205	3.2×10^8	2016	[65]
Ferdinand-Braun-Institute, Germany	On grooved AlN/sapphire template by ELOG	AlN	(0002): 180 (30–32):310	Below 10^9	2012	[66]
	On *ex situ* nanopatterned SiN_X/AlN/sapphire substrate, by ELOG	AlN	(0002): 125 (30-32): 325	Below 10^9	2013	[67]
University at Ulm, Germany	On *in situ* nanopatterned SiN_X/AlN/sapphire substrate, by ELOG	AlGaN	(0002): 260 (10–12): 685	4.9×10^9 (Calculated by XRD)	2011	[68]
	On sapphire substrate by two-step process	AlN	(0002): 92 (10–12): 1162	1×10^{10}	2015	[45]
CIOMP, CAS, China	On sapphire substrate by two-step growth	AlN	(0002): 60 (10–12): 550	3.4×10^9 (Calculated by XRD)	2013	[44]
Georgia Institute of Technology, Arizona State University, USA	On sapphire substrate by three-step growth	AlN	(0002): 280 (10–12): 480	Total DD: 2.5×10^9	2015	[46]
City University of New York, Texas Tech University, USA	On sapphire substrate by three-step growth	AlN	(0002): 280 (10–12): 480	2×10^9	2012	[47]
Meijo University, Japan	On NCC-SS combining three-step mehtod	AlN	(0002): 50 (10–12): 250	0.8×10^9 (XRD) 2×10^9 (TEM)	2017	[48]
University College Cork, Ireland	On self-assembled patterned AlN-nanorod/ sapphire, by ELOG	AlN	—	3.5×10^8	2015	[69]

HVPE with a higher growth rate than MOCVD is more appropriate for the growth of thicker AlGaN films. However, it is more difficult to control the stress in an AlGaN film grown by HVPE than by MOCVD. Additionally, both a precursor of hydrogen chloride (HCl) gas and its resultants such as AlCl or $AlCl_3$ in HVPE can react with quartz (SiO_2) in the growth chamber, which will reduce the quality and increase the background dopant concentration in AlN [43], though the more chemically active AlCl can be effectively controlled by proper temperature. Additionally, many other approaches, including two-step growth [44,45], three-step growth [46–48], interlayer [30], high-temperature (HT) growth with modulation of the V/III ratio [49–51], pulsed atomic layer epitaxy (PALE) [52], migration-enhanced epitaxy (MEE) [53], modified MEE [54], ammonia (NH_3) pulse-flow multilayer growth [55,56], use of a superlattice (SL) as a dislocation filter [57–59], and epitaxial lateral overgrowth (ELOG), have been tried by MOCVD in attempts to improve the quality of the resulting AlN or AlGaN. At present, ELOG combined with HT *ex situ* annealing is believed to be the most realistic and effective approach for the growth of AlN or AlGaN layers on AlN/sapphire templates. The progress in the growth of high-quality AlN and AlGaN made by various research organizations in recent years is summarized in Table 2. In addition, the relative development levels of different methods can be seen in Fig. 5.

Two-step growth, also called high-low temperature, is an effective technique to improve the quality of AlN grown on a sapphire substrate. The first step is to deposit low-temperature (LT) AlN as a nucleation layer, and the second step is to grow a HT AlN epilayer. The mechanism is to realize a transition from 3D growth to two-dimensional (2D) growth, so the dislocations can be effectively reduced by bending and annihilating during their propagation along the growth direction. The schematic of two-step growth is shown in Fig. 6 [44].

Three-step growth is a developed technique based on two-step growth. The structure of three-step growth includes a LT AlN nucleation layer, a middle temperature (MT) AlN intermediate layer, and a HT epilayer. The function of the intermediate layer grown at MT is to promote 2D growth, prevent surface pits from uncoalesced islands and reduce edge dislocation [46,47]. Recently, Yoshikawa *et al.* reported a three-step

Figure 5

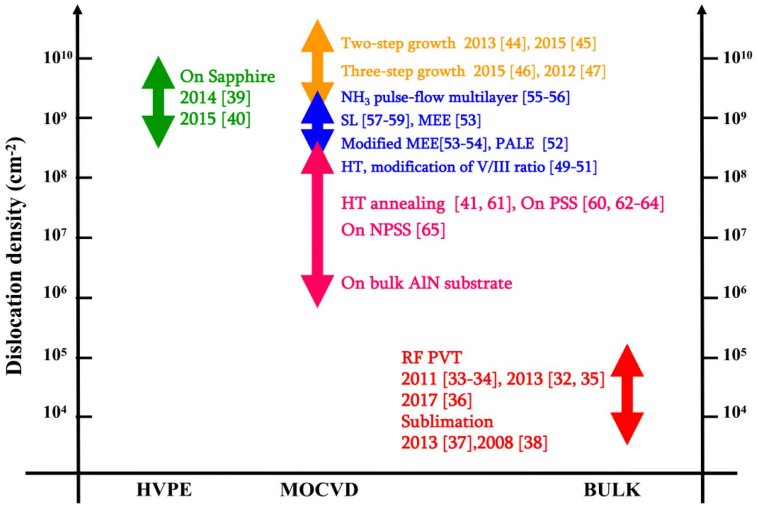

Progress in low DD AlN development using the techniques of HVPE, MOCVD, PVT, and sublimation [32–41,44–47,49–65].

growth method combining a randomly distributed nanosized concavo-convex sapphire substrate (NCC-SS) for fabrication of high-quality AlN film. The x-ray diffraction (XRD) results for their AlN films are 50 arc sec and 250 arc sec for (0002) and (10-12) planes, respectively [48].

Many effects have been made to improve the quality of AlN and AlGaN, especially for the AlGaN with high Al content. An interlayer is usually introduced and Fig. 7 shows the XRD (0002) FWHM as a function of AlN molar fraction (x) in an $Al_xGa_{1-x}N$ epilayer with and without an interlayer [30]. It can be seen that the interlayer technique is an effective way to reduce the defects in AlGaN. Furthermore, the technique of HT growth with modulation of V/III ratio is adopted to improve the quality of AlN grown

Figure 6

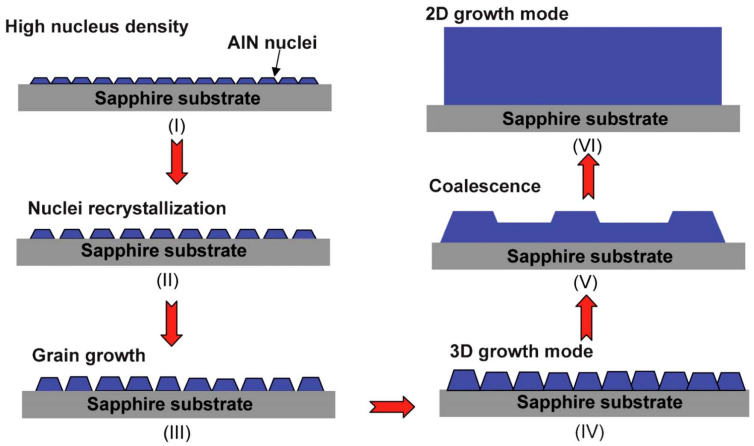

Schematic of two-step growth. Reprinted from [44] with copyright permission.

Figure 7

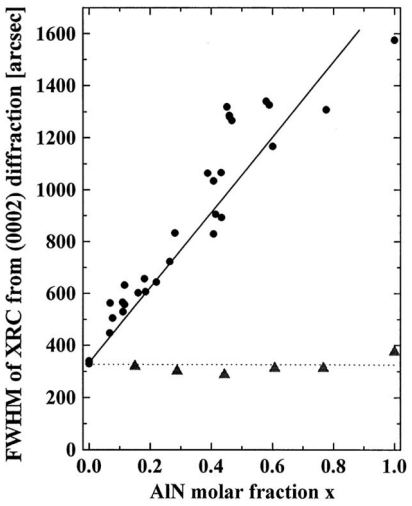

XRD (0002) FWHMs as a function of AlN molar fraction (x) in $Al_xGa_{1-x}N$, where closed triangles represent the structure with interlayer and closed circles represent the structure without interlayer [30]. Reprinted from J. Cryst. Growth **223**, Kamiyama *et al.*, "Low-temperature-deposited AlGaN interlayer for improvement of AlGaN/GaN heterostructure," 83–91. Copyright 2001, with permission from Elsevier.

on a sapphire substrate by MOCVD [49–51]. The HT growth can promote Al adatom migration and thus high-quality AlN with an atomically flat surface can be achieved. However, the excessive HT will accelerate the dopants diffusion, and generate the instability and thermal damage of a sapphire substrate [70]. So the HT growth with modulation of V/III ratio is proposed to further improve AlN quality and reduce the side effect generated at HT.

In 2006, a 9 μm AlN was grown on a sapphire substrate using the HT growth of 1400°C and modification of V/III ratio by MOCVD, and high-quality AlN with atomically flat surface and DD less than 3×10^8 cm^{-2} was achieved. The resulting atomic force microscopy (AFM) images, growth flow models, and dislocation behavior of AlN for different periods of time are shown in Figs. 8(a)–8(c) [49]. In 2007, high-quality AlN with DD less than 10^6 cm^{-2} was achieved on a patterned SiC substrate using the HT growth of 1510°C and modification of V/III ratio by MOCVD that was capable of heating to a maximum temperature of 1800°C under nitrogen and hydrogen atmospheres. The dislocation evolution by changing V/III ratio was measured by transmission electron microscopy (TEM), as shown in Fig. 9 [50]. Many screw-type dislocations were annihilated by forming a loop structure [Fig. 9(a)], and some edge-type dislocations were annihilated with bundles or agglomerates [Fig. 9(b)]. Nevertheless, high quality of AlN is very dependent on high growth temperature.

PALE is an epitaxy technique with a constant supply of group III source and pulsed supply of group V source, which can promote Al adatom migration, so as to improve epitaxial quality and surface flatness of AlN. In 2002, the Khan group reported that ultra-high-quality AlN grown on a plane sapphire substrate by PALE was achieved, with strong band-edge RT photoluminescence (PL) of 208 nm, and (0002) and (11-24) FWHMs of 18 and 210 arc sec, respectively [52]. MEE is an epitaxy technique with

Figure 8

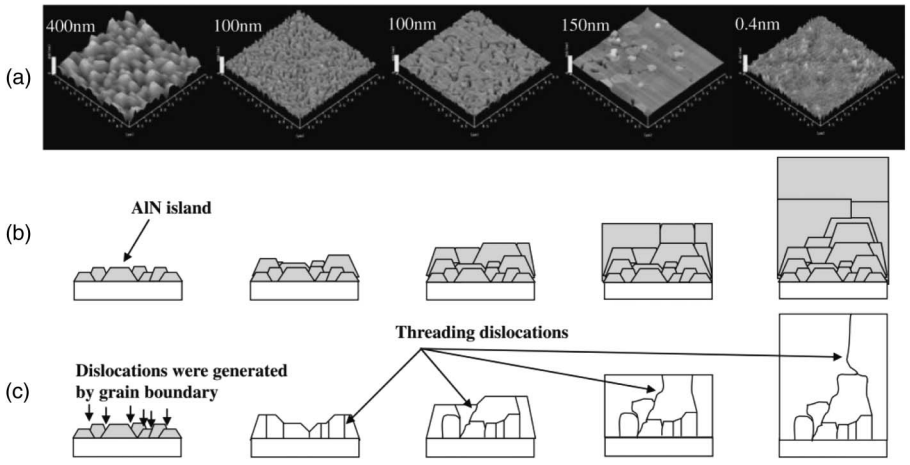

Resulting AFM images and models of growth flow and dislocation behavior of AlN for different periods of time. (a) AFM images of AlN grown for different periods of time. (b) Illustration of growth with time. Initially, AlN islands are formed that subsequently coalesce to form larger grains as the growth progresses. Ultimately, 2D growth results. (c) Formation of dislocations during growth. Initially, dislocations are generated at the points of coalescence of grains. The threading dislocations formed propagate vertically during growth and get annihilated at growth transition points [49]. Reprinted from Imura *et al.*, Jpn. J. Appl. Phys. **45**, 8639–8643 (2006). © IOP Publishing. Reproduced with permission. All rights reserved.

the separate supplies of group III and group V sources, which not only can promote Al adatom migration, but also can suppress gas phase reaction between group III and V sources by separating supplies. Modified MEE is characterized by the combination of a MEE and a simultaneous source supply [53,54]. In 2008, AlN with low DD was achieved by modified MEE based on MOCVD, with the FWHMs of XRD (002) and (102) diffractions of 45 arc sec and 250 arc sec, respectively. The growth sequences and surface morphologies of 600 nm AlN grown by the techniques of conventional MEE, modified MEE, and simultaneous supply are shown in Figs. 10(a)–10(c) [53]. These morphological characteristics resulted in the root-mean-square roughness of 0.12 nm for modified MEE, 0.35 nm for MEE, and 0.52 nm for the simultaneous supply. The schematics model of the initial AlN nucleation grown by the three growth modes are shown in Fig. 11 [53]. The initial nucleation occurs mostly along the step edges of the sapphire substrate for MEE, whereas random nucleation occurs both at

Figure 9

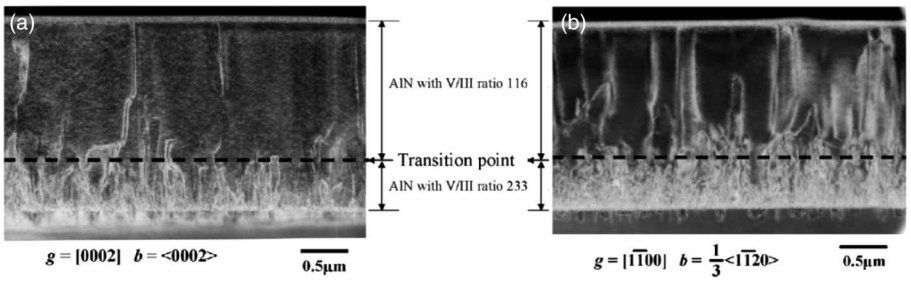

Dark-field cross-sectional TEM images of AlN grown by growth form modification taken under different diffraction conditions: (a) $g = [0002]$ and (b) $g = [1–100]$. The dotted line corresponds to the interface between the top AlN layer with V/III ratio at 116 and the underlying AlN layer [50]. Reprinted from J. Cryst. Growth **300**, Imura *et al.*, "Annihilation mechanism of threading dislocations in AlN grown by growth form modification method using V/III ratio," 136–140. Copyright 2007, with permission from Elsevier.

Figure 10

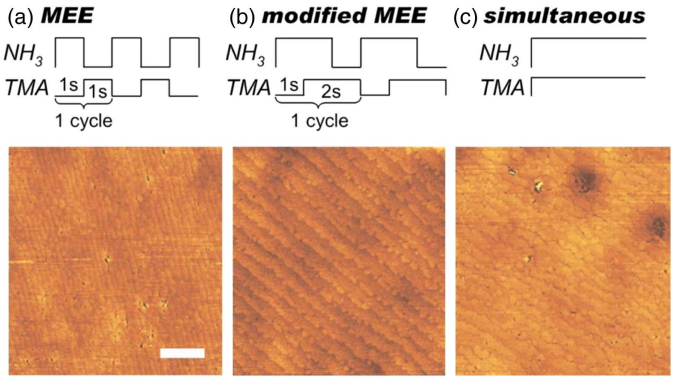

Growth sequences and surface morphologies of 600 nm AlN grown by the techniques of (a) conventional MEE, (b) modified MEE, and (c) simultaneous supply. All three images share the one scale bar, which represents 1 μm [53]. Reprinted with permission from Banal *et al.*, Appl. Phys. Lett. **92**, 241905 (2008). Copyright 2008 AIP Publishing, LLC.

the step edge and onto the terrace for simultaneous supply. So it is illustrated that modified MEE is more effective to improve AlN than MEE and simultaneous supply.

The technique of ammonia (NH_3) pulse-flow multilayer growth is another way to improve the AlN quality. High-quality AlN can be grown by the technique of NH_3 pulse-flow multilayer growth. NH_3 pulse-flow growth is to promote Al adatom migration and improve epitaxial quality and surface flatness of AlN. On the contrary, NH_3 continuous-flow growth is to keep continuous-flow for both NH_3 and group III source [55,56]. The gas flow sequence used for NH_3 pulse-flow growth and the schematic view of the growth control method using pulse- and continuous-flow gas feeding growth are shown in Fig. 12 [55]. In 2009, low threading dislocation density AlN template on a sapphire substrate was realized by using the NH_3 pulse-flow multilayer growth technique, and the edge-type and screw-type dislocation densities of the AlN layer were reduced to 7.5×10^8 cm^{-2} and 3.8×10^7 cm^{-2}, respectively.

Figure 11

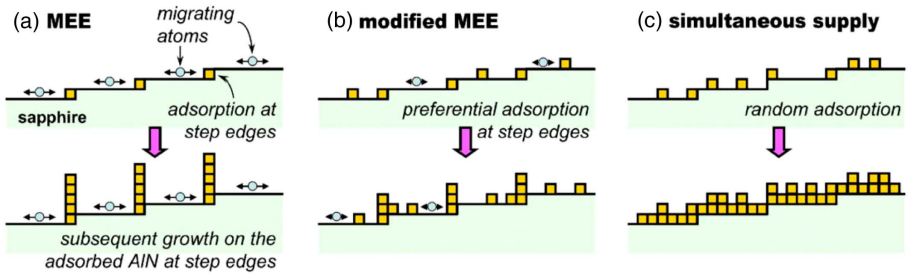

Schematic model of initial AlN nucleation on sapphire [53]. Reprinted with permission from Banal *et al.*, Appl. Phys. Lett. **92**, 241905 (2008). Copyright 2008 AIP Publishing, LLC.

Figure 12

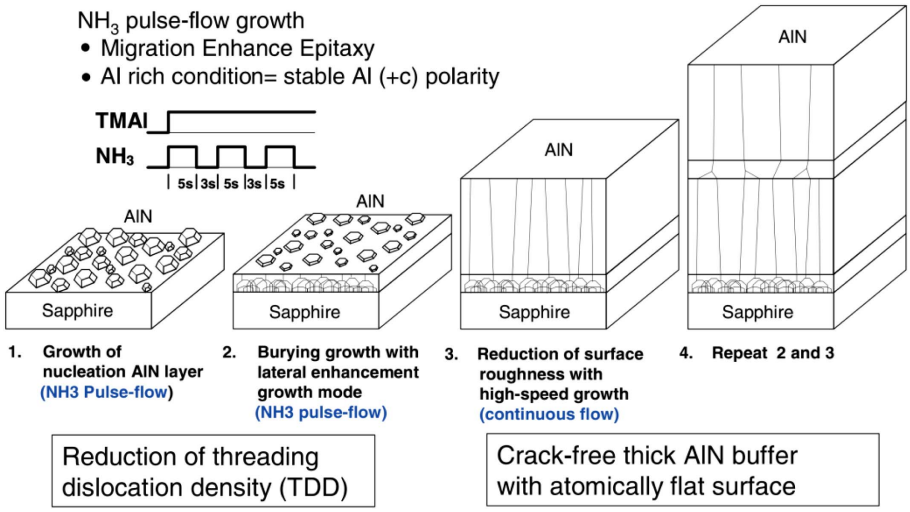

Gas flow sequence used for NH_3 pulse-flow growth, and schematic view of the growth control method using pulse- and continuous-flow gas feeding growth [55]. Hirayama *et al.*, Phys. Status Solidi A **206**, 1176–1182 (2009). Copyright Wiley-VCH Verlag GmbH & Co. KGaA. Reproduced with permission.

The SL insertion is also considered to filter dislocation and release the strain [57,58]. In 2005, AlN/AlGaN SLs by PALE as th dislocation filter were adopted to grow 1.0 μm AlN on a sapphire substrate, and high quality of $Al_{0.55}Ga_{0.45}N$ was achieved with screw dislocation density and edge dislocation density of 7×10^7 cm^{-2} and 3×10^9 cm^{-2}, respectively. The TEM images of revealing screw-type threading dislocations (TDs) for two 1.0 μm $Al_{0.55}Ga_{0.45}N$ layers grown on a high-quality AlN buffer with and without the SL insertion are shown in Fig. 13 [59].

ELOG is an effective way to reduce the DD and thus improve the epitaxial quality. ELOG of AlN is usually performed on patterned sapphire substrates (PSSs) and patterned (Al)GaN/sapphire templates. The ELOG technique promotes the development of AlGaN-based DUV devices. In 2011, an AlN template with a thickness of 8 μm was grown on a PSS by the ELOG technique, with the XRD (0002) and (10-10) FWHM of 148 arc sec and 385 arc sec, respectively. Using this AlN template, a high-performance DUV-LED was fabricated with an operating wavelength of 266 nm, output power of 5.3 Mw, and external quantum efficiency (EQE) of 1.9% at 60 mA DC [60]. In 2014, the quality of AlN was further improved by ELOG with XRD (0002) and (10-12) FWHM values of 69.4 arc sec and 319.1 arc sec, respectively. Based on this AlN, a 43% improvement in the IQE was achieved at a wavelength of 283 nm according to PL measurements [64]. In 2016, a 7.3 μm thick AlN layer was grown on nanopatterned AlN/sapphire substrates by the ELOG technique, and obtaining the AlN template with XRD (0002) and (10-12) FWHM values of 177 arc sec and 448 arc sec, respectively. And thus an optically pumped DUV-LD at RT was realized with an operating wavelength of 263.3 nm and an optical pump power threshold of 2.7 MW/cm^2 [71]. In 2016, very low dislocation of AlN was realized by ELOG on nanopatterned sapphire substrates (NPSSs). This template owns atomically flat surfaces with the XRD (0002) and (10-12) FWHMs of 171 arc sec and 205 arc sec, respectively, which can improve the performance of AlGaN-based DUV devices further. The surface of NPSSs and the cross section of AlN are shown in Fig. 14 [65].

Although nanopatterns can effectively improve AlN quality, it is extremely difficult to fabricate nanopatterned substrates. In addition, a nanorough surface is an alternative for ELOG of AlN. A nanorough surface can be fabricated by *ex situ* annealing at HT. So, ELOG of AlN can be grown on a nanorough AlN template, which is annealed in a carbon-saturated N_2–CO gas at extremely HT between 1500°C and 1800°C. AlN at HT suffers from recrystallization, which will provide a driving force to bend or annihilate the dislocations. Improved AlN quality was achieved by thermal annealing in

Figure 13

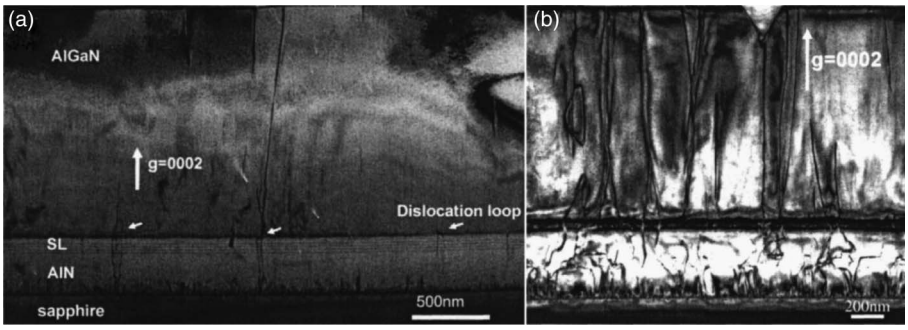

Cross-section TEM micrographs [$g = (0002)$] showing screw-type TDs in n-$Al_{0.55}Ga_{0.45}N$ (a) with and (b) without SLs insertion [59]. Reprinted with permission from Sun *et al.*, Appl. Phys. Lett. **87**, 211915 (2005). Copyright 2005 AIP Publishing LLC.

a carbon-saturated N_2–CO gas at 1700°C for 1 h, with XRD (0002) and (10-12) FWHMs from 532 arc sec to 49 arc sec and 6031 arc sec to 287 arc sec, respectively, for 170 nm AlN grown by sputtering [61], and from 180 arc sec to 68 arc sec and 1300 arc sec to 421 arc sec, respectively, for 300 nm AlN grown by MOCVD [41]. Figure 15 shows the AFM images of the surface morphologies of AlN with different annealing temperatures. Based on an annealed AlN template extremely high-quality AlN was obtained, with XRD (0002) and (10-12) FWHMs of 16 arc sec and 154 arc sec, respectively, which is the best result for AlN [41]. The improvement of AlN quality with thermal annealing can be explained that γ-AlON layer forms through the solid-state reaction between AlN and sapphire during the annealing. The schematic is shown in Fig. 16 [72].

3. ACHIEVEMENT OF HIGH-EFFICIENCY DOPING OF ALGAN

High-conductivity AlGaN is required to realize high performance AlGaN-based UV devices. However, it is difficult to achieve high-efficiency doping, particularly p-type

Figure 14

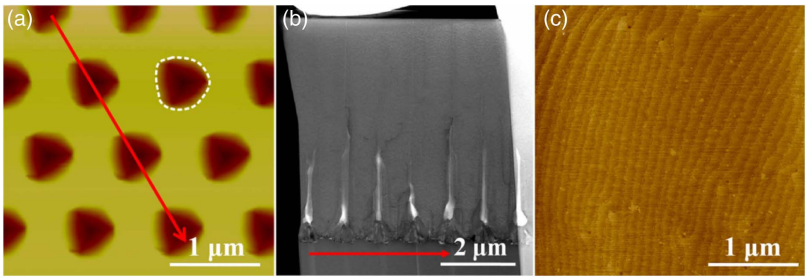

(a) AFM image of a typical NPSS (3 μm × 3 μm). (b) The cross-sectional STEM image for this chosen sample fabricated by focused ion beam. (c) A typical AFM image of the surface morphology of the AlN sample on NPSS with 650 nm holes patterns (3 μm × 3 μm) [65]. Reproduced from [65] under the terms of the Creative Commons Attribution 4.0 License. With copyright permission.

Figure 15

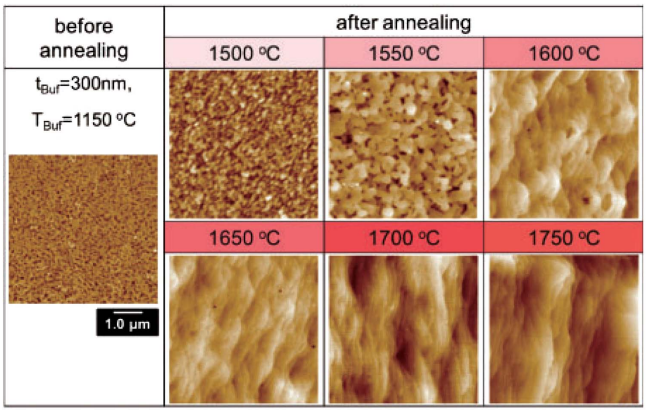

AFM images of 300 nm AlN grown at 1150°C before and after annealing. The scanning area in the AFM is 5 μm × 5 μm [41]. Reproduced from [41] under the terms of the Creative Commons Attribution 4.0 License. With copyright permission.

doping, which limits the application of DUV devices. It is therefore crucial to improve both the n-type and p-type doping efficiencies in AlGaN.

Realization of n-type doping is comparatively easier than p-type doping. The difficulty of n-type doping is mainly caused by scattering and self-compensation from defects. High-efficiency n-type doping can be achieved by improving the initial AlGaN quality and suppressing the self-compensation from the defects. Silicon is always chosen as the n-type dopant for III-nitrides. When silicon uniform doping is used, the electron concentration can usually reach the magnitude of 10^{18} cm^{-3} when Al content is low. However, once Al content is higher than 85%, the electron concentration is hard to reach to 10^{18} cm^{-3}. Some effects have been made to improve the n-doping of AlGaN, such as indium–silicon codoping, introducing interlayers and SLs [73–76]. By adopting the indium–silicon codoping technique, a n-type $Al_{0.65}Ga_{0.35}N$ with an electron density as high as 2.5×10^{19} cm^{-3}, an electron mobility of 22 $cm^2/V \cdot s$, and a resistivity of 1.1×10^{-4} $\Omega \cdot cm$ was achieved [73]. For higher Al content of 0.75, the electron density and the electron mobility can also reach to 9.5×10^{18} cm^{-3} and 21.1 $cm^2/V \cdot s$, respectively [74]. In addition, delta-doping processes can not only improve the doping efficiency but can also reduce the DD [77]. It is believed that the reduction in the DD is caused by growth interruption during delta-doping, which partially terminates the propagation of dislocations in the epitaxial direction, and thus the impurity self-compensation process is suppressed and the n-type doping efficiency is improved. Polarization-induced doping is an effective technique for AlGaN n-type doping. Based on the polarization-induced doping method, the electron concentration as high as 10^{20} cm^{-3} has been reported [78]. In this case, the electron concentration, mobility, and resistivity have less been affected by temperature variation.

Compared with the n-type doping, it is particularly difficult to achieve p-type doping of AlGaN with high Al content. In III-nitrides, the elements Be, Mg, and Zn are usually taken as the p-type dopants. The activation energies for these three elements in GaN are about 60 meV, 160 meV, and 370 meV, respectively. However, the activation energies for all the three dopants increase with the increase of Al content [79–81]. Additionally, although the Be element has lower activation energy than the others, it is a poisonous metal and it will easily introduce interstitial atoms to compensate the acceptors [79], so Mg is the most commonly used acceptor impurity for p-type

Figure 16

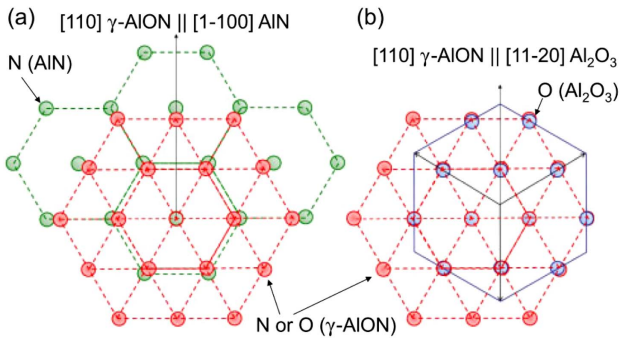

Plan-view anionic atomic arrangements of (a) γ-AlON and AlN and (b) γ-AlON and sapphire. These atomic arrangements were constructed along the [0001] AlN, [0001] sapphire, and [111] γ-AlON axes [72]. Reprinted from Fukuyama *et al.*, Jpn. J. Appl. Phys. **55**, 05FL02 (2016).

doping of AlGaN. The difficulties in performing p-type doping using Mg dopant are largely caused by the following factors.

(1) Strong self-compensation arising from the presence of donor-like native defects. As shown in Figs. 17(a) and 17(b), the formation energies of donor-like native defects such as nitride vacancies (denoted by V_N) and oxygen incorporation are very low when the fermi level is close to valence band maximum [82], which indicates that the self-compensation effect is strong when Mg is used as an acceptor for p-type AlGaN doping. The self-compensation effect can be suppressed by optimization of the growth conditions and reduction of the defect density, which improves the Mg doping efficiency in AlGaN.

(2) Mg, as the acceptor dopant, having low solubility in III-nitride materials. When used as a substitute for Ga or Al in AlGaN, Mg has low solubility in AlGaN because of large formation enthalpy. The relationship between the formation enthalpy (ΔH_f) and the equilibrium Mg solubility (C) is given by the following formula,

$$C = N_{\text{sites}} e^{-\Delta H_f / K_B T}. \tag{3}$$

Here, N_{sites} is the number of sites in AlGaN on which Mg can be incorporated, K_B is the Boltzmann constant, and T is the temperature. According to this formula, the equilibrium Mg solubility decreases with increasing ΔH_f. As seen in Fig. 17(c), with regard to the increase in ΔH_f resulting from the increase of Al composition, the Mg solubility decreases, and thus Mg incorporation is particularly difficult in Al-rich AlGaN. However, the negative surface ΔH_f as shown in

Figure 17

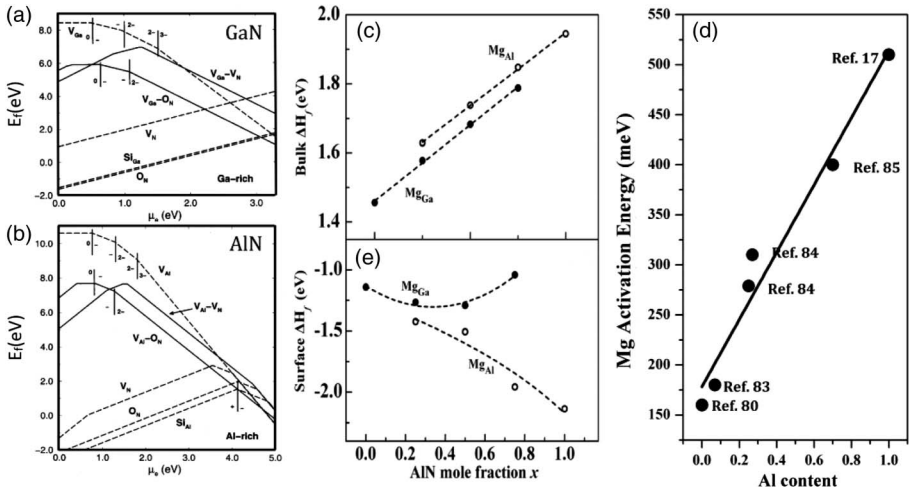

(a) and (b) are the formation energies and ionization levels for the studied defects in GaN and AlN for the Ga-rich/Al-rich case. The experimental bandgap values 3.3 eV for GaN and 5.0 eV for AlN are used to give the upper limit for the electron chemical potential. The dashed lines correspond to isolated point defects [82]. Reproduced from [82] under the terms of the Creative Commons Attribution 2.0 License. With copyright permission. (c) and (e) are the formation enthalpies of Mg_{Ga}/Mg_{Al} in the bulk AlGaN and the surface of AlGaN as a function of Al content under N-rich condition 15]]. Reproduced from [15] under the terms of the Creative Commons Attribution 2.0 License. With copyright permission. (d) The Mg activation energy in AlGaN as a function of Al content [17,80,83–85].

Fig. 17(e) indicates that enhancing the Mg incorporation by using the surface effect should be practically feasible [15]. Additionally, Mg solubility increases with increasing growth temperature according to the formula above. Meanwhile, the Mg acceptors are increasingly compensated by N vacancies at higher temperatures because of the escape of N from AlGaN, and thus suppression of the compensation becomes a main concern. AlGaN grown under HT conditions is beneficial for improving Mg solubility, and N-rich growth conditions are beneficial in suppressing the compensation from nitrogen vacancies.

(3) The activation energy of Mg dopant in AlGaN is very high. Mg acceptors having high activation energies that range from 160 meV to 510 meV with Al compositions ranging from 0 to 1 [17,80,83–85], are shown in Fig. 17(d). The ionization efficiency of Mg for high Al content AlGaN is even lower than millionth under the RT of 300 K. The high activation energy of the Mg acceptors results in low p-type doping efficiency in AlGaN.

To overcome the difficulties of p-type doping in AlGaN, various approaches have been adopted to suppress the self-compensation processes, improve Mg solubility, and reduce the Mg activation energy in AlGaN. In terms of dopant distributions in AlGaN, these approaches can be divided into uniform doping, delta-doping, modulation doping, SLs doping, and codoping processes. In addition, polarization-induced doping and so-called multidimensional doping also take some positive effects on AlGaN p-type doping.

For optimized and uniform Mg doping, use of an appropriate level of Mg doping in AlGaN can obtain relatively low resistivity and high material quality. However, excessive Mg doping of AlGaN will not only result in increased resistivity but will also reduce the material quality. It is believed that this reduction in quality is caused by the high density of stacking faults [86], and the increased resistivity is a result of structural defect generation due to excessive Mg incorporation [87]. Delta-doping can improve the Mg solubility by increasing the incorporation of Mg into AlGaN. Delta-doping maintains a constant group V source supply (NH_3) and offers an alternating source supply between group III (Al and Ga) and the dopant (Mg). The Mg sources are supplied under NH_3 atmospheres, and Mg has a high probability of combining with the Al or Ga vacancies as a result of the interruption of the Al and Ga supply, which thus increases Mg incorporation into AlGaN [83]. HT AlGaN growth with modulation of the V/III ratio can not only improve the AlGaN quality [49], but also improve the Mg solubility [88]. Modified surface engineering is a growth technique that uses periodic interruptions in an extremely N-rich atmosphere to enhance Mg incorporation in Al-rich AlGaN. Additionally, the presence of hydrogen is beneficial for doping and can improve the Mg solubility [89].

During growth of Mg-doped AlGaN, hydrogen originating from both ammonia (NH_3) decomposition and the H_2 carrier gas will combine with the Mg dopant to form Mg-H complexes, which can suppress escape of Mg from AlGaN and improve the Mg solubility. However, use of hydrogen as a donor in AlGaN can compensate for the Mg acceptors, which results in Mg passivation. Thermal annealing of Mg-doped AlGaN in N_2 or O_2 atmospheres can produce Mg activation by dissociating the hydrogen from the Mg-H complexes and can thus improve hole concentration. Mg activation is typically accomplished through a rapid thermal annealing process at 850°C for 10 min in a N_2 atmosphere [90].

The SL doping method is an effective way to improve Mg doping efficiency in AlGaN. The polarization that is induced by lattice mismatch in the heterostructure and noncentrosymmetric for III-nitrides will generate polarization charges and induce

the bending of the energy bands near the interface, as shown in Fig. 18(a) [91], which results in a reduction of the dopant activation energy [91,92], as shown in Fig. 18(b). Mg modulation-doped SLs can form multiple two-dimensional hole gases, which can improve the vertical conductivity on the basis of a single heterostructure [93].

Codoping is a very useful method for AlGaN p-type doping, and many good results had been achieved by this method. According to first principles calculations, codoping with p-type and n-type dopants will generate hybridization of the dopant energy levels, resulting in a rise in the number of donor levels acting as anti-bonding states and a fall in the number of acceptor levels acting as bonding states, and can thus be used as a way to reduce the acceptor activation energy [94]. Indium-surfactant-assistance doping, Mg–O codoping [95], Mg–Zn codoping, and Mg–Si codoping or their combinations with other doping methods have been studied in recent years.

Indium-surfactant-assistance can suppress the self-compensation and improve the p-type doping efficiency [96]. Additionally, a combined indium-surfactant-assisted delta-doping technique was investigated and high-efficiency p-type doping was achieved with a maximum hole concentration of 4.75×10^{18} cm^{-3} and sheet resistivity as low as 2.46×10^{4} Ω/sq [80]. It was found that the incorporation of indium would increase the Mg solubility, as shown in Fig. 19. In addition, the valence band diagrams for the Mg-delta-doped AlGaN without and with In surfactant were calculated using the one-dimensional Schrodinger–Poisson equation solver, as shown in Fig. 20. Based on the theory simulation and experimental results, the high hole concentration in $Al_xGa_{1-x}N$ ($x \sim 0.4$) by indium-surfactant-assisted Mg-delta-doping could be attributed to the significant reduction of compensation ratio and acceptor activation energy (E_A) by introducing indium surfactant. Furthermore, the In surfactant may induce stronger valence-band modulation, leading to the decrease of E_A and the increase of hole concentration.

Zn–Mg codoping in GaN had been experimentally studied early, and it was demonstrated that the incorporation of Zn would improve the hole concentration and reduce

Figure 18

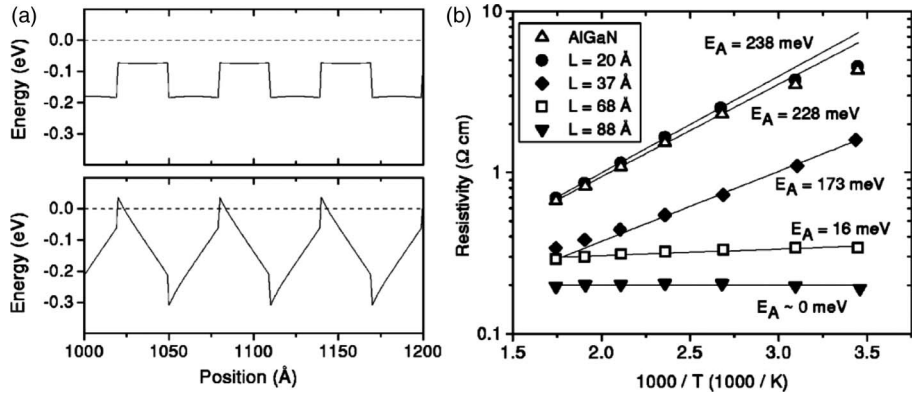

(a) Calculated valence band diagram for Mg-doped $Al_{0.2}Ga_{0.8}N/GaN$ SLs in which the thickness of each layer is 30 Å, shown (A) without and (B) with the polarization fields taken into account. In both plots, the Fermi energy is indicated by the dashed line. (b) Temperature-dependent resistivity measurements. Values obtained on bulk film of Mg-doped $Al_{0.1}Ga_{0.9}N$ are included for comparison [91]. Reprinted with permission from Kozodoy *et al.*, Appl. Phys. Lett. **74**, 3681–3683 (1999). Copyright 1999 AIP Publishing LLC.

the resistivity. By studying the elements distribution in GaN as shown in Fig. 21, it is speculated that the enhancement of electrical conducting characteristics in a Mg–Zn codoping sample might be attributed to the increase of Mg activation ratio due to the reduction of hydrogen solubility [81]. Some theoretical calculations had been performed. Based on first-principles calculation, Zn–Mg codoping was designed to reduce the ionization energy of acceptors in (Al)GaN. The calculated ionization energy of the Zn–Mg acceptor was only 117 meV, which was about 90 meV shallower than that of the isolated Mg acceptor. Figure 22 shows the schematic model of the position, hybridization, and level repulsions with Zn–Mg codoping. It was believed that the hybridization and level repulsion between Zn t_{2d} and N t_{2p} states and the hybridization and level repulsion between the p-like defect level of substantial Zn and Mg should be responsible for the reduction of ionization energy [97].

In 2009, Kang *et al.* proposed the concept of Mg- and Si-delta-codoped $Al_xGa_{1-x}N/Al_yGa_{1-y}N$ SLs method and did the simulation via the first principle. It was found that the internal electric field in SL has been significantly intensified due to the charge transferring from the Si-doped interface to the Mg-doped interface. Based on these calculation results, p-type AlGaN was grown by metal-organic vapor phase epitaxy (MOVPE) and DUV-LED was fabricated, and the acceptor activation energy was reduced by 67 meV [98]. In recent years, polarization-induced doping has been applied in p-AlGaN doping successfully. Due to the lack of centrosymmetric in WZ crystal structure, AlGaN alloys exhibit strong spontaneous polarization. Meanwhile, as the mismatch between heterogeneous epilayers, there exists tensile or compressive strain which will lead to piezoelectric polarization. According to the Gauss law given by Eqs. (4) and (5), the variation of polarization will introduce fixed charges,

$$\sigma = (\vec{P}_1 - \vec{P}_2) \cdot \vec{n}_{12}, \tag{4}$$

$$\rho = -\nabla \cdot \vec{P}. \tag{5}$$

Equation (4) can be used to calculate the polarization-induced interface charges, where σ is the density of the interface charge, P_1 and P_2 are the polarization strengths in the two materials, and the n_{12} is the unit vector that is perpendicular to the interface and point from material 1 to material 2. Similarly, Eq. (5) can be used to calculate the

Figure 19

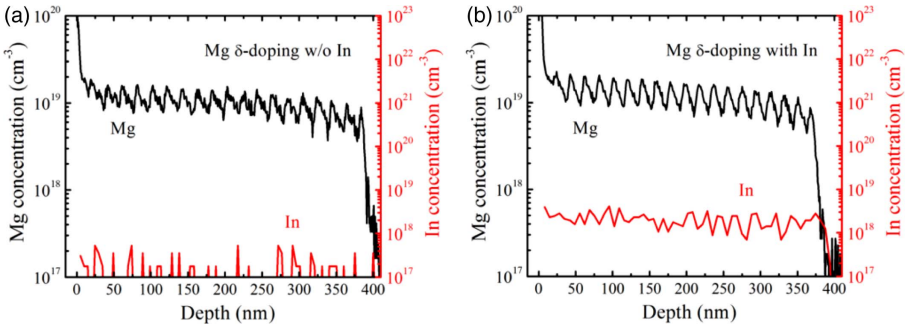

Mg and In concentration depth profiles measured by SIMS for Mg-doped AlGaN layers grown (a) without In surfactant and (b) with In surfactant. The Mg element shows the periodic variations in both the samples [80]. Reprinted with permission from Chen *et al.*, Appl. Phys. Lett. **106**, 162102 (2015). Copyright 2015 AIP Publishing LLC.

polarization-induced volume charges, where ρ stands for the volume charge density and P is the polarization strength in the material. For AlGaN alloy, along the metal-face (0001) direction, gradually increasing Al content within a thin film will lead to fixed positive charges, which will induce electrons within the area due to the electrical neutrality requirement. Contrarily, in the same direction, decreasing Al content will lead to fixed negative charges, which will induce holes within the area. When it is along the N-face (000-1) direction, increasing Al content will lead to fixed negative charges while decreasing Al content will lead to fixed positive charges, thus inducing holes and electrons, respectively. Figure 23 shows the case of increasing Al content along the N-face (000-1) direction [99]. As it can be seen in Figs. 23(d) and 23(e), the polarization-induced field can help to active the deep acceptor and make the valence band smoother to enhance the vertical transport. The typical hole characterizations including concentration, mobility, and resistivity are shown in Fig. 24. Because the Mg acceptors are mainly activated by the polarization field other than thermal activation, the hole concentration will not decrease with temperature. In addition, the more the polarization-induced negative charges are, the higher the hole

Figure 20

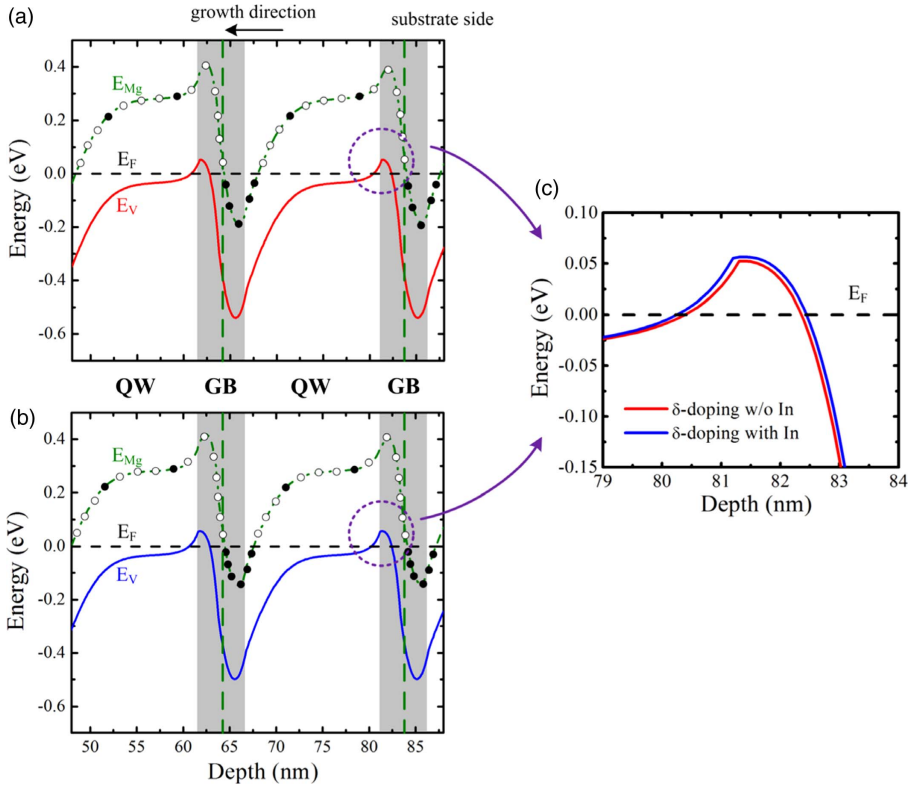

Calculated self-consistent valance band diagrams of Mg-delta-doped p-AlGaN samples grown (a) without In surfactant and (b) with In surfactant. The solid circles show the ionized acceptors in contrast to unionized acceptors, open circles. As compared with other regions, there are nearly no ionized acceptors in the GBs where the Mg acceptor level is above the Fermi level. The two ground-state hole energies are $E_0 - E_F = 6.55$ meV and 12.48 meV, respectively. The vertical green dashed lines indicate the positions of d-doping planes. A detailed view for comparing the VB profiles of two d-doped samples around QW/GB interface is presented in (c) [80]. Reprinted with permission from Chen *et al.*, Appl. Phys. Lett. **106**, 162102 (2015). Copyright 2015 AIP Publishing LLC.

concentration is. However, the mobility will be lower as the existence of alloy scattering within the graded AlGaN layers. Synthetically, the resistivity of the graded AlGaN layer will be lower and less temperature dependence shown as the right graph in Fig. 24.

Based on the polarization-induced doping mechanism, many research groups had realized high hole concentration AlGaN p-type doping with comparatively high average Al content. Researchers from the University of Notre Dame first realized the AlGaN polarization-induced p-type doping by increasing Al content along the (000-1) direction, resulting in a hole concentration of higher than 2×10^{18} cm^{-3}, a resistivity of $0.6\ \Omega \cdot cm$ [99]. Later, some other researchers also made some progress in

Figure 21

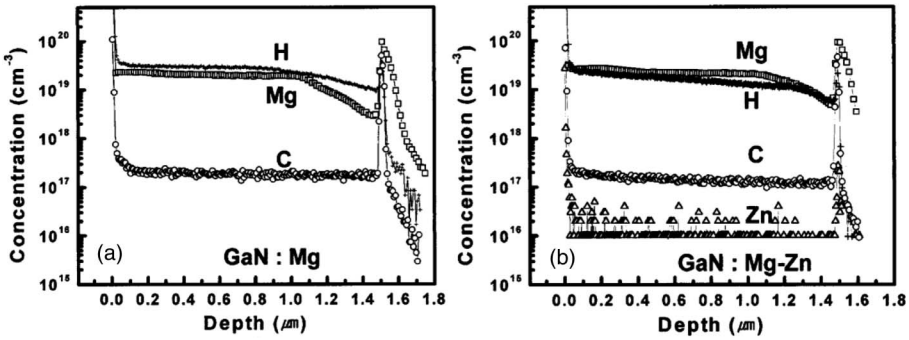

SIMS depth profiles of (a) Mg-doped only GaN ($[Cp_2Mg] = 0.643$ μmol/min) and (b) Mg–Zn codoped GaN ($[Cp_2Mg] = 0.643$ μmol/min and $[DEZn] = 0.616$ μmol/min). Cross, open square, open circle, and open triangle denote hydrogen, Mg, carbon, and Zn, respectively [81]. Reprinted with permission from Kim *et al.*, Appl. Phys. Lett. **77**, 1123–1125 (2000). Copyright 2000 AIP Publishing LLC.

Figure 22

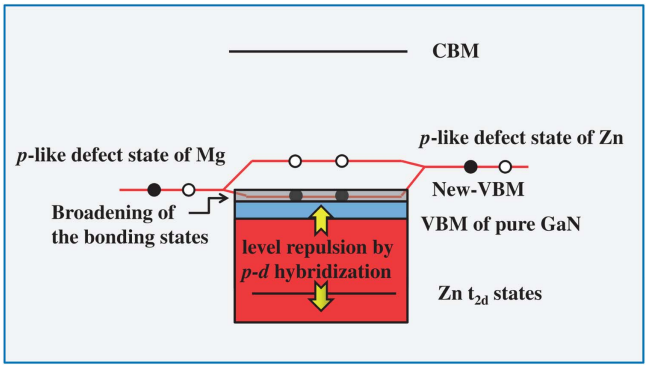

Schematic model showing the position and the hybridization and level repulsions between Zn t_{2d} and N t_{2p} states, and the hybridization and level repulsions between p-like defect level of substantial Zn and Mg. Black and white balls represent electrons and holes, respectively. Note that a "new" higher valence-band maximum (VBM), which is composed of hybrid p-d orbitals and occupied bonding states, is formed [97]. Reprinted from Liu *et al.*, Appl. Phys. Express **6**, 042104 (2013). © IOP Publishing. Reproduced with permission. All rights reserved.

polarization-induced high Al content AlGaN p-type doping. Zhang *et al.* [100] from the Institute of Semiconductors, Chinese Academy of Science, also achieved a p-type AlGaN material with hole concentration larger than 2.5×10^{18} cm^{-3} by decreasing Al content from 0.3 to 0 along the direction of metal-face (0001), which could result in better material quality. Shibin Li *et al.* from the University of Electronic Science and Technology of China used the MBE technique to grow AlGaN with Al grading from 1 to 0.7 along the metal-face (0001) direction and took Be as the dopant [79].

In 2016, a novel multidimensional Mg-doped SL was investigated in an attempt to improve the vertical conductivity. The comparison between the multidimensional Mg-doped SL and conventional 2D superlattice Mg doping is shown in Fig. 25(A) [panels (a) and (b)] [101]. Through the density of state (DOS) analysis by first-principle calculation of valance bands along the [0001] direction of the undoped and Mg-doped structure, corresponding to panels (a)–(e) in Fig. 25(B) and panels (a)–(d) in Fig. 26(A), it is shown that a 3D Mg-doped SL decreases the hole potential barrier along the c-axis and increases the hole concentration in the barrier region shown in panels (e) and (f) in Figs. 26(A). The stronger Pz hybridization as shown in panel (c) in

Figure 23

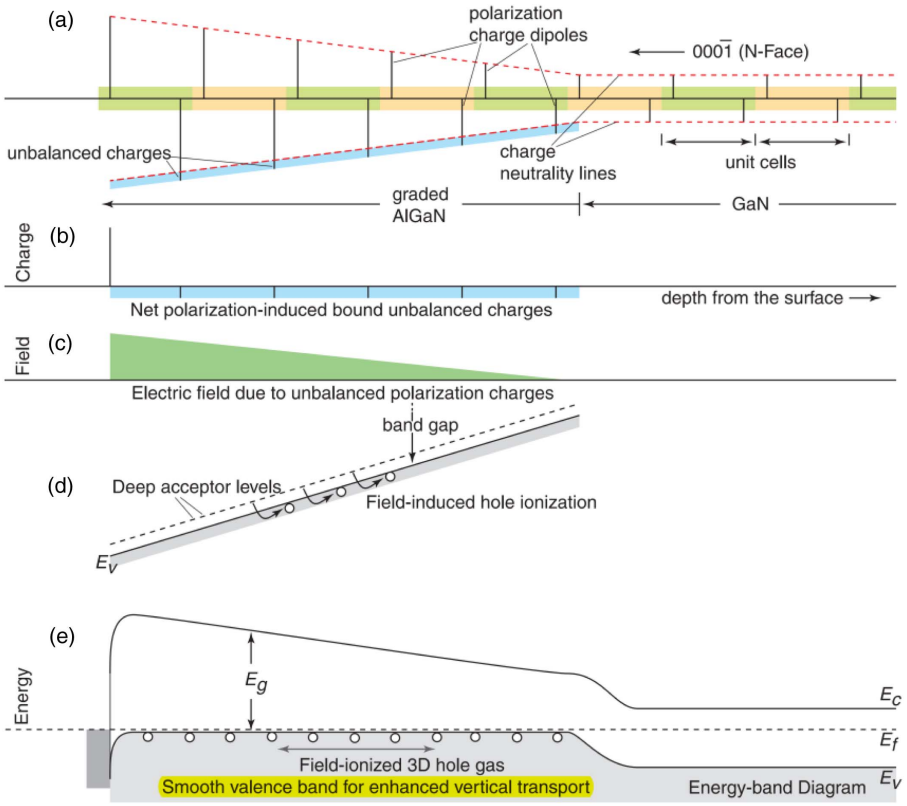

Schematic illustration of polarization-induced p-type doping in graded polar heterostructures. (a) Sheets of charge dipoles in every unit cell of the crystal. The net unbalanced polarization charge is shown in (b), which leads to the electric field in (c), and the energy-band bending in the valence band in (d) if holes are not ionized. Field ionization of holes results in a steady-state energy-band diagram shown in (e), which highlights the smooth valence-band edge without any potential barriers for hole flow. E_f, is the Fermi level; E_c and E_v are the conduction and valence-band edges, respectively; and E_g is the bandgap [99]. From Simon *et al.*, Science **327**, 60–64 (2010). Reprinted with permission from AAAS.

Fig. 26(B) is believed to account for the aforementioned results. Based on the theoretical results, p-type $Al_{0.63}Ga_{0.37}N/Al_{0.51}Ga_{0.49}N$ SLs were grown and high-efficiency p-type doping was achieved with a hole concentration of 3.5×10^{18} cm^{-3} and resistivity of 0.7 $\Omega \cdot cm$ at RT [101].

In addition, other dopants including carbon (C) and beryllium (Be) have been investigated in attempts to improve the p-type doping efficiency of AlGaN with high Al content [79,102], but no major improvements have been made to date. When compared with C and Be, Mg is still a unique p-type dopant for use with GaN and AlGaN. In recent years, methods for p-type doping of AlGaN have been developed by various organizations, as shown in Table 3.

Figure 24

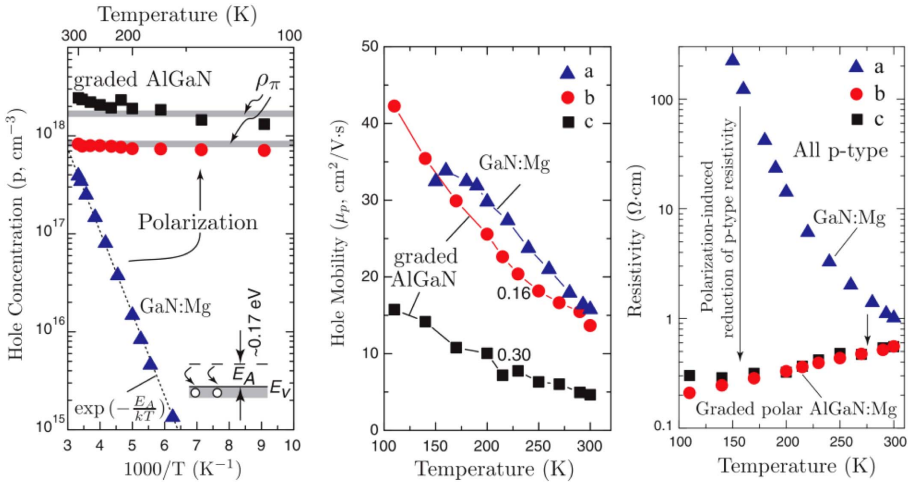

Typical hole characteristics of polarization-induced p-type doping in AlGaN. The left, middle, and right graphs correspond to the hole concentration, mobility, and resistivity depending on temperature, respectively [99]. From Simon *et al.*, Science **327**, 60–64 (2010). Reprinted with permission from AAAS.

Figure 25

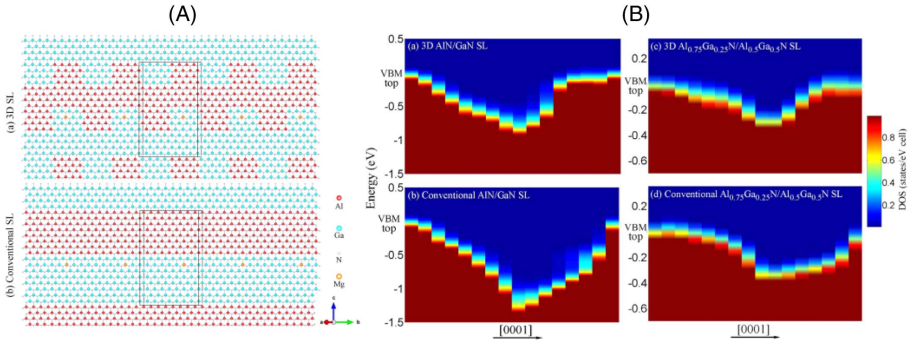

(A) Crystal structures of 3D (a) and conventional AlN/GaN SL (b). (B) Projected DOS of valence bands along the [0001] direction for each bilayer in undoped 3D AlN/GaN SL (a), conventional AlN/GaN SL (b), 3D $Al_{0.75}Ga_{0.25}N/Al_{0.5}Ga_{0.5}N$ SL (c), and conventional $Al_{0.75}Ga_{0.25}N/Al_{0.5}Ga_{0.5}N$ SL (d) [101]. Reproduced from [101] under the terms of the Creative Commons Attribution 4.0 License. With copyright permission.

4. ADVANCES IN ALGAN-BASED ULTRAVIOLET DEVICES

With the breakthroughs in both the quality and the p-type doping of AlGaN materials, AlGaN-based UV devices are being developed rapidly. AlGaN with WZ structure has weak symmetry of crystal lattice, which results in a unique property of optical polarization anisotropy of AlGaN material. In this section, the energy band structures and optical properties of AlGaN-based materials, and the progress made in the research into AlGaN-based UV-LEDs, EB-pumped light sources, LDs, and PDs are presented.

4.1. Energy Band Structures and Optical Anisotropy Properties of AlGaN Materials

In AlGaN material, the valence band maximum is split into HH, LH subbands, and CH subband by the crystal field near the Γ point in the Brillouin zone, as introduced before. Recently, significant progress has been made in simulating on the valance bands with spin-orbit interactions. It is generally accepted that transverse electric (TE)-polarized emission originates from the transition that occurs between the conduction bands and the HH/LH subbands, and that transverse magnetic (TM)-polarized emission originates from the transition between the conduction bands and the CH subbands. The TE polarization has a direction of E⊥[0001], while the TM polarization has a direction of E‖[0001], where E represents the electric field vector of the emitted light.

In a hexagonal crystal system, the light propagation is anisotropic. The light propagating along the ***c*** axis will not generate the birefringence phenomenon, which is

Figure 26

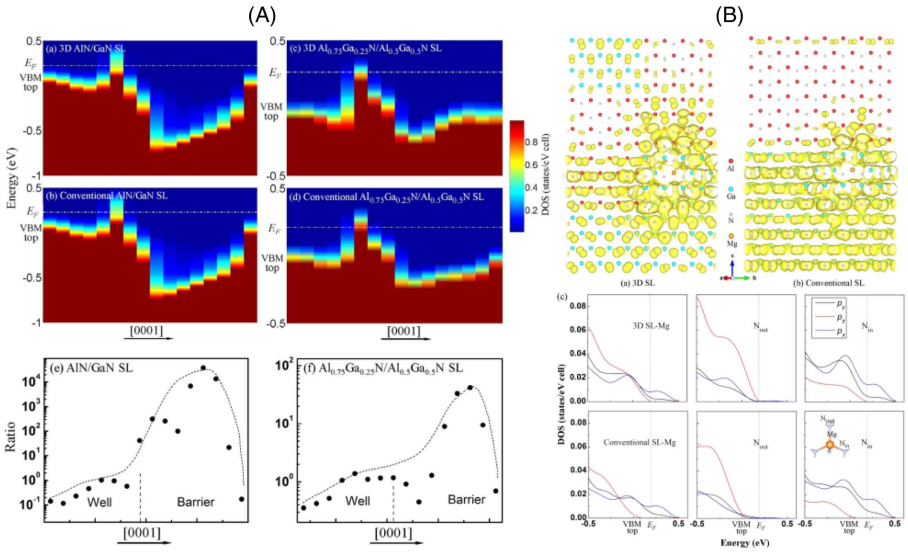

(A) Projected DOS of valence bands along the [0001] direction for each bilayer in Mg-doped 3D and conventional SL (a)–(d). Hole concentration ratio of 3D SL to conventional SL for AlN/GaN (e) and $Al_{0.75}Ga_{0.25}N/Al_{0.5}Ga_{0.5}N$ (f). (B) The surface of the valence states at the top of valance bands for Mg-doped 3D (a) and conventional (b) GaN/AlN SLs with k vector restricted to [0001]. (c) Decomposed DOS of p_x, p_y, and p_z of Mg and bonded N atoms in 3D SL and conventional SL. Te N bonded with Mg lying in the ab plane and out of the plane is respectively denoted as N_{in} and N_{out} in the inset [101]. Reproduced from [101] under the terms of the Creative Commons Attribution 4.0 License with copyright permission.

Table 3. Recent Progress in p-Type Doping of AlGaN

Organizations	Techniques	Material	Hole Concentration at RT (cm^{-3})	Mobility at RT (cm^2/Vs)	Resistivity at RT ($\Omega \cdot cm$)	Year	Refs.
University of Electronic Science and Technology of China, China	Polarization-induced doping	$Al_xGa_{1-x}N$:Mg ($x = 0.7 - 1$)	8×10^{16}	40	1.95	2013	[79]
		$Al_xGa_{1-x}N$:Be ($x = 0.7 - 1$)	9×10^{18}	30	0.0231		
Sun Yat-sen University, China	Indium-surfactant assisted delta-doping	$Al_{0.4}Ga_{0.6}N$:Mg	4.75×10^{18}	1.34	0.98	2015	[80]
Tokuyama Corporation, Japan	Modifying V/III ratio	$Al_{0.7}Ga_{0.3}N$:Mg	1.3×10^{17}	1.02	47	2013	[88]
Ritsumeikan University, Riken Institute, Japan	Alternative codoping	$Al_{0.4}Ga_{0.6}N$:Mg	6.3×10^{18}	1.00	0.99	2011	[94]
Xiamen University, China	Mg- and Si-delta codoped SLs	$Al_{0.2}Ga_{0.8}$ N/GaN SL	5.77×10^{18}	3.21	0.37	2009	[98]
	Multidimensional Mg-doped SLs	$Al_{0.63}Ga_{0.37}N$/$Al_{0.51}G_{0.49}aN$ SLs	3.5×10^{18}	2.55	0.70	2016	[101]
Kogakuin University, Japan	C-doped	$Al_{0.1}Ga_{0.9}N$:C	3.2×10^{18}	0.40	20	2012	[102]
Xidian University, China	Uniform doping	$Al_{0.2}Ga_{0.8}N$:Mg	—	—	0.71	2009	[103]

called ordinary light (***o*** light), while the light propagating deviating from the ***c*** axis will generate the birefringence phenomenon, which is called extraordinary light (***e*** light). The refractive index matrix of AlGaN can be expressed as follows:

$$n_{ij} = \begin{bmatrix} n_{11} & 0 & 0 \\ 0 & n_{22} & 0 \\ 0 & 0 & n_{33} \end{bmatrix}, \tag{6}$$

where $n_{11} = n_{22} = n_o$, $n_{33} = n_e$, and the n_o and n_e stand for the refractive indices of ***o*** light and ***e*** light, respectively. For different wavelengths, the refractive indices are different due to the dispersion relation. The ***o*** light and ***e*** light refractive index dispersion laws for AlN and GaN materials are expressed from Eqs. (7)–(10):

$$n_o(\mathrm{AlN}) = 2.035 + 0.015/\lambda^2, \tag{7}$$

$$n_e(\mathrm{AlN}) = 2.078 + 0.018/\lambda^2, \tag{8}$$

$$n_o(\mathrm{GaN}) = 2.27 + 0.034/\lambda^2, \tag{9}$$

$$n_e(\mathrm{GaN}) = 2.31 + 0.037/\lambda^2, \tag{10}$$

where the λ is the light wavelength expressed in micrometers [104]. Equations (7) to (10) are valid at the wavelength from 442 nm to 1064 nm with uncertainty of ± 0.005, and with lower precision they can be used at an extended range from 253 nm to 2500 nm [105]. The element values of the AlGaN refractive index matrix can refer to the counterparts of GaN or AlN. Correspondingly, the TM- and TE-polarized emissions in AlGaN-based emitters are ***o*** light and ***e*** light, respectively, thus possessing different propagation characterization.

When the Al content is low, the HH and LH subbands are on top of the valence band. TE-polarized emission is then predominant and the TM-polarized emission is weak.

With increasing Al content, the HH and LH subbands fall while the CH subbands rise, and thus the TE-polarized emission becomes weaker while the TM-polarized emission becomes stronger. The crossover from TE to TM polarization occurs at the critical Al composition. With further increases in the Al composition, the TM-polarized emission then becomes predominant while the TE-polarized emission becomes negligible. It was predicted by theoretical calculation that the order of these subbands is fundamentally different due to the difference in the crystal-field splitting energy of $\Delta cr = 10$ meV for GaN and $\Delta cr = -169$ meV for AlN [5]. The valence band levels of $Al_XGa_{1-X}N$ with increasing Al content (x) from GaN ($x = 0$) to AlN ($x = 1$) are shown in Fig. 27 [7]. The peak spontaneous emission coefficients for the TE and TM polarizations as a function of the Al content in an $Al_xGa_{1-x}N/AlN$ QW structure with a well thickness $L_W = 2.5$ nm on c-plane AlN substrates for several carrier densities are shown in Fig. 28 [106].

It can be indicated that the surface emission along c-orientated $Al_xGa_{1-x}N$ will become weaker with increasing Al content, which is not beneficial for the achievement of surface-emitting devices, such as LEDs and LDs. In order to achieve a strong surface emission in AlGaN with a high Al content, nonpolar or semipolar AlGaN is required to reduce the spontaneous polarization in AlGaN material. Additionally, an AlGaN/AlN MQW structure has an important effect on the polarization switching point. It is believed that the TE to TM polarization switching point is determined by Al content, material strain, well width, and barrier carrier concentration in an AlGaN/AlN MQW structure. The integrated PL intensities of the TE and TM polarizations as a function of L_W in $Al_{0.65}Ga_{0.35}N/AlN$ QWs measured at 10 K are shown in Fig. 29 [107]. The intensity of the TE-polarized emission increases with decreasing L_W, while the intensity of the TM-polarized emission decreases with decreasing L_W. The gains of the TM and TE polarizations of the AlGaN/AlN QW with high Al content are shown as functions of carrier concentration in AlN barrier in Figs. 30(a) and 30(b) [108], respectively. High gain for the TM polarization in AlGaN/AlN QWs can be realized using a high Al material composition, a large well width, and a high barrier carrier concentration. It is expected that a high-efficiency DUV AlGaN-based LED with TM-polarized emission could be achieved by optimization of the parameters of the AlGaN/AlN MQW structures.

Figure 27

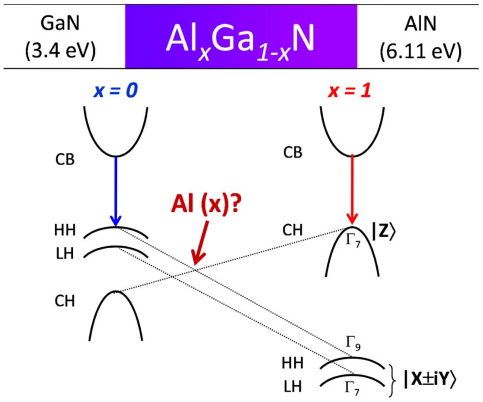

Valence band levels of $Al_xGa_{1-x}N$ with increasing Al content (x) from GaN ($x = 0$) to AlN ($x = 1$) [7]. Reprinted from the doctoral dissertation "MOVPE growth of AlN and AlGaN/AlN quantum wells and their optical polarization properties."

4.2. AlGaN-Based Ultraviolet LEDs

AlGaN-based UV-LEDs have numerous advantages, including short operating wavelengths, small size, compact structures, high efficiency, operational stability, and long lifetimes, and can be applied in fields such as solid-state lighting, displays, high-density data storage, manufacturing, biology, medicine, disinfection processes, dentistry, identification of hazardous biological agents, and many other areas.

Following the commercialization of GaN-based blue and green LEDs, it is increasingly necessary for UV-LEDs to realize applications at shorter wavelengths. AlN or AlGaN structures with wider bandgaps can achieve UV light emission. After the realization of p-type AlGaN in 1991, an UV GaN/AlGaN LED based on a double heterostructure was developed for the first time [109]. In 1998, an UV GaN/$Al_{0.2}Ga_{0.8}N$

Figure 28

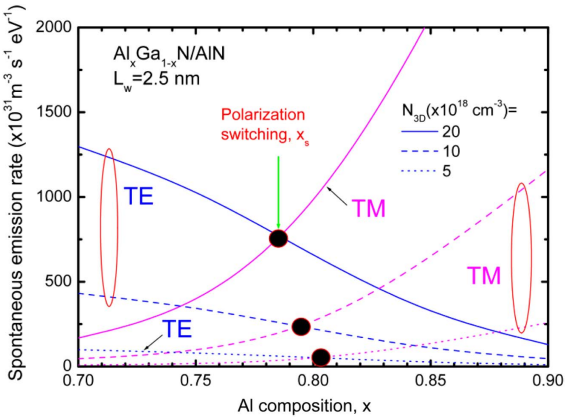

Spontaneous emission peaks for TE and TM polarizations as a function of the Al compositions of $Al_xGa_{1-x}N/AlN$ QW structures ($L_{aw} = 2.5$ nm) on c-plane AlN substrates for several carrier densities [106]. Reprinted with permission from Park and Shim, Appl. Phys. Lett. **102**, 221109 (2013). Copyright 2013 AIP Publishing LLC.

Figure 29

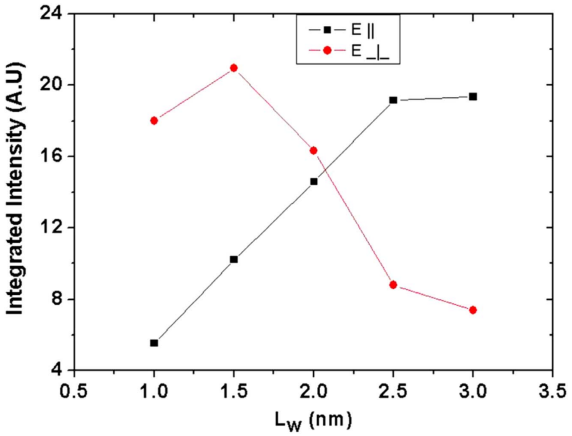

Integrated PL intensities of the TE and TM polarizations as a function of L_w in $Al_{0.65}Ga_{0.35}N/AlN$ QWs measured at 10 K [107]. Reprinted with permission from Altahtamouni *et al.*, Appl. Phys. Lett. **101**, 042103 (2012). Copyright 2013 AIP Publishing LLC.

MQW LED was grown on a sapphire substrate by MOCVD with a wavelength of 353.6 nm, a linewidth of 5.8 nm, output power of 13 μW at 20 mA, a turn-on voltage of approximately 4 V, and an EQE of less than 1%. The low EQE of the device was limited by the piezoelectric effect and by absorption from the GaN layers. However, it was the first report of the shortest wavelength to be emitted by nitride-based QW LEDs in 1998 [110]. To reduce the piezoelectric effect and improve the EQE, strain-reduced $Al_{0.08}Ga_{0.92}N/Al_{0.12}Ga_{0.88}N$ MQW structures were used to suppress the piezoelectric field, and an UV-LED with an operating wavelength of 346 nm was fabricated in 1999 [111]. In addition, a Mg-doped $GaN/Al_{0.25}Ga_{0.75}N$ SL was used as a p-type layer to improve the hole injection efficiency of an $Al_{0.03}Ga_{0.97}N/Al_{0.25}Ga_{0.75}N$ MQW LED, and an operating wavelength of 333 nm at a pulsed current density of 0.13 kA/cm^2 was achieved in 2000. This was the shortest wavelength to be reported for nitride-based QW LEDs at that time [112]. Shortly afterwards, RIKEN reported that $Al_{0.18}Ga_{0.82}N/AlN$ and $Al_{0.18}Ga_{0.82}N/Al_{0.8}Ga_{0.2}N$ MQWs that were grown on SiC substrates by MOCVD had been investigated, and that DUV emissions of PL at 77 K were observed at wavelengths of 234 nm and 245 nm, respectively [113]. Additionally, DUV AlGaN MQW LEDs with operating wavelengths of 222–231 nm were also fabricated. These LEDs, which operated in pulsed mode at RT, produced maximum output powers of 0.15 mW and 0.014 mW and EQEs of 0.2% and 0.003% at wavelengths of 227 nm and 222 nm, respectively [55]. In 2006, an AlN PIN (p-type/intrinsic/n-type) homojunction LED with an emission wavelength of 210 nm was produced, and this remains the shortest wavelength to be reported to date for any type of LED [114].

In recent years, high-efficiency AlGaN-based DUV-LEDs have been developed by several research organizations. UV Craftory in Japan reported a high-efficiency DUV-LED was achieved with an EQE of 14.3% at 2 mA and wavelength of 285 nm [115]. Sensor Electronic Technology Inc. in the USA reported a DUV-LED was fabricated by using UV transparent and stable encapsulation material to improve the light extraction, and high efficiency was achieved with an EQE of 11% at 10 mA and wavelength of 278 nm [116–119]. RIKEN in Japan reported a DUV-LED was fabricated by introducing a multiquantum barrier (MQB), and high efficiency was achieved with an EQE of 7% at 25 mA and wavelength of 279 nm [120]. Later in 2017, they further improved the EQE to about 20.3% at 275 nm by using a transparent AlGaN:Mg contact layer, a Rh mirror electrode, an AlN

Figure 30

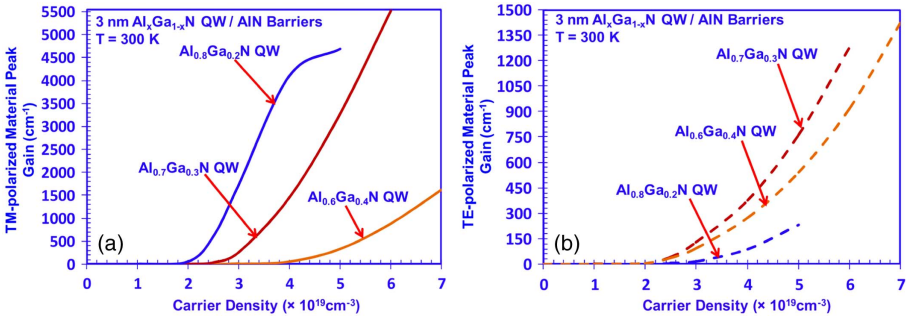

Gains of (a) TM polarization and (b) TE polarization of $Al_xGa_{1-x}N$ QWs with L_w of 3 nm and Al compositions of $x = 60\%$, 70%, and 80% as a function of the AlN barrier carrier concentration [108]. Reprinted with permission from Zhang *et al.*, Appl. Phys. Lett. **97**, 111105 (2010). Copyright 2010 AIP Publishing LLC. With copyright permission.

template on a patterned sapphire substrate, and encapsulation resin, which currently is the highest EQE at a wavelength shorter than 280 nm [121]. Crystal IS in the USA reported a DUV-LED was fabricated by introducing die thinning and encapsulation, and high efficiency was achieved with an EQE of 5.8% at 60 mA and wavelength of 271 nm [122]. The University of South Carolina in the USA reported a DUV-LED with a (6 × 6) micropixel array was fabricated, and high efficiency was achieved with an EQE of 4% at 40 mA and wavelength of 268 nm [123]. Tokuyama Corporation in Japan reported that DUV-LEDs were grown on AlN substrates, and high performance was achieved with an EQE of 2.4% and 2.25% for the wavelengths of 268 nm and 261 nm, respectively [124,125]. Meijo University and Nagoya University in Japan developed DUV-LEDs with EQEs of 5.1% and 3.1% for the wavelengths of 280 nm and 257 nm, respectively [126,127]. Nichia in Japan reported DUV-LEDs with an EQE of 2.78% and wavelength of 281 nm [128]. In 2016, the Chinese company, EpiTop Optoelectronics Technology Co Ltd, reported that they successfully fabricated DUV-LEDs with a wavelength of 280 nm from a single 45 μm × 45 μm large-chip. The optical output power was 176.6 mW at RT at 1 A DC operation, which was the highest reported optical power from a single die at such a short wavelength under DC operation and made a world record optical, as shown in Fig. 31 [129]. Recently, Inoue *et al.* demonstrated a high-power 1 mm × 1 mm single-chip sub-270 nm DUV-LED using a large-area AlN nanophotonic light-extraction structure that was fabricated by nanoimprint lithograph, as shown in Fig. 32 [130]. The output power of more than 150 mW was observed at an injection current of 850 mA at a peak emission wavelength of 265 nm, as exhibited in Fig. 33 [130]. To date, this is the highest output power for DUV-LEDs with emission wavelengths shorter than 280 nm during continuous wave (CW) operation. The recent development progress in high-efficiency AlGaN-based DUV-LED has been summarized in Table 4.

The current state-of-the-art in terms of EQE results for DUV-LEDs is shown in Fig. 34. The EQE drops dramatically with decreasing wavelength, and this is caused by a number of factors. First, the AlGaN quality decreases with increasing Al content, which results in an increase in the DD, reduction of the IQE, and further reduction of the EQE with decreasing wavelength. Surface plasmons (SPs) can be used to improve the IQE of DUV-LEDs by means of coupling between QWs and SPs [144,145]. Second, the low p-type doping efficiency in AlGaN with high Al content leads to

Figure 31

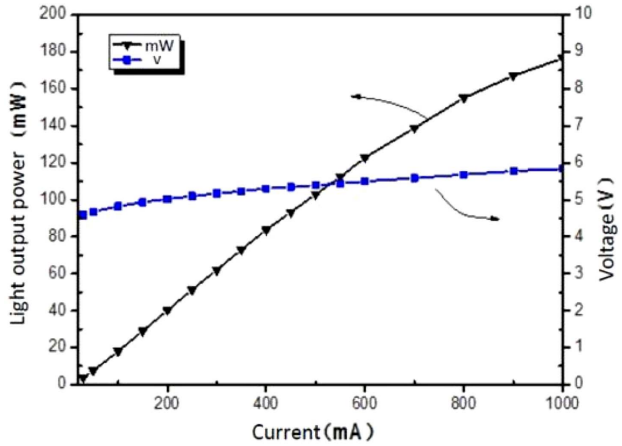

L-I and IV characteristic of the 45 μm × 45 μm chip LED at 280 nm [129]. With copyright permission from the EpiTop Optoelelctronics Technology Co Ltd.

a low carrier recombination probability and high resistance, which both reduce the EQE. Third, degradation of the optically polarized emissions with increasing Al contents is also believed to cause a reduced EQE at smaller wavelengths [5,7,106–108].

Sensor Electronic Technology Inc. in the USA reported that the improved efficiency of 278 nm LED was realized with an IQE of 39%, light extraction efficiency (LEE) of 25%, and EQE of 10% [119]. The expression of EQE related with IQE and LEE can be shown in Eq. (11):

$$\eta_{\mathrm{EQE}} = \eta_{\mathrm{IQE}} \times \eta_{\mathrm{LEE}}, \tag{11}$$

where η_{EQE} is the EQE, η_{IQE} is the IQE, and η_{LEE} is the LEE. Kolbe *et al.* [146] calculated the IQE varying with the dislocation density for a 280 nm LED. According to the calculated results, the reduction of dislocation density is required to improve the IQE. For a LED with a wavelength of 280 nm, the IQE can be improved to above 60% only if the dislocation density is reduced to below 5×10^8 cm^{-2}. Further, the EQE can be improved to 12% only if the LEE of above 20% is achieved according to Eq. (11).

Figure 32

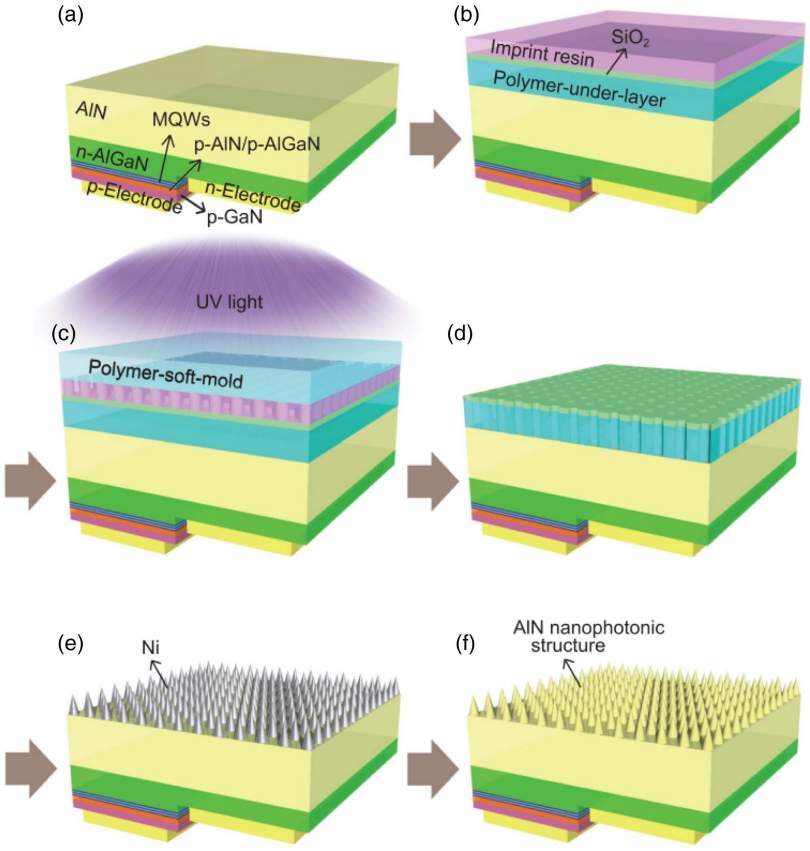

Schematic diagrams of fabrication process flow used to construct nanophotonic light extraction structure for DUV-LEDs using soft UV NIL and ICP dry etching processes: (a) after mesa etching and formation of the p and n-electrodes; (b) the sacrificial polymer underlayer, SiO_2 hard mask, and imprint resin coating; (c) soft UVNIL process; (d) ICP dry etching of the SiO_2 and polymer; (e) Ni deposition and lift-off process; and (f) AlN ICP dry etching and wet etching processes [130]. Reproduced from [130] under the terms of the Creative Commons Attribution 4.0 License. With copyright permission.

Table 4. Recent Development Progress in High-Efficiency AlGaN-Based DUV-LEDs

Organizations	Structures and Techniques	EQE	Wavelength (nm)	Year	Refs.
UV Craftory, Japan	With encapsulation	14.3% at 2 mA	285	2014	[115]
Sensor Electronic Technology Inc., USA	With UV transparent and stable encapsulation	11% at 10 mA	278	2015	[116–119]
RIKEN, Japan	With MQB	7% at 25 mA	279	2014	[120]
	Transparent AlGaN:Mg contact layer, Rh mirror electrode, AlN template on a patterned sapphire substrate, encapsulation resin	20.3% at 10 mA	275	2017	[121]
	Transparent AlGaN:Mg contact layer High reflective index electrode	5.5% at 35 mA	287	2013	[131]
Crystal IS, USA	Die thinning and encapsulation	5.8% at 60 mA	271	2013	[122]
		5.5% at 50 mA	266	2013	[132]
University of South Carolina, USA	With (6 × 6) micropixel array	4% at 40 mA	268	2013	[123]
Tokuyama Corporation, Japan	LED grown on AlN Substrate (by HVPE)	2.4% at 250 mA	268	2013	[124,125]
		2.2% at 20 mA	261		
Meijo University, Japan	(800 μm × 800 μm) packaged device with flip-chip configuration	5.1% at 20 mA	280	2016	[126,127]
Nagoya University, Japan		3.1% at 20 mA	257		
Nichia Chemical Industries, Japan	Sapphire/AlN/AlGaN-QW	2.78% at 20 mA	281	2010	[128]
National Institute of Information and Communications Technology, Japan	Nanoimprint lithography	3.9% at 850 mA	265	2017	[130]

In summary, AlGaN-based DUV-LEDs with short operating wavelengths have been achieved, and these wavelengths have been extended to 222 nm for AlGaN/AlN MQW devices and 210 nm for AlN PIN homojunction devices. The EQEs of AlGaN-based LEDs have been achieved 5.8% at 271 nm and 20.3% at 275 nm. However, the EQEs of DUV-LEDs are still low when compared with those of GaN-based blue and green LEDs. There is also a considerable drop in efficiency, which is caused by high dislocation densities, low hole concentrations, and low LEEs for the AlGaN-based LEDs. Furthermore, the EQE also drops dramatically with decreasing wavelength, which is caused by deterioration in the AlGaN quality, the difficulty of p-type doping processes, and degradation of the optically polarized emission with increasing Al content. The research target for AlGaN-based UV-LEDs in future work should be to further improve the EQE. It is expected that high-efficiency DUV AlGaN-based LEDs will be realized by improving the quality and p-type doping of AlGaN as well as optimizing the parameters of the AlGaN/AlN MQWs.

4.3. EB-Pumped AlGaN-Based Ultraviolet Light Sources

As mentioned before, one of the important reasons leading to the low efficiency of AlGaN-LEDs is the difficulty of p-type doping. One alternative approach is to bypass the difficulty of the p-type doping processes and realize DUV light emission using EB pumping. A schematic illustration and a prototype photograph of a typical EB-pumped DUV light source are shown in Fig. 35 [147].

Compared with AlGaN-based DUV-LEDs using electric pumping, AlGaN-based DUV light sources using EB pumping have multiple advantages. First, no p-type layer is required in the structure, thus avoiding the difficulty of the p-type doping processes

in AlGaN. Second, the simple light source structure is convenient for epitaxial growth and manufacturing processes. Third, the absorption of the emitted light is reduced by the simplified structure without any p-type layers. Fourth, AlGaN-based light sources based on EB pumping are suitable for fabrication of large-scale light sources. Additionally, it is possible to realize both high power and high efficiency because of the low device resistance. Finally, AlGaN-based light sources with EB pumping can be applied in the field of UV radiation, and are especially suitable for use in field-emission displays.

As an alternative to DUV-LEDs, EB-pumped DUV light sources have a short development history of less than 10 years. In 2009, hexagonal boron nitride (hBN) powder that was to be used as a fluorescent material for DUV light sources was irradiated by an EB, and DUV light emission was achieved at a wavelength of 225 nm, with maximum output power of 1 mW and power conversion efficiency (PCE) of 0.6% [148]. However, the powder and the bulk material have high absorption and a low carrier radiative recombination probability during EB excitation. MQW structures with low

Figure 33

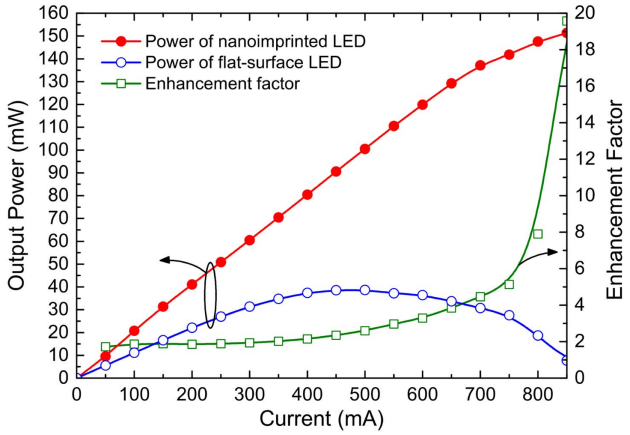

Output power and enhancement factor characteristics [130]. Reproduced from [130] under the terms of the Creative Commons Attribution 4.0 License. With copyright permission.

Figure 34

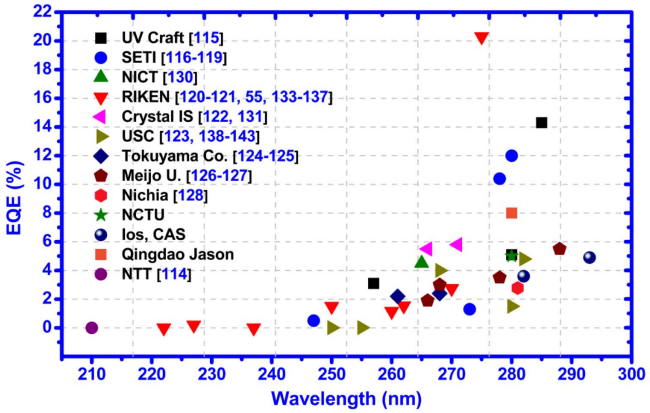

State-of-the-art in EQE results for DUV-LEDs [55,114–128,130,131,133–143].

absorption and high IQEs can realize high emission efficiencies. In 2010, an $Al_{0.69}Ga_{0.31}N/AlN$ MQW was grown on an AlN/sapphire substrate, and a high-performance DUV light source based on EB excitation was achieved with an operating wavelength of 238 nm, output power of 100 mW, and a PCE of 40%, as shown in Fig. 36 [149].

In 2011, a Si-doped AlGaN film was grown on an AlN/sapphire substrate, and a DUV light source tube based on EB excitation was then fabricated. The improved lifetime for the DUV light source tube was achieved at a wavelength of 247 nm, with an output power of 2.2 mW, a PCE of 0.24%, and a lifetime of 2000 h at an EB current of 100 μA [147]. In 2012, an EB-pumped DUV light source tube was fabricated with an AlGaN MQW structure as a target and a graphene nanoneedle as a field electron emitter, and DUV light emission was achieved at a wavelength of 240 nm, with output power of 20 mW and a PCE of 4% [150]. In 2013, a Si-doped AlGaN MQW was fabricated as a target for an EB-pumped DUV light source, and DUV light emission was achieved at a wavelength of 256 nm, with output power of 15 mW and a PCE of 0.75% [151]. In 2015, an EB-pumped DUV light source was produced with a wavelength of 270 nm, an output power of 3.2 mW, and a PCE of 0.16% [152]. In 2016, a novel structure for a quasi-2D GaN layer inserted into an AlGaN MQW to act as an active region for EB-pumped UV light sources was grown by MBE using the submonolayer digital alloying technique, and mid-UV light emission was achieved at a wavelength of 285 nm with output power of 27 mW and a PCE of 0.3% [153]. In 2016, an AlGaN-based MQW was irradiated using a pulsed electron beam, and DUV light emission was achieved at a wavelength of 246 nm, with a peak output power of 230 mW and a PCE of 0.43% at a beam energy of 12 keV [154]. The progress in the development of EB-pumped DUV light sources by various research organizations is summarized in Table 5.

While the output characteristics of these EB-pumped DUV light sources have been improved, their output powers and emission efficiencies are not yet satisfactory for the desired applications. Many challenges still exist in the fabrication of EB-pumped DUV light sources. First, the light sources under EB excitation are usually generated using thermal cathodes, which leads to high electric power consumption and reduced PCE. To reduce the electric power losses, it is necessary to use field emission cold

Figure 35

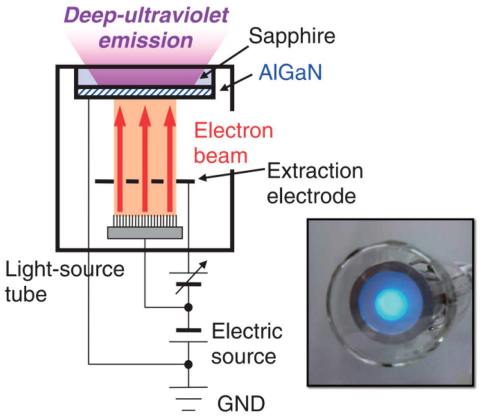

Schematic illustration and prototype photograph of EB-pumped DUV light source [147]. Reprinted from Shimahara *et al.*, Appl. Phys. Express **4**, 042103 (2011). © IOP Publishing. Reproduced with permission. All rights reserved.

cathodes. Second, a high vacuum is required to supply high-energy field emission electron sources, which increases the device fabrication difficulty. Third, it is essential to optimize the thickness of the MQW structure to match the EB penetration depth in the MQW to obtain high carrier injection efficiency. It is expected that production of EB-pumped DUV light sources with high powers and high efficiencies to meet the demand for DUV light emission will be achieved in the near future.

4.4. AlGaN-Based Ultraviolet LDs

Laser is an acronym for light amplification by stimulated emission of radiation, which is generated by light feedback and amplification in a gain media [155]. A laser diode is a semiconductor laser in which the active laser medium is formed by a p-n junction of a semiconductor diode [156]. With their unique properties of high spatial and temporal coherence, AlGaN-based UV-LDs have many advantages, including high light beam quality, high power density, and high modulation speed, which can be applied in areas such as precision laser processing, high-density data storage, nanopattern-type photolithography, medical diagnostics, disinfection, biochemical technology, gas sensing, and materials science.

The typical LD structures include double heterojunctions (DHs), separate confinement heterostructure (SCH), quantum well (QW), quantum dot, nanowire, distributed feedback, distributed Bragg reflector, quantum cascade laser, external cavity laser, vertical cavity surface-emitting laser, vertical external cavity surface-emitting laser, microcavity laser, disk or ring laser, and photonic crystal laser. Restricted by the difficulties of growth and fabrication processes, AlGaN-based UV-LDs with complicated structures have not been achieved yet. In addition, it is particularly difficult to achieve electrically pumped stimulated emission at short wavelengths.

The research on UV-LDs began in the 1970s. Stimulated emission at the low temperature of 2 K from an optically pumped GaN single-crystal needle was first observed in 1971, with a high gain of 10^5 cm^{-1} and a low threshold power of 0.3 MW/cm^2, which indicated great potential for laser action [157]. Optically pumped stimulated emission at RT from a GaN film was first observed in 1990, at a wavelength of 337.1 nm and with an optical pump power threshold of 0.7 MW/cm^2 [158]. In 2006, the shortest wavelength for optically pumped stimulated emission at RT from

Figure 36

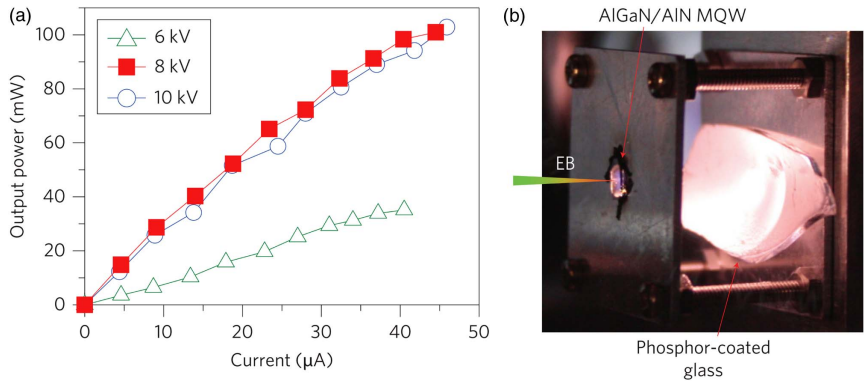

(a) Output power as functions of irradiated current under different accelerate voltages (VA) and (b) photograph of a phosphor-coated glass excited by UV emission from $Al_{0.69}Ga_{0.31}N/AlN$ MQW under 8 kV and 45 μA [149]. Reprinted by permission from Macmillan Publishers Ltd.: Takao *et al.*, Nat. Photonics **4**, 767–770 (2010). Copyright 2010.

Table 5. Recent Progress in Development of EB-Pumped DUV Light Sources

Organizations	Material and Structure	EB Energy	Output Power (mW)	PCE (%)	Wavelength (nm)	Year	Refs.
Mie University, Japan	Si-doped AlGaN film	10 keV, 100 μA	2.2	0.24	247	2011	[147]
National Institute for Materials Science, Japan	hBN powder	8 keV, 50 μA	0.2	0.6	225	2009	[148]
Kyoto University, Japan	AlGaN MQW	8 keV, 45 μA	100	40	238	2010	[149]
Stanley Electric Corporation, Japan	AlGaN MQW	7.5 kV, 80 μA	20	4	240	2012	[150]
Mie University, Japan	Si-doped AlGaN MQW	10 keV, 200 μA	15	0.75	256	2013	[151]
Ioffe Institute, Russia	AlGaN MQW	20 keV, 100 μA	3.2	0.16	270	2015	[152]
Peking University, China	Quasi-2D GaN inserted in AlGaN MQW	15 keV, 700 μA	27	0.3	285	2016	[153]
Palo Alto Research Center, Inc., USA	AlGaN MQW	12 keV, 4.4 mA (Pulsed)	230	0.43	246	2016	[154]

an AlN film was achieved at a wavelength of 214 nm with an optical pump power threshold of 9 MW/cm^2 [159].

With the achievement of p-type doping [160,161], the first GaN/AlGaN DHs with optically pumped stimulated emission at RT were realized in 1993, with an emission wavelength of 368.2 nm and an optical pump power threshold of 0.1 MW/cm^2 [162]. In 1996, the GaN/AlGaN SCH single quantum well with strong near-UV optically pumped stimulated emission at RT was realized at a wavelength of 365 nm and with an optical pump power threshold of 90 kW/cm^2 [163]. In 2004, UV-C band output was realized in an $Al_{0.66}Ga_{0.34}N/Al_{0.76}Ga_{0.26}N$ MQW LD grown on a SiC substrate with optically pumped stimulated emission at RT, with an emission wavelength of 241.5 nm and an optical pump power threshold of 1200 kW/cm^2 [164]. In 2006, optically pumped RT stimulated emission at 214 nm was achieved using high-quality AlN layers that were grown on patterned sapphire substrates by the pulsed lateral epitaxial overgrowth (PLOG) process. The stimulated edge emission spectrum of AlN is the dashed line shown in Fig. 37(a) [159]. As it can be seen, the stimulated emission signal of AlN is TM mode, which is fully different from GaN shown as the solid line in Fig. 37(a). The devices exhibited an optical pump power threshold of 9 MW/cm^2, as shown in Fig. 37(b) [159].

However, the electric pumped AlGaN DUV-LDs face a lot of challenges. In 2003, Kneissl *et al.* realized the electric pumped UV InGaN/InAlGaN multiple-quantum-well laser diodes operating under CW conditions. The emission under CW operation conditions was 373.5 nm with output powers of more than 1 mW [165]. At the same time, Masui *et al.* demonstrated the CW operation at a wavelength of 365 nm at RT. The estimated lifetime of the UV-LDs was approximately 2000 h at an output power of 3 mW [166]. In 2004, Akasaki *et al.* obtained crack-free and partially low-dislocation density AlGaN on a grooved GaN substrate via the combination of a LT deposited AlN interlayer technology and heteroepitaxial lateral overgrowth. Based on this, they reported the lasing wavelength under pulsed current injection at RT of 350.9 nm [167]. After that, in 2007, Yoshida succeeded in fabricating UV GaN/AlGaN laser diodes using a hetero-facet-controlled ELOG (hetero-FACELOG) technique. The UV laser diodes lased in the peak wavelength range from 355.4 to 361.6 nm under a pulsed current operation at RT [168]. Via optimizing the hetero-FACELOG technique, Yoshida *et al.* further pushed the lasing wavelength to a shorter region and the electric

pumped AlGaN LD by lasing at 342 nm and even at 336 nm was demonstrated. The schematics structure for the 336 nm LD and the light output-current characteristic are shown in Figs. 38(a) and 38(b) [169], respectively. The peak output power for the AlGaN MQW UV-LD lasing at a wavelength of 336.0 nm is 3 mW and the external quantum efficiency is about 1.1%. [169,170].

Up to now, the 336 nm lasing is the shortest wavelength electrically pumped AlGaN LD. However, some research demonstrated that with nanowire structures, shorter wavelength AlGaN-based LDs could be realized [171–173]. As shown in Figs. 39(a) and 39(b), a nanowire LD had been realized at a wavelength of 262.1 nm on CW operation at 77 K using a nearly defect-free AlGaN nanowire heterostructure grown

Figure 37

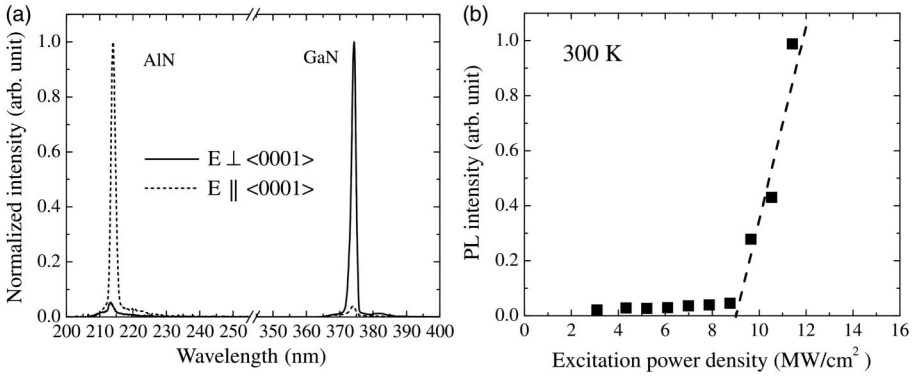

(a) Stimulated edge emission spectra of AlN and GaN for TE and TM polarization. (b) Intensity of edge emission PL signal as a function of excitation power density [159]. Reprinted from Shatalov *et al.*, Jpn. J. Appl. Phys. **45**, L1286–L1288 (2006). © IOP Publishing. Reproduced with permission. All rights reserved.

Figure 38

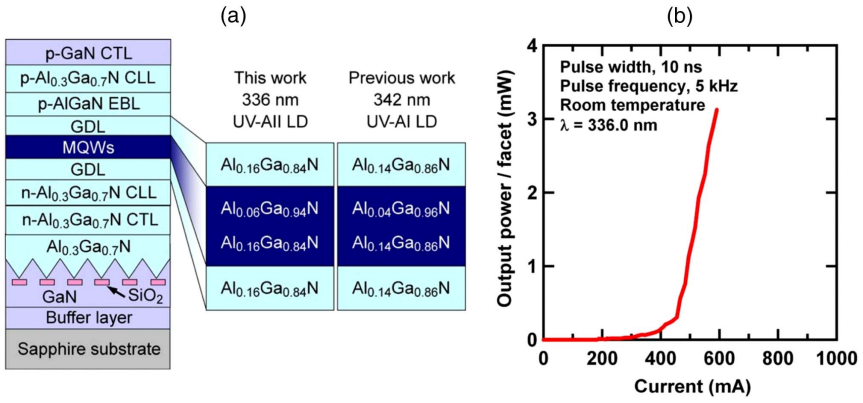

(a) AlGaN MQW UV-LD. Schematic illustration shows a layer structure of an AlGaN MQW UV-LD on a sapphire substrate lasing at a wavelength of 336.0 nm. Another layer structure of the previous reported 342 nm AlGaN MQW UV-LD is also illustrated for comparison. (b) Light output-current and voltage-current characteristic for the AlGaN MQW UV-LD lasing at a wavelength of 336.0 nm [169]. Reprinted with permission from Yoshida *et al.*, Appl. Phys. Lett. **93**, 241106 (2008). Copyright 2008 AIP Publishing LLC.

on an Si substrate by the molecular beam epitaxial growth [171]. Additionally, AlGaN core-shell nanowires on an Si substrate as shown in Fig. 39(c) were also fabricated, and electrically injected lasers in the wavelength range of about 320 to 340 nm were achieved, as shown in Fig. 39(d) [172]. The progress in the development of AlGaN-based UV-LDs produced by various research organizations in recent years is summarized in Table 6.

The development of UV AlGaN-based LDs is continuing to move toward shorter wavelengths. However, it is particularly difficult to achieve electrically pumped stimulated emission from LDs in the UV-C band. At present, numerous challenges must be faced to achieve high performance in these LDs. First, the high densities of defects and dislocations in the active regions of these LDs will increase their internal losses, resulting in a reduction of the IQE. Second, the difficulty of performing p-type doping of AlGaN will reduce the hole injection efficiency and increase the device series resistance, which results in an increase in threshold and a reduction in efficiency for LDs that operate under current injection conditions [189]. Additionally, difficulties in device fabrication processes including etching, thinning, and cleaving will increase device losses and reduce their efficiency. Furthermore, no

Figure 39

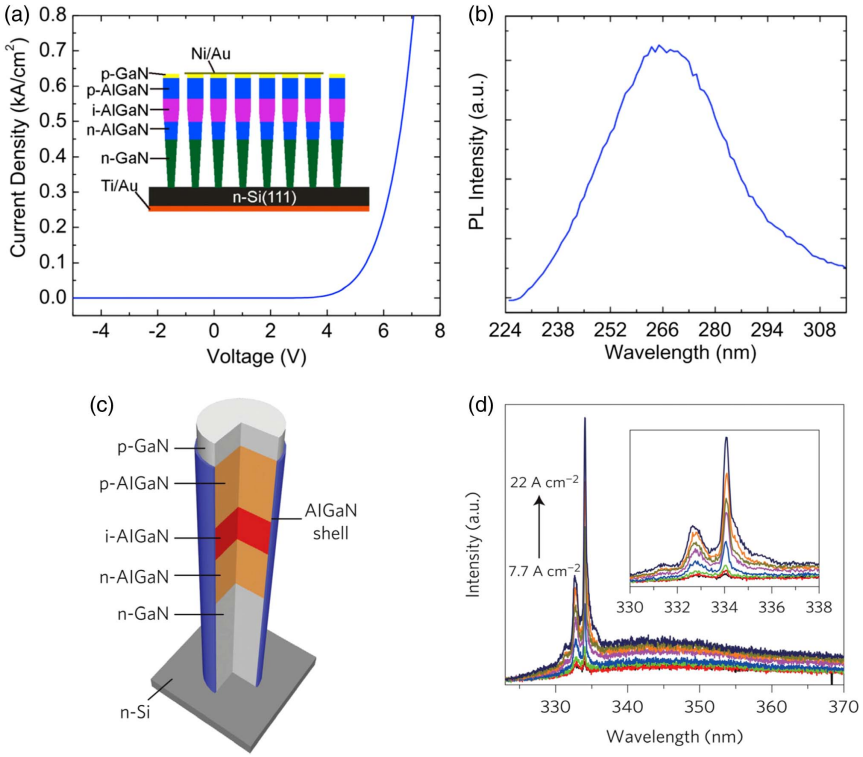

(a) I-V characteristics measured at 77 K. The schematic of the fabricated laser device is shown in the inset; (b) RT PL spectrum measured under an excitation of 7 mW; (c) schematic of AlGaN nanowire double-heterostructures; (d) emission spectra measured at 6 K under different current densities. The black arrow denotes that the current density increases from 7.7 $A \cdot cm^{-2}$ to 22 $A \cdot cm^{-2}$ and the inset shows an enlarged view of the lasing spectra [171,172]. (a), (b) reprinted with permission from Zhao *et al.*, Appl. Phys. Lett. **107**, 043101 (2015). Copyright 2015 AIP Publishing LLC. (c), (d) reprinted by permission from Macmillan Publishers Ltd.: Li *et al.*, Nat. Nanotechnol. **10**, 140–144 (2015). Copyright 2015.

Table 6. Recent Development Progress in AlGaN-Based DUV-LDs

Operation Mode	Organizations	Substrates and Techniques	Threshold	Maximum Power	Differential Efficiency (Both facets)	Wavelength (nm)	Year	Refs.
Pulsed electric pump (at RT)	Central Research Laboratories, Hamamatsu Photonics K.K., Japan	Patterned GaN template (No facet coating)	17.6 KA/cm^2	3 mW	1.1%	336	2008	[169]
			8 KA/cm^2	80 mW	17.4%	359.6	2009	[174]
			56 kA/cm^2	10 mW	14%	356.6	2015	[175]
			15.4 kA/cm^2	35.2 mW	1.8%	340	2013	[176]
	Sandia National Laboratories, USA	Patterned AlGaN template (facets coating)	22.5 kA/cm^2	2.7 mW	0.0135 W/A	353	2015	[177]
Continuous electric pump	McGill University, McMaster University, Canada	AlGaN nanowire laser On Si substrate	200 A/cm^2 at 77 K	—	—	262.1	2015	[171]
			10 A/cm^{-2} at 6 K	—	—	334.1	2015	[172]
			300 A/cm^2 at RT	—	—	289	2015	[173]
Optical pump (at RT)	Kohgakuin University, Japan	SiC substrate	1200 kW/cm^2	—	—	241.5	2004	[164]
	University of South Carolina, USA	AlN/on PSS By PLOG	9 MW/cm^2	—	—	214	2006	[165]
	Sandia National Laboratories, USA	Patterned AlGaN/AlN/sapphire template	34 kW/cm^2	—	—	346	2015	[177]
	University of Sheffield, UK	Porous AlN/sapphire	6.6 kW/cm^2	—	—	340	2009	[178]
	Palo Alto Research Center Inc. (PARC), USA	AlN substrate	175 kW/cm^2	—	—	330	2009	[179]
			126 kW/cm^2	—	—	267	2011	[180,181]
			41 kW/cm^2	—	—	266	2016	[182]
			—	—	—	237–291		
	HexaTech, Inc., North Carolina State University, USA	AlN substrate	84 kW/cm^2	—	—	280.8	2013	[183]
		AlN substrate	90 kW/cm^2	—	—	263.9		
	Technical University of Berlin, Germany	AlN substrate	50 mJ/cm^2	—	—	279	2014	[184]
		AlN/template	65 mJ/cm^2	—	—	272		
	Georgia Institute of Technology, Arizona State University, USA	AlN substrate	427 kW/cm^2	—	—	243.5	2013	[185]
			297 kW/cm^2	—	—	245.3	2014	[186]
		AlN template	95 kW/cm^2	—	—	249	2014	[187]
	Institute of Semiconductors, China	Sapphire substrate	64 mJ/cm^2	—	—	288	2015	[188]

homoepitaxial substrate is available for AlGaN growth processes. Therefore, appropriate substrates with high transparency and high electrical and thermal conductivities are required to improve the performances of these LDs. In addition, an appropriate LD structure design is required to improve device efficiency. In conclusion, the low defect densities of bulk AlN substrates indicate a promising strategy to achieve high-performance LDs.

4.5. AlGaN-Based Ultraviolet PDs

AlGaN based UV-PDs have attracted considerable attention in recent years because of their wide range of potential applications across various fields, including missile warning systems, non-line-of-sight communications, flame detection, medical applications, and environmental monitoring. At present, the most commonly used UV-PD is the photomultiplier tube, which has high gain but suffers from high working voltage requirements, huge device volumes, and fragility. Si detectors can also be used in the UV field. However, complicated spectral filters are needed. As mentioned before, AlGaN is one the best candidates for UV-PDs.

Since GaN-based photoconductors first appeared, work on detection in the deeper UV range using AlGaN-based photoconductors has also been in progress [190,191]. Schottky-type AlGaN-based UV-PDs have also been studied. Researchers found that the insertion layer and appropriate passivation in Schottky AlGaN-based UV-PDs could effectively improve overall device performance [192,193]. Research into Schottky avalanche PDs has also seen some progress. Tut [194] and Huang *et al.* [195] reported Schottky AlGaN-based solar-blind avalanche photodiodes (APDs) with gains of 25 and 10^3, respectively.

AlGaN-based UV metal-semiconductor-metal (MSM) PDs have also been widely investigated. In 1999, French researchers [196] used AlGaN to fabricate MSM UV PDs. Subsequently, the HT AlN interlayer technique was used to improve the quality of $Al_{0.3}Ga_{0.7}N$, and improved PD performance was achieved [197]. In 2006, DUV MSM PDs were fabricated using AlGaN with an Al content of 0.75 [198]. Furthermore, factors such as the use of appropriate electrode materials [199] and annealing temperatures [200] and the insertion of buffer layers [197,201] can make the devices more suitable for deeper UV detection applications. Our team investigated the effect of dislocations on the performance of GaN-based MSM PDs, and found that the screw dislocations were the main reason for the dark current. Based on this theory, we developed using SiO_2 nanoparticles to passivate the dislocations followed by the reduction in the dark current [202,203]. The common MSM AlGaN-based photodetectors cannot work at 0 V bias. To solve this problem, the effect of asymmetric Schottky barrier on GaN-based MSM UV detectors was also studied and high spectral response of self-driven GaN-based detectors by controlling the contact barrier height was realized [204,205]. These achievements widen the application field of MSM AlGaN detectors.

In recent years, surface plasmon has offered new opportunities to engineer and improve the performance of optoelectronic devices, and our team realized high-performance GaN UV detectors by Ag nanoplasmonic enhancement and AlGaN deep UV detectors by Al nanoplasmonic enhancement [206–208]. Figure 40(a) shows the schematic structure of Ag surface plasmon enhancing the performance of GaN detectors and Fig. 40(b) the spectral response of GaN detectors with and without Ag nanoparticles. The responsivity of GaN UV detectors was increased by over 30 times when using Ag nanoparticles. To reveal the physical origin of this enhancement, Kelvin probe force microscopy was used and the localized field enhancement induced by the SP was measured, which was regarded as the main reason for the enhancement

of the responsivity of (Al) GaN detectors, as shown in Fig. 41. This method will open a new door for realizing weak signal detection.

P-n junction-based PDs have the advantage of faster response speeds than other types of structures. In 1999, AlGaN with an Al content of less than 0.15 was used to fabricate PDs. However, the device response time exceeded 0.5 μs as a result of Mg-related defects, and hardly reflected the advantage of the high device speed [209]. Additionally, research into AlGaN-based p-n PDs with shorter detectable wavelengths was also underway, and one year later, a device with a cutoff wavelength of 275 nm was realized [210]. Approaches based on the use of AlN buffer layers and Si-In codoping further improved the device response and quantum efficiency [211]. In 2013, Cicek *et al.* produced a solar-blind UV-PD with a high EQE of 89%, which was the highest reported EQE among p-n AlGaN-based PDs, through the use of high-quality AlN patterns and optimization of the device design and doping profile [212].

APDs work at a high reverse bias with avalanche multiplication, which results in internal current multiplication. With their high internal gains, APDs can realize high responsivity and can thus detect weak signals or even single photons. In 1998, the avalanche effect was observed in GaN by Osinsky, who predicted that GaN-based APDs would become one of the most important UV-PD structures [213]. At present, GaN-based APDs can achieve gains as high as 10^5 to 10^6 and responsivities as high as 1 A/W, and have thus realized visible-blind weak signal detection. A single photon detection efficiency (SPDE) of as high as 30.5% has been achieved with a dark count probability (DCP) of 57%. When the DCP decreases to 1%, the SPDE can still reach 8.8%, which represents an advantage over previous SiC-based UV-PDs [214]. Unlike the rapid development of these visible-blind UV GaN APDs, solar-blind DUV AlGaN APDs are progressing more slowly. There have been hardly any reports of AlGaN APDs with gains of more than 10^5 or single photon detection (SPD) capabilities. In 2005, McClintock *et al.* reported an AlGaN-based solar-blind PD [215]. Their PD was a p-i-n type device with soft breakdown phenomena at relatively low electric fields that eventually saturated without demonstrating a Geiger mode breakdown. Under the bias of 60 V, the maximum gain reached 700, while the electric field was 1.7 MV/cm, which was far below the theoretical value. In 2007, Tut *et al.* [216] reported an APD with a gain of 1560, but the effective area of the device

Figure 40

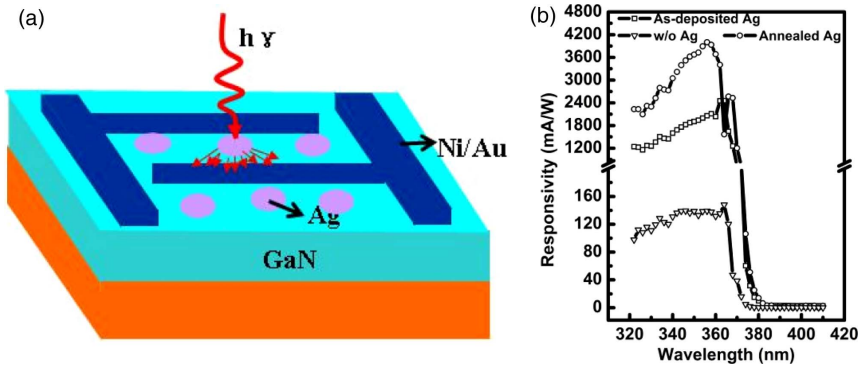

(a) Schematic structure of surface plasmon-enhanced (Al)GaN detectors. (b) The spectral response of GaN detectors with and without Ag nanoparticles [206]. Reprinted from [206] with copyright permission.

was very small, which limited its applications. In 2010, Sun *et al.* [217] reported a p-i-n APD with gain that reached 2500, which is much higher than the previously reported results. In 2012, Lu *et al.* reported a back-illuminated AlGaN-based solar-blind separated absorption and multiplication region APD (SAM-APD) that achieved a maximum gain of more than 3000 at −91 V [218]. Figure 42 shows the schematic structure of back-illuminated AlGaN SAM-APDs and the reverse I-V curves in dark and under UV illumination. For comparison, the gains of the aforementioned Schottky AlGaN-based solar-blind APDs reported by Tut *et al.* [194] and Huang *et al.* [195] were 25 and 4000, respectively. A great deal of research [219–221] has focused on theoretical calculations and performance analyses of AlGaN APDs and has provided important foundations for device design and fabrication. To date, high-gain APDs have not been realized because of the limitations of the AlGaN growth and device processing technologies. While some researchers [222–224] have declared that their APDs had gains of more than 10^4, the effective areas of their devices were too small to be practical and the device reliabilities still remain to be tested.

Figure 41

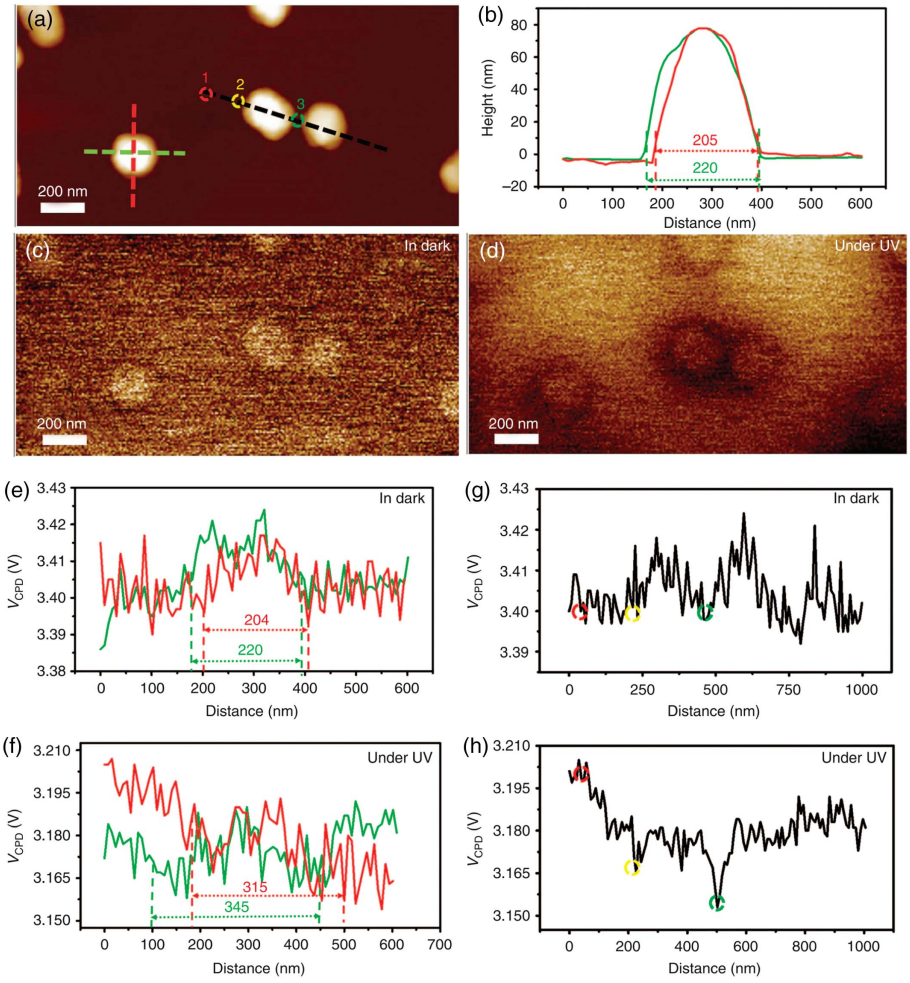

Surface potential reduction in the vicinity of Ag nanoparticles on a GaN epilayer measured by Kelvin probe force microscopy (KPFM) [208]. Reproduced from [208] under the terms of the Creative Commons Attribution 4.0 License. With copyright permission.

Compared with GaN APDs, AlGaN APDs face more fabrication difficulties, which can be summed up as follows. First, it is difficult to grow high-quality AlGaN. Heteroepitaxial AlGaN contains numerous defects that may serve in the roles of primary leakage paths for dark currents, recombination centers for photogenerated carriers [225], and microplasma centers for premature breakdown [213]. Second, the avalanche gain mechanism of AlGaN has not been fully understood to date. Some researchers [219,226] have pointed out that AlGaN layers with different Al contents have shown different breakdown fields and ionization coefficients, and it is thus difficult to analyze these differences quantitatively. Third, the Geiger mode is hard to realize in these layers. GaN APDs are able to detect single photons because they can steadily operate in the Geiger mode. However, AlGaN APDs exhibit strong noise and low gain characteristics in the Geiger mode, and thus fail to achieve SPD. Fourth, doping of and ohmic contact formation on AlGaN remain difficult processes. The activation energies of both n-type and p-type AlGaN increase rapidly with increasing Al content, reaching values as high as 630 meV and 282 meV for Mg-doped p-AlN and Si-doped n-AlN at RT, respectively [99]. When compared with GaN and AlGaN, SiC-based materials show higher crystal quality. Recently, some reports [227,228] have presented the idea that use of SiC in combination with GaN or AlGaN to form a SAM-APD could produce a beneficial structure that could solve the above difficulties.

The progress in the development of AlGaN-based UV-PDs is shown in Table 7. The development aims of AlGaN-based UV-PDs include realization of shorter operating wavelengths, higher responsivities, faster response speeds, and eventually achievement of SPD. Deeper UV detection requires layers with higher Al content. However, epitaxial growth of AlGaN with high Al content is extremely difficult. To realize SPD, it will be necessary for the gain to be at least 10^5 to 10^6 and for the noise to be suitably low. At present, APDs can obtain a gain of 10^4 and can simultaneously achieve sufficiently low noise characteristics by optimizing their configurations, and thus show promise for actualization of SPD.

5. NONLINEAR OPTICAL PROPERTIES OF ALGAN MATERIALS

Since the advent of LDs with high intensity and good coherence, nonlinear optical effects including electro-optic effect, second- and higher-order harmonic generation, optical sum-frequency and difference-frequency, optical parametric oscillation and

Figure 42

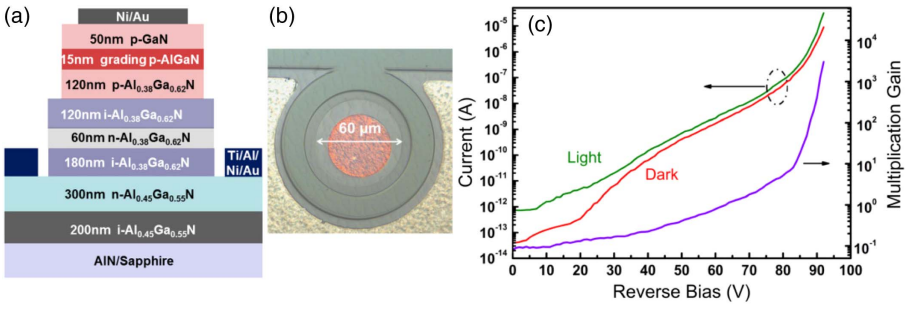

(a) Schematic structure of back-illuminated AlGaN SAM-APDs. (b) The top view of the device. (c) The reverse I-V curves in dark and under UV illumination, and the right-hand axis is the gain [218]. Reprinted with permission from Huang *et al.*, Appl. Phys. Lett. **101**, 253516 (2012). Copyright 2012 AIP Publishing LLC.

Table 7. Recent Progress in Development of AlGaN-Based UV-PDs

Device Structures	Organizations	Light of Detection	Responsivity	Detection Contrast	Gain	Detectivity ($cm \cdot Hz^{1/2}/W$)	Year	Refs.
Schottky	National Cheng Kung University	300 nm–360 nm	0.057 A/W at −2 V	$\sim 1.5 \times 10^2$	—	1.26×10^8 at −2 V	2009	[192]
	National Cheng Kung University	320 nm–360 nm	1.03×10^{-2} A/W at −10 V	3.38×10^5	—	4.52×10^{10} at −10 V	2015	[193]
MSM	Bilkent University	222 nm	0.53 A/W at 50 V	10^5–10^7	—	1.64×10^{12} at 222 nm at 0 V	2006	[198]
	CIOMP, CAS	288 nm	0.288 A/W at 5 V	—	—	—	2014	[205]
	Ferdinand-Braun-Institute	210 nm–260 nm	46 mA/W at 0 V	$>10^4$	—	—	2015	[201]
	Huazhong University of Science and Technology	200 nm–270 nm	2.34 A/W at 269 nm at 20 V	—	—	—	2015	[206]
p-(i)-n	Northwestern University	270 nm–290 nm	136.5 mA/W at 281.5 nm at 0 V	$\sim 10^2$	—	—	2004	[211]
	Northwestern University	270 nm–280 nm	176 mA/W at 275 nm at 0 V	$>10^2$	—	—	2013	[212]
APD	Northwestern University	230 nm–270 nm	0.11 A/W at 254 nm at −25 V	$>10^4$	25	4.68×10^{13}	2005	[194]
	Northwestern University	278 nm	—	—	700	—	2005	[215]
	Bilkent University	230 nm–280 nm	0.13 A/W at 272 nm at −20 V	10^2–10^5	1560	1.4×10^{14}	2007	[216]
	Sun Yat-sen University	270 nm	79.8 mA/W at 270 nm at 0 V	—	>2500	—	2010	[217]
	Nanjing University	270 nm–280 nm	132 mA/W at 281 nm at −60 V	10–10^3	3000	—	2012	[218]
	Sun Yat-sen University	244 nm–275 nm	98 mA/W at 262 nm at 0 V	$>10^3$	2000 4000	—	2013	[195]
	Nanjing University	280 nm	0.15 A/W at 280 nm at −15 V	10^3–10^4	1.2×10^4	—	2014	[222]
	Georgia Institute of Technology	200 nm–362 nm	43.4 mA/W at 354 nm at 0 V 221.8 mA/W at 362 nm at −80 V	—	1.5×10^5	—	2015	[223]
	Sun Yat-sen University	250 nm–280 nm	114.1 mA/W at 0 V 145.3 mA/W at −10 V 176.2 mA/W at −20 V	$\sim 10^2$	2×10^4	—	2016	[224]

amplification, two-photon absorption, multiphoton absorption, and self-focusing etc., have been studied and applied. With the development of AlGaN-based active optoelectronic devices, especially the development of DUV and high-power light-emitting devices, nonlinear optical properties of AlGaN materials are becoming more important, and more attention has gradually been attracted. Various approaches are adopted to improve nonlinear optical properties of AlGaN materials, including the Pockels effect, second-harmonic generation, Kerr effect, two-photon absorption effect, multiphoton absorption effect, free-carrier absorption effect, and so on.

On the condition of strong optical field or applied electric field, the nonlinear polarization of a crystal occurs, resulting in the changes of light propagation characteristics, which are the nonlinear optical properties of crystals. The nonlinear optical properties of materials can be expressed with the intensity of polarization,

$$P = \varepsilon_0 \cdot [\chi^{(1)} \cdot E + \chi^{(2)} \cdot EE + \chi^{(3)} \cdot EEE + \cdots], \tag{12}$$

where parameters $\chi^{(1)}$, $\chi^{(2)}$, and $\chi^{(3)}$ are the first-, second-, and third-order tensors of polarizability, respectively. The first term at right introduces linear optical phenomena, the second introduces second-order nonlinear optical phenomena, the third and following terms introduce higher-order nonlinear optical phenomena. The principle of improving nonlinear optical properties of materials is to improve the high-order tensors of polarizability, mainly the second- and third-order tensors of polarizability.

In the early stage, the research on nonlinear optical properties of III-nitrides was stagnating in the measurements and analyses of nonlinear optical parameters. Miragliotta *et al.* [229] investigated the second-order harmonic generation of GaN film. The second-order nonlinear optical tensor of polarizability was obtained. It has been proved experimentally that the application of a direct electric field on the surface of GaN film can damage the inversion symmetry of a crystal, change the distribution state of electrons and holes, and cause the enhancement of the nonlinear optical effect. Afterwards, a very strong second-harmonic generation effect was observed in a bulk GaN film by Sun *et al.* in Taiwan [230]. The effective second-order tensor of polarizability $\chi^{(2)}_{\text{eff}}(2W{:}W,W)$ was calculated to be 2×10^{-12} m/V. In 2003, Sanford *et al.* [104] measured the second-order nonlinear optical tensors of polarizability of a series of GaN and AlGaN films by the method of rotational interference fringe, obtaining the second-order tensor of polarizability of GaN film with $\chi^{(2)}_{31} = -5.7$ pm/V and $\chi^{(2)}_{33} = -9.2$ pm/V. With regard to theoretical research, the second-order optical nonlinearity of WZ GaN and AlN in the wide wave band was calculated by using first principle in 1997 [231]. In 2008, the second-order nonlinear optical responsibility of GaN nanowires with different structures was calculated by using first principle, and the results show that all GaN nanowires with different structures have very strong second-harmonic effect, which indicates the potentials of III-nitride nanowires in nonlinear optical applications [232].

Besides the second-order optical nonlinearity, the third- or even higher-order optical nonlinearity of III-nitride was also investigated. In 1996, the third-order nonlinear refractive index (n_2) of GaN film at 532 nm was first obtained by using degeneration four-wave mixing, with the value of 1×10^{-12} cm^2/W [233]. Afterwards, the third-order nonlinear refractive indices of GaN film at shorter wavelengths were measured by using the femtosecond Z-scanning technique, with the values of -1.4×10^{-12} cm^2/W at 371.2 nm, -2.9×10^{-12} cm^2/W, -1.2×10^{-12} cm^2/W, and -0.5×10^{-12} cm^2/W at 368 nm, 371 nm, and 380 nm, respectively [234].

After eliminating the influence of two-photon absorption on nonlinear refraction, Fazio *et al.* [235] got the nonlinear refractive indices of GaN film at 800 nm with the value of -7.3×10^{-14} cm^2/W. In addition, the phenomena of two-photon and three-photon absorption were reported. In 2000, Krishnamurthy *et al.* [236] calculated the two-photon absorption coefficients (β) of GaN and AlGaN based on the whole energy band structure, obtaining a coherent result with the experiment. Sun *et al.* [234,237] also measured the two-photon absorption coefficients of GaN at different wavelengths, with the results that the third-order nonlinear absorption coefficient at 371.2 nm is −37 cm/GW, and two-photon absorption coefficients at 387 nm, 391 nm, 410 nm, 690 nm, and 720 nm are 17 cm/GW, 16 cm/GW, 12 cm/GW, 7 cm/GW, and 3 cm/GW, respectively. These results indicate that III-nitrides show good nonlinear optical properties from the UV to the visible band. Additionally, Pacebutas *et al.* [238,239] obtained two-photon and three-photon absorption coefficients (β_3) of GaN at 527 nm with the values of 17–20 cm/GW and 0.012 cm^3/GW, and proved the existence of the free-carrier absorption effect. More studies confirmed that there exists two-photon absorption in the defect-related yellow peak in GaN [240], and free carrier and impurity bond carrier can generate nonlinear optical effects [241].

With the research and applications deepening, it is not enough to measure nonlinear optical parameters, but to improve the nonlinear optical properties. The polarization effect induced by the noncentrosymmetry in a WZ AlGaN crystal structure is the main reason of generating nonlinear optical effect. The nonlinear optical coefficient of bulk GaN is still smaller than those of traditional nonlinear optical materials. For example, the electro-optic coefficient of GaN film is only 10% of $KTiOPO_4$. So many approaches were attempted to improve the nonlinear optical effect of AlGaN, importantly to improve the electro-optic effect, namely, the electro-optic coefficient. Based on the lattice and polarization symmetry of AlGaN material, the electro-optic coefficient can be expressed as follows:

$$r_{ij} = \begin{bmatrix} 0 & 0 & r_{13} \\ 0 & 0 & r_{13} \\ 0 & 0 & r_{33} \\ 0 & r_{13} & 0 \\ r_{13} & 0 & 0 \\ 0 & 0 & 0 \end{bmatrix}. \tag{13}$$

At present, a lot of approaches have been proposed to improve nonlinear optical properties of AlGaN material, such as increasing Al content to improve the spontaneous polarization effect, increasing interface mismatch to improve the piezoelectric polarization effect, increasing carrier concentration to change nonlinear absorption, and so on. As the growth technique develops, the epitaxial growth of AlGaN with high Al composition has been able to control accurately, and the internal polarization effect was strengthened by increasing Al content, and further improve nonlinear optical properties of AlGaN [242]. By using a AlGaN/GaN heterostructure, the built-in electrical field and high-concentration two-dimensional electron gas induced by piezoelectric polarization not only improved the second-order nonlinear optical effect, but also the third-order nonlinear optical effect original faint [243]. By using AlGaN/GaN SLs with Al composition of about 0.5, the electro-optic effect was strengthened, realizing a comparable electro-optic coefficient with traditional KDP and $LiNbO_3$ crystals [244]. By using ultrathin strain AlN/GaN SLs, the regulation and control on nonlinear optical properties of AlGaN with average Al composition

higher than 0.5 was realized [245]. In addition, using a AlGaN/GaN step QW structure to improve the second-order polarization rate was also proposed. The simulation showed that the double resonance effect can be realized by calibrating the thickness of well and step well, or Al composition of the barrier and step well [246]. Except for the separated research on the second- and third-order nonlinear optical effects, the research on the interaction between second- and third-order nonlinear optical effects has been investigated [230,243]. However, the mechanism is not clear yet because of the complicated procedure, and further investigation is necessary.

In summary, the improvement of nonlinear optical coefficients is still the most important problem in recent years from the development of nonlinear optics of AlGaN materials. With the increase of Al composition and the decrease of wavelength, it is also an important research direction to measure the nonlinear optical parameters of AlGaN with higher Al composition and wider spectral range. Additionally, besides the electro-optic effect, many other nonlinear optical effects of AlGaN materials, such as harmonic generation, two-photon absorption, three-photon absorption, and nonlinear refractive index, are still to be studied.

6. ALGAN PASSIVE DEVICES AND PHOTONIC INTEGRATED CIRCUIT

In addition to the active photoelectronic devices, it is also important to study the passive photonic devices. A photonic integrated circuit (PIC) is a large-scale network of optical or electronic elements including active photoelectronic devices, such as light-emitters or photodetectors, and passive photonic devices, such as optical limiting devices or optical amplifiers. Since the conception of PIC was proposed by Miller in 1969 [247], the research on PIC based on materials like Si/SiO_2, InP, GaAs, and $LiNbO_3$ never suspends. However, it is until 2004 that a breakthrough had been made on a large-scale PIC containing active and passive devices and that the PIC had been commercial available [248]. Currently, the application of a PIC is still limited to the narrow telecom band.

Except for the telecom band, a UV band PIC will be beneficial to the application areas such as biochemical sensing, beam steering, quantum photonics, UV Raman spectroscopy, and so on. The materials for a UV PIC must meet the requirements of UV optically transparent and low defect density to avoid unwanted optical absorption or autofluoresence [249]. With the development of the III-N-based UV materials and optoelectronic devices and experimental measurements of the linear or nonlinear optical parameters, such as refractive indices, second- or third-order polarizability tensors, people increasingly tend to apply these UV active devices to a PIC, which has the advantages of compact size, low power consumption, high transmission speed and high reliability, realizing monolithic integration of UV optical signal emission, amplification, propagation and detection, and pushing the PIC technique to the UV or DUV band.

Among III-nitrides, InGaN- or GaN-based passive devices developed earlier and microring cavity arrays [250], photonic crystals [251], photonic crystal cavities [252], photonic crystal nanocavities [253], nanophotonic waveguides and resonators [254], and microdisk resonators [255] have been exploited and some high quality (Q) factors have been obtained. Further, GaN on Si passive devices also made some progress. In 2011, Tang *et al.* succeeded in using the GaN/Si microring structure to realize second-harmonic generation at 780 nm and 1560 nm [256]. In 2015, Thuthimhtong *et al.* first achieved a high Q-factor asymmetrically and vertically coupled hybrid Si/GaN microring resonator at the telecom band with a GaN microring and Si waveguide circuit [257]. After the realization of dual mode selection between light emission and

detection by using InGaN/GaN MQWs on a Si-based GaN substrate, the monolithic integration of a LED and PD also became a reality [258–260]. Nevertheless, the integration of nanowire InGaN-based LEDs and PDs has achieved initial success [261–263].

The present AlN-based resonators have a relatively simplex structure, namely a microring structure. Since 2012, Tang *et al.* from Yale University have reported the AlN resonators several times. By using sputtered deposited AlN film on a Si substrate, they realized low-loss waveguides [264] and high Q-factor resonators [265] at infrared and visible bands, reaching a Q-factor as high as 4.4×10^5 at the infrared telecom band. Later, they achieved optical frequency comb at wavelengths of 520 nm, 775 nm, and 1550 nm in their subsequent research [266,267]. Moreover, Sun *et al.* from Tsinghua University applied better-quality MOCVD-grown AlN film to fabricate microring resonators with a high Q-factor of 10^6 magnitude, realizing an all-optically tunable microwave photonic phase shifter [268,269]. Due to the lower crystal quality of AlGaN compared to GaN and AlN, the studies of AlGaN-based passive devices were limited. In 2016, Soltani *et al.* theoretically investigated the propagation characters of AlGaN/AlN waveguides from 300 nm to 700 nm, and predicted their potential application at the deeper UV band [249]. Next year, they further studied the application of AlGaN-based microring resonators on UV band broadband biphoton generation and statistics of quantum light in theory [270]. In respect to experiment, Tang *et al.* adopted the electrochemically sliced AlGaN material to manufacture photon waveguide and resonators, reaching a Q-factor as high as 6.8×10^5 at 780 nm due to the high AlGaN crystal quality [271].

In a word, for the III-nitrides-based passive devices, the wavelength is generally at the visible, infrared, or near-infrared range, and only a few devices work at the UVA range, while the deeper UV range is still under theoretical studies. While for the PIC, most of research focused on improving the single device performance rather than the whole PIC. To realize epitaxial AlN-based low-loss waveguides, it is essential to minimize the scattering and defect-related absorption loss. So it is basically important to improve the AlGaN crystal quality to enhance passive devices and PIC performances.

7. CONCLUSIONS AND OUTLOOK

The crystalline quality of AlN and AlGaN layers has been improved by techniques including HT growth with modulation of the V/III ratio, ALE, NH_3 pulse-flow multilayer growth, use of a SLs as a dislocation filter, ELOG, and several other methods. However, this alone is not enough to enhance the performance of UV devices. Bulk AlN substrates are ideal for AlN and AlGaN growth, but commercial bulk AlN substrates with large area are not available in the market to date. AlN/sapphire templates, which serve as an alternative to bulk AlN substrates, are used for AlN and AlGaN growth. At present, ELOG is regarded as a promising way to grow AlN or AlGaN layers combined with *ex situ* annealing.

The difficulty of p-AlGaN doping with high Al content is mainly caused by the strong self-compensation effect of the material, low dopant solubility, and high activation energy. Several approaches, including codoping, delta-doping, modulation doping, SLs doping, and polarization-induced doping, have been used in attempts to solve these difficulties and improve the doping efficiency. Piezoelectric polarization can reduce the dopant activation energy near the interfaces of heterostructures and can also improve lateral conductivity, but the vertical conductivity remains low. In addition, nonuniform doping approaches are difficult to control and optimize, and this is not advantageous for process industrialization. The next

target in this area is to explore new high-efficiency p-type doping technologies when combined with the good levels of controllability and reproducibility to meet industrial production needs.

AlGaN-based DUV-LEDs with short operating wavelengths have been achieved, and these wavelengths have been extended to 222 nm for AlGaN/AlN MQW devices and 210 nm for AlN PIN homojunction devices. The improved performances of these LEDs have been achieved with EQEs of 20.3% at 275 nm. However, the EQEs of DUV-LEDs are still low when compared with those of GaN-based blue and green LEDs. There is also a considerable drop in efficiency, which is caused by high dislocation densities, low hole concentrations, and low LEEs for the AlGaN-based LEDs. Furthermore, the EQE also drops dramatically with decreasing wavelength, which is caused by deterioration in the AlGaN quality, the difficulty of p-type doping processes, and degradation of the optically polarized emission with increasing Al content. It is expected that high-efficiency DUV AlGaN-based LEDs will be realized by improving the quality and the p-type doping of AlGaN as well as optimizing the parameters of the AlGaN/AlN MQWs.

With the advantages of simple structures and free of p-type layers, EB-pumped AlGaN-based DUV light sources have been developed, and DUV light emission has been realized at a wavelength of 238 nm, with output power of 100 mW and a PCE of 40%. However, these output characteristics are still unsatisfactory for many applications, and many challenges remain in terms of device fabrication. Further optimization and improvements in the device structure and fabrication processes will be required to realize high-performance devices.

Due to the improvements in both AlGaN quality and p-type doping, UV stimulated emission has been achieved in AlGaN MQW LDs using electrical pumping at RT, with a shortest reported wavelength of 336 nm. At present, the development of UV AlGaN-based LDs is moving toward shorter wavelengths. However, it is particularly difficult to achieve electrically pumped stimulated emission from LDs in the UV-C bands. Many challenges must be overcome to achieve high-performance LDs of this type. First, the high densities of defects and dislocations in the active regions of these LDs will increase their internal losses, resulting in reduction of the EQE. Second, the difficulty involved in p-type doping of AlGaN will reduce the hole injection efficiency and increase the series resistance, which leads to an increased threshold and reduced efficiency for LDs operating under current injection conditions. Additionally, the difficulties faced in device fabrication processes such as etching, thinning, and cleaving will increase losses and reduce the efficiency of these LDs. In addition, suitable homoepitaxial substrates for AlGaN growth are not available at present. Therefore, appropriate substrates with high transparency and high electrical and thermal conductivities are required to improve the performance of these LDs. Furthermore, a suitable LD structure design is required to improve device efficiency. In conclusion, the low defect densities of bulk AlN substrates offer a promising strategy to enable fabrication of high-performance LDs.

While considerable research progress has been made in the development of AlGaN-based UV-PDs, the current device performance is still far from the goals of weak signal detection or even SPD. How to realize the UV-PDs with low noise, fast response speeds, and high gains are expected. The traditional AlGaN PD cannot detect the weak signal due to lack of gain. AlGaN APDs can solve this problem and a gain of as high as 10^4 has been achieved using the SAM-APD structure. However, it remains difficult to detect weak signals using this structure because of the small effective device area. Surface plasmon is regarded as a promising

way to realize high spectral response but it is just used in the MSM-AlGaN PDs and how to use the surface plasmon into pin-AlGaN is still a problem. In a word, both the quality of AlGaN and the structure of devices need to be optimized for weak single detecting.

Although the nonlinear optical properties of AlGaN were less studied compared to LEDs, LDs and PDs, they are becoming more important as the increasing output light power. And the AlGaN-based nonlinear optical devices were not widely applied due to the comparatively low nonlinear optical coefficients, thus the primary task is to increase the nonlinear optical coefficients. In addition, the measurements of these coefficients at different wavelengths, shorter wavelengths, and different Al content AlGaN are required. AlGaN-based passive devices and PIC are generally based on high-quality materials and high-performance active devices. Thus the motivation to develop AlGaN-based passive devices and PIC put forward high requirements involving promoting crystal quality and optimizing the performances of active devices.

FUNDING

National Key R&D Program of China (2016YFB0400101, 2016YFB0400900); National Science Fund for Distinguished Young Scholars (61725403); National Natural Science Foundation of China (NSFC) (61574142, 61322406); Key Program of the International Partnership Program of CAS (181722KYSB20160015); Special Project for Inter-government Collaboration of the State Key Research and Development Program (2016YFE0118400); Jilin Provincial Science & Technology Department (20150519001JH); CAS Interdisciplinary Innovation Team; Youth Innovation Promotion Association of CAS (2015171).

ACKNOWLEDGMENT

The authors give special thanks to Dr. Yong Wang, Jianwei Ben, Xiaotong Liu, Yuping Jia, Yinghao Fu, You Wu, Cuihong Kai, and Henan Liu for their valuable discussion and suggestions. Additionally, the authors also would like to thank the publishing companies for their permissions to reproduce figures from their websites.

REFERENCES

1. A. R. Denton and N. W. Ashcroft, "Vegard's law," Phys. Rev. A **43**, 3161–3164 (1991).
2. D. Fritsch, H. Schmidt, and M. Grundmann, "Band-structure pseudopotential calculation of zinc-blende and wurtzite AlN, GaN, and InN," Phys. Rev. B **67**, 235205 (2003).
3. M. Suzuki, T. Uenoyama, and A. Yanase, "First-principles calculations of effective-mass parameters of AlN and GaN," Phys. Rev. B **52**, 8132–8139 (1995).
4. H. S. Kim, R. A. Mair, J. Li, J. Y. Lin, and H. X. Jiang, "Time-resolved photoluminescence studies of $Al_xGa_{1-x}N$ alloys," Appl. Phys. Lett. **76**, 1252–1254 (2000).
5. I. Vurgaftman and J. R. Meyer, "Band parameters for nitrogen-containing semiconductors," J. Appl. Phys. **94**, 3675–3696 (2003).
6. M. E. Levinshtein, S. L. Rumyantsev, and M. S. Shur, *Properties of Advanced Semiconductor Materials: GaN, AlN, InN, BN, SiC, SiGe* (Wiley, 2001), http://www.gbv.de/dms/ilmenau/toc/314774785.PDF.

7. R. G. Banal, "MOVPE growth of AlN and AlGaN/AlN quantum wells and their optical polarization properties," Ph.D. dissertation (Kyoto University, 2009), https://dx.doi.org/10.14989/doctor.k14627.
8. M. Kuball, "Raman spectroscopy of GaN, AlGaN and AlN for process and growth monitoring/control," Surf. Interface Anal. **31**, 987–999 (2001).
9. F. Bernardini, V. Fiorentini, and D. Vanderbilt, "Spontaneous polarization and piezoelectric constants of III-V nitrides," Phys. Rev. B **56**, R10024 (1997).
10. E. W. Van Stryland, H. Vanherzeele, M. A. Woodall, M. J. Soileau, A. L. Smirl, S. Guha, and T. F. Boggess, "Two-photon absorption, nonlinear refraction and optical limiting in semiconductors," Opt. Eng. **24**, 244613 (1985).
11. A. M. Streltsov, K. D. Moll, A. L. Gaeta, P. Kung, D. Walker, and M. Razeghi, "Pulse autocorrelation measurements based on two-and three-photon conductivity in a GaN photodiode," Appl. Phys. Lett. **75**, 3778–3780 (1999).
12. S. Tatsuura, M. Furuki, Y. Sato, I. Iwasa, M. Tian, and H. Mitsu, "Semiconductor carbon nanotubes as ultrafast switching materials for optical telecommunications," Adv. Mater. **15**, 534–537 (2003).
13. D. B. Li, M. Aoki, T. Katsuno, H. Miyake, K. Hiramatsu, and T. Shibata, "Influence of growth conditions on Al incorporation to $Al_xGa_{1-x}N$ ($x > 0.4$) grown by MOVPE," J. Cryst. Growth **298**, 372–374 (2007).
14. C. G. Van de Walle and J. Neugebauer, "First-principles calculations for defects and impurities: applications to III-nitrides," J. Appl. Phys. **95**, 3851–3879 (2004).
15. T. C. Zheng, W. Lin, D. J. Cai, W. H. Yang, W. Jiang, H. Y. Chen, J. C. Li, S. P. Li, and J. Y. Kang, "High Mg effective incorporation in Al-rich $Al_xGa_{1-x}N$ by periodic repetition of ultimate V/III ratio conditions," Nano. Res. Lett. **9**, 40 (2014).
16. S. F. Fan, Z. X. Qin, C. G. He, M. J. Hou, X. Q. Wang, B. Shen, W. Li, W. Y. Wang, D. F. Mao, P. Jin, J. C. Yan, and P. Dong, "Optical investigation of strong exciton localization in high Al composition $Al_xGa_{1-x}N$ alloys," Opt. Express **21**, 24497–24503 (2013).
17. K. B. Nam, M. L. Nakarmi, J. Li, J. Y. Lin, and H. X. Jiang, "Mg acceptor level in AlN probed by deep ultraviolet photoluminescence," Appl. Phys. Lett. **83**, 878–880 (2003).
18. K. M. Taylor and C. Lenie, "Some properties of aluminum nitride," J. Electrochem. Soc. **107**, 308–314 (1960).
19. J. Pastrnak and L. Roskovcova, "Morphologie und Wachstumsmechanismus von AIN-Einkristallen," Phys. Status Solidi **7**, 331–338 (1964).
20. H. M. Manasevit, F. M. Erdmann, and W. I. Simpson, "The use of metalorganics in the preparation of semiconductor materials IV. The nitrides of aluminum and gallium," J. Electrochem. Soc. **118**, 1864–1868 (1971).
21. R. Rutz, "Ultraviolet electroluminescence in AlN," Appl. Phys. Lett. **28**, 379–381 (1976).
22. W. M. Yim, E. J. Stofko, P. J. Zanzucchi, J. I. Pankove, and M. Ettenberg, "Epitaxially grown AlN and its optical band gap," J. Appl. Phys. **44**, 292–296 (1973).
23. D. K. Wickenden, K. R. Faulkner, R. W. Brander, and B. J. Isherwood, "Growth of epitaxial layers of gallium nitride on silicon carbide and corundum substrates," J. Cryst. Growth **9**, 158–164 (1971).
24. B. Baranov, L. Daweritz, V. B. Gutan, G. Jungk, H. Neumann, and H. Raidt, "Growth and properties of AlGaN epitaxial layers," Phys. Status Solidi A **49**, 629–636 (1978).
25. S. Yoshida, S. Misawa, and S. Gonda, "Properties of AlGaN films prepared by reactive molecular beam epitaxy," J. Appl. Phys. **53**, 6844–6848 (1982).

26. M. A. Khan, R. A. Skogman, R. G. Schulze, and M. Gershenzon, "Properties and ion implantation of $Al_xGa_{1-x}N$ epitaxial single crystal films prepared by low pressure metalorganic chemical vapor deposition," Appl. Phys. Lett. **43**, 492–494 (1983).
27. Y. Koide, N. Itoh, K. Itoh, N. Wawaki, and I. Akasaki, "Effect of AlN buffer layer on AlGaN/α-Al_2O_3 heteroepitaxial growth by metalorganic vapor phase epitaxy," Jpn. J. Appl. Phys. **27**, 1156–1161 (1988).
28. K. Ito, K. Hiramatsu, H. Amano, and I. Akasaki, "Preparation of $Al_xGa_{1-x}N$/GaN heterostructure by MOVPE," J. Cryst. Growth **104**, 533–538 (1990).
29. K. Ban, J. Yamamoto, K. Takeda, K. Ide, M. Iwaya, T. Takeuchi, S. Kamiyama, I. Akasaki, and H. Amano, "Internal quantum efficiency of whole-composition-range AlGaN multiquantum wells," Appl. Phys. Express **4**, 052101 (2011).
30. S. Kamiyama, M. Iwaya, N. Hayashi, T. Takeuchi, H. Amano, I. Akasaki, S. Watanabe, Y. Kaneko, and N. Yamada, "Low-temperature-deposited AlGaN interlayer for improvement of AlGaN/GaN heterostructure," J. Cryst. Growth **223**, 83–91 (2001).
31. Y. Kida, T. Shibata, H. Miyake, and K. Hiramatsu, "Metalorganic vapor phase epitaxy growth and study of stress in AlGaN using epitaxial AlN as underlying layer," Jpn. J. Appl. Phys. **42**, L572–L574 (2003).
32. C. Hartmann, J. Wollweber, A. Dittmar, K. Irmscher, A. Kwasniewski, F. Langhans, T. Neugut, and M. Bickermann, "Preparation of bulk AlN seeds by spontaneous nucleation of freestanding crystals," Jpn. J. Appl. Phys. **52**, 08JA06 (2013).
33. Z. G. Herro, D. Zhuang, R. Schlesser, and Z. Sitar, "Growth of AlN single crystalline boules," J. Cryst. Growth **312**, 2519–2521 (2010).
34. R. Dalmau, B. Moody, J. Q. Xie, R. Collazo, and Z. Sitar, "Characterization of dislocation arrays in AlN single crystals grown by PVT," Phys. Status Solidi A **208**, 1545–1547 (2011).
35. R. R. Sumathi, "Bulk AlN single crystal growth on foreign substrate and preparation of free-standing native seeds," CrystEngComm **15**, 2232–2240 (2013).
36. "AlN substrate products," http://www.hexatechinc.com/aln-wafer-sales.html.
37. E. Mokhov, I. Izmaylova, O. Kazarova, A. Wolfson, S. Nagalyuk, D. Litvin, A. Vasiliev, H. Helava, and Y. Makarov, "Specific features of sublimation growth of bulk AlN crystals on SiC wafers," Phys. Status Solidi C **10**, 445–448 (2013).
38. R. T. Bondokov, S. G. Mueller, K. E. Morgan, G. A. Slack, S. Schujman, M. C. Wood, J. A. Smart, and L. J. Schowalter, "Large-area AlN substrates for electronic applications: an industrial perspective," J. Cryst. Growth **310**, 4020–4026 (2008).
39. T. Baker, A. Mayo, Z. Veisi, P. Lu, and J. Schmitt, "High temperature HVPE of AlN on sapphire templates," Phys. Status Solidi C **11**, 373–376 (2014).
40. H. Jeon, C. Lee, C. Lee, M. Yang, S. N. Yi, H. S. Ahn, Y. M. Yu, S. C. Lee, S. W. Kim, and N. Sawaki, "Thick AlN epilayer grown by using the HVPE method," J. Korean Phys. Soc. **67**, 643–647 (2015).
41. H. Miyake, G. Nishio, S. Suzuki, K. Hiramatsu, H. Fukuyama, J. Kaur, and N. Kuwano, "Annealing of an AlN buffer layer in N_2–CO for growth of a high-quality AlN film on sapphire," Appl. Phys. Express **9**, 025501 (2016).
42. S. M. Kim, T. Y. Park, S. J. Park, S. J. Lee, J. H. Baek, Y. C. Park, and G. Y. Jung, "Nanopatterned aluminum nitride template for high efficiency light-emitting diodes," Opt. Express **17**, 14791–14799 (2009).

43. Y. Kumagai, T. Yamane, T. Miyaji, H. Murakami, Y. Kangawa, and A. Koukitu, "Hydride vapor phase epitaxy of AlN: thermodynamic analysis of aluminum source and its application to growth," Phys. Status Solidi C **0**, 2498–2501 (2003).
44. X. J. Sun, D. B. Li, Y. R. Chen, H. Song, H. Jiang, Z. M. Li, G. Q. Miao, and Z. Zhang, "In situ observation of two-step growth of AlN on sapphire using high-temperature metal-organic chemical vapour deposition," CrystEngComm **15**, 6066–6073 (2013).
45. O. Rettig, "Investigation of AlBGaN structures for UV-lighting," Annual Report 2015 (Institute of Optoelectronics, Ulm University, 2015), pp. 65–70.
46. X. H. Li, S. Wang, H. G. Xie, Y. O. Wei, T. T. Kao, M. M. Satter, S. C. Shen, P. D. Yoder, T. Detchprohm, R. D. Dupuis, A. M. Fischer, and F. A. Ponce, "Growth of high-quality AlN layers on sapphire substrates at relatively low temperatures by metalorganic chemical vapor deposition," Phys. Status Solidi B **252**, 1089–1095 (2015).
47. M. L. Nakarmi, B. Cai, J. Y. Lin, and H. X. Jiang, "Three-step growth method for high quality AlN epilayers," Phys. Status Solidi A **209**, 126–129 (2012).
48. A. Yoshikawa, T. Nagatomi, T. Morishita, M. Iwaya, T. Takeuchi, S. Kamiyama, and I. Akasaki, "High-quality AlN film grown on a nanosized concave-convex surface sapphire substrate by metalorganic vapor phase epitaxy," Appl. Phys. Lett. **111**, 162102 (2017).
49. M. Imura, K. Nakano, N. Fujimoto, N. Okada, K. Balakrishnan, K. Balakrishnan, M. Iwaya, S. Kamiyama, H. Amano, I. Akasaki, T. Noro, T. Takagi, and A. Bandoh, "High-temperature metal-organic vapor phase epitaxial growth of AlN on sapphire by multi transition growth mode method varying V/III ratio," Jpn. J. Appl. Phys. **45**, 8639–8643 (2006).
50. M. Imura, N. Fujimoto, N. Okada, K. Balakrishnan, M. Iwaya, S. Kamiyama, H. Amano, I. Akasaki, T. Noro, T. Takagi, and A. Bandoh, "Annihilation mechanism of threading dislocations in AlN grown by growth form modification method using V/III ratio," J. Cryst. Growth **300**, 136–140 (2007).
51. K. Balakrishnan, A. Bandoh, M. Iwaya, S. Kamiyama, H. Amano, and I. Akasaki, "Influence of high temperature in the growth of low dislocation content AlN bridge layers on patterned 6H-SiC substrates by metalorganic vapor phase epitaxy," Jpn. J. Appl. Phys. **46**, L307–L310 (2007).
52. J. P. Zhang, M. A. Khan, W. H. Sun, H. M. Wang, C. Q. Chen, Q. Fareed, E. Kuokstis, and J. W. Yang, "Pulsed atomic-layer epitaxy of ultrahigh-quality $Al_xGa_{1-x}N$ structures for deep ultraviolet emissions below 230 nm," Appl. Phys. Lett. **81**, 4392–4394 (2002).
53. R. G. Banal, M. Funato, and Y. Kawakami, "Initial nucleation of AlN grown directly on sapphire substrates by metal-organic vapor phase epitaxy," Appl. Phys. Lett. **92**, 241905 (2008).
54. R. G. Banal, M. Funato, and Y. Kawakami, "Characteristics of high Al-content AlGaN/AlN quantum wells fabricated by modified migration enhanced epitaxy," Phys. Status Solidi C **7**, 2111–2114 (2010).
55. H. Hirayama, S. Fujikawa, N. Noguchi, J. Norimatsu, T. Takano, K. Tsubaki, and N. Kamata, "222–282 nm AlGaN and InAlGaN-based deep-UV LEDs fabricated on high-quality AlN on sapphire," Phys. Status Solidi A **206**, 1176–1182 (2009).
56. H. Hirayama, J. Norimatsu, N. Noguchi, S. Fujikawa, T. Takano, K. Tsubaki, and N. Kamata, "Milliwatt power 270 nm-band AlGaN deep-UV LEDs fabricated on ELO-AlN templates," Phys. Status Solidi C **6**, S474–S477 (2009).
57. J. P. Zhang, H. M. Wang, M. E. Gaevski, C. Q. Chen, Q. Fareed, J. W. Yang, G. Simin, and M. Asif Khan, "Crack-free thick AlGaN grown on sapphire using

AlN/AlGaN superlattices for strain management," Appl. Phys. Lett. **80**, 3542–3544 (2002).
58. H. M. Wang, J. P. Zhang, C. Q. Chen, Q. Fareed, J. W. Yang, and M. A. Khan, "AlN/AlGaN superlattices as dislocation filter for low-threading-dislocation thick AlGaN layers on sapphire," Appl. Phys. Lett. **81**, 604–606 (2002).
59. W. H. Sun, J. P. Zhang, J. W. Yang, H. P. Maruska, M. A. Khan, R. Liu, and F. A. Ponce, "Fine structure of AlN/AlGaN superlattices grown by pulsed atomic-layer epitaxy for dislocation filtering," Appl. Phys. Lett. **87**, 211915 (2005).
60. M. Kim, T. Fujita, S. Fukahori, T. Inazu, C. Pernot, Y. Nagasawa, A. Hirano, M. Ippommatsu, M. Iwaya, T. Takeuchi, S. Kamiyama, M. Yamaguchi, Y. Honda, H. Amano, and I. Akasaki, "AlGaN-based deep ultraviolet light-emitting diodes fabricated on patterned sapphire substrates," Appl. Phys. Express **4**, 092102 (2011).
61. H. Miyake, C. H. Lin, K. Tokoro, and K. Hiramatsu, "Preparation of high-quality AlN on sapphire by high-temperature face-to-face annealing," J. Cryst. Growth **456**, 155–159 (2016).
62. R. Jain, W. Sun, J. Yang, M. Shatalov, X. Hu, A. Sattu, A. Lnev, J. Deng, I. Shturm, Y. Belenko, R. Gaska, and M. S. Shur, "Migration enhanced lateral epitaxial overgrowth of AlN and AlGaN for high reliability deep ultraviolet light emitting diodes," Appl. Phys. Lett. **93**, 051113 (2008).
63. B. T. Tran, N. Maeda, M. Jo, D. Inoue, T. Kikitsu, and H. Hirayama, "Performance improvement of AlN crystal quality grown on patterned Si(111) substrate for deep UV-LED applications," Sci. Rep. **6**, 35681 (2016).
64. P. Dong, J. C. Yan, Y. Zhang, J. X. Wang, J. P. Zeng, C. Geng, P. P. Cong, L. L. Sun, T. B. Wei, L. X. Zhao, Q. F. Yan, C. G. He, Z. X. Qin, and J. M. Li, "AlGaN-based deep ultraviolet light-emitting diodes grown on nano-patterned sapphire substrates with significant improvement in internal quantum efficiency," J. Cryst. Growth **395**, 9–13 (2014).
65. L. S. Zhang, F. J. Xu, J. M. Wang, C. G. He, W. W. Guo, M. G. Wang, B. W. Sheng, L. Lu, Z. X. Qin, X. Q. Wang, and B. Shen, "High-quality AlN epitaxy on nano-patterned sapphire substrates prepared by nano-imprint lithography," Sci. Rep. **6**, 35934 (2016).
66. V. Kueller, A. Knauer, C. Reich, A. Mogilatenko, M. Weyers, J. Stellmach, T. Wernicke, M. Kneissl, Z. Yang, C. L. Chua, and N. M. Johnson, "Modulated epitaxial lateral overgrowth of AlN for efficient UV LEDs," IEEE Photon. Technol. Lett. **24**, 1603–1605 (2012).
67. V. Kueller, A. Knauer, U. Zeimer, M. Kneissl, and M. Weyers, "Controlled coalescence of MOVPE grown AlN during lateral overgrowth," J. Cryst. Growth **368**, 83–86 (2013).
68. K. Forghani, M. Klein, F. Lipski, S. Schwaiger, J. Hertkorn, R. A. R. Leute, F. Scholz, M. Feneberg, B. Neuschl, K. Thonke, O. Klein, U. Kaiser, R. Gutt, and T. Passow, "High quality AlGaN epilayers grown on sapphire using SiN_x interlayers," J. Cryst. Growth **315**, 216–219 (2011).
69. M. Conroy, V. Z. Zubialevich, H. N. Li, N. Petkov, J. D. Holmes, and P. J. Parbrook, "Epitaxial lateral overgrowth of AlN on self-assembled patterned nanorods," J. Mater. Chem. C **3**, 431–437 (2015).
70. Y. Ohba, H. Yoshida, and R. Sato, "Growth of high-quality AlN, GaN and AlGaN with atomically smooth surfaces on sapphire substrates," Jpn. J. Appl. Phys. **36**, L1565–L1567 (1997).
71. X. Chen, J. C. Yan, Y. Zhang, Y. D. Tian, Y. N. Guo, S. Zhang, T. B. Wei, J. X. Wang, and J. M. Li, "Improved crystalline quality of AlN by epitaxial lateral overgrowth using two-phase growth method for deep-ultraviolet stimulated emission," IEEE Photon. J. **8**, 2300211 (2016).

72. H. Fukuyama, H. Miyake, G. Nishio, S. Suzuki, and K. Hiramatsu, "Impact of high-temperature annealing of AlN layer on sapphire and its thermodynamic principle," Jpn. J. Appl. Phys. **55**, 05FL02 (2016).
73. P. Cantu, S. Keller, and U. K. Mishra, "Metalorganic chemical vapor deposition of highly conductive $Al_{0.65}Ga_{0.35}N$ films," Appl. Phys. Lett. **82**, 3683–3685 (2003).
74. T. M. Altahtamouni, A. Sedhain, J. Y. Lin, and H. X. Jiang, "Si-doped high Al-content AlGaN epilayers with improved quality and conductivity using indium as a surfactant," Appl. Phys. Lett. **92**, 092105 (2008).
75. S. C. Wang, X. Zhang, M. Zhu, F. D. Li, and Y. P. Cui, "Crack-free Si-doped n-AlGaN film grown on sapphire substrate with high-temperature AlN interlayer," Optik **126**, 3698–3702 (2015).
76. C. G. He, Z. X. Qin, F. J. Xu, L. S. Zhang, M. X. Wang, M. J. Hou, W. W. Guo, S. Zhang, X. Q. Wang, and B. Shen, "Growth of high quality n-$Al_{0.5}Ga_{0.5}N$ thick films by MOCVD," Mater. Lett. **176**, 298–300 (2016).
77. S. X. Zhu, J. C. Yan, Y. Zhang, J. P. Zeng, Z. Si, P. Dong, J. M. Li, and J. X. Wang, "The effect of delta-doping on Si-doped Al rich n-AlGaN on AlN template grown by MOCVD," Phys. Status Solidi C **11**, 466–468 (2014).
78. R. Adhikari, T. Li, G. Capuzzo, and A. Bonanni, "Controlling a three dimensional electron slab of graded $Al_xGa_{1-x}N$," Appl. Phys. Lett. **108**, 022105 (2016).
79. S. B. Li, T. Zhang, J. Wu, Y. J. Yang, Z. M. Wang, Z. M. Wu, Z. Chen, and Y. D. Jiang, "Polarization induced hole doping in graded $Al_xGa_{1-x}N$ ($x = 0.7$–1) layer grown by molecular beam epitaxy," Appl. Phys. Lett. **102**, 062108 (2013).
80. Y. D. Chen, H. L. Wu, E. Han, G. L. Yue, Z. M. Chen, Z. S. Wu, G. Wang, and H. Jiang, "High hole concentration in p-type AlGaN by indium-surfactant-assisted Mg-delta doping," Appl. Phys. Lett. **106**, 162102 (2015).
81. K. S. Kim, M. S. Han, G. M. Yang, C. J. Youn, H. J. Lee, H. K. Cho, and J. Y. Lee, "Codoping characteristics of Zn with Mg in GaN," Appl. Phys. Lett. **77**, 1123–1125 (2000).
82. T. Mattila and R. M. Nieminen, "Point-defect complexes and broadband luminescence in GaN and AlN," Phys. Rev. B **55**, 9571–9576 (1997).
83. M. L. Nakarmi, K. H. Kim, J. Li, J. Y. Lin, and H. X. Jiang, "Enhanced p-type conduction in GaN and AlGaN by Mg-δ-doping," Appl. Phys. Lett. **82**, 3041–3043 (2003).
84. J. Li, T. N. Oder, M. L. Nakarmi, J. Y. Lin, and H. X. Jiang, "Optical and electrical properties of Mg-doped p-type $Al_xGa_{1-x}N$," Appl. Phys. Lett. **80**, 1210–1212 (2002).
85. M. L. Nakarmi, K. H. Kim, M. Khizar, Z. Y. Fan, J. Y. Lin, and H. X. Jiang, "Electrical and optical properties of Mg-doped $Al_{0.7}Ga_{0.3}N$ alloys," Appl. Phys. Lett. **86**, 092108 (2005).
86. H. K. Cho, J. Y. Lee, S. R. Jeon, and G. M. Yang, "Influence of Mg doping on structural defects in AlGaN layers grown by metalorganic chemical vapor deposition," Appl. Phys. Lett. **79**, 3788–3790 (2001).
87. S. R. Jeon, Z. Ren, G. Cui, J. Su, M. Gherasimova, and J. Han, "Investigation of Mg doping in high-Al content p-type $Al_xGa_{1-x}N$ ($0.3 < x < 0.5$)," Appl. Phys. Lett. **86**, 082107 (2005).
88. T. Kinoshita, T. Obata, H. Yanagi, and S. Inoue, "High p-type conduction in high-Al content Mg-doped AlGaN," Appl. Phys. Lett. **102**, 012105 (2013).
89. J. Neugebauer and C. G. Van de Walle, "Role of hydrogen in doping of GaN," Appl. Phys. Lett. **68**, 1829–1831 (1996).

90. M. E. Zvanut, U. R. Sunay, J. Dashdorj, W. R. Willoughby, and A. A. Allerman, "Mg-hydrogen interaction in AlGaN alloys," Proc. SPIE **8262**, 82620L (2012).
91. P. Kozodoy, M. Hansen, S. P. DenBaars, and U. K. Mishra, "Enhanced Mg doping efficiency in $Al_{0.2}Ga_{0.8}N$/GaN superlattices," Appl. Phys. Lett. **74**, 3681–3683 (1999).
92. K. Kumakura, T. Makimoto, and N. Kobayashi, "Enhanced hole generation in Mg-doped AlGaN/GaN superlattices due to piezoelectric field," Jpn. J. Appl. Phys. **39**, 2428–2430 (2000).
93. E. L. Waldron, J. W. Graff, and E. F. Schubert, "Improved mobilities and resistivities in modulation-doped p-type AlGaN/GaN superlattices," Appl. Phys. Lett. **79**, 2737–2739 (2001).
94. Y. Aoyagi, M. Takeuchi, S. Iwai, and H. Hirayama, "High hole carrier concentration realized by alternative co-doping technique in metal organic chemical vapor deposition," Appl. Phys. Lett. **99**, 112110 (2011).
95. G. Kipshidze, V. Kuryatkov, B. Borisov, Y. Kudryavtsev, R. Asomoza, S. Nikishin, and H. Temkin, "Mg and O codoping in p-type GaN and $Al_xGa_{1-x}N$ ($0 < x < 0.08$)," Appl. Phys. Lett. **80**, 2910–2912 (2002).
96. Z. Y. Xu, Z. X. Qin, L. W. Sang, Y. Z. Zhang, B. Shen, G. Y. Zhang, L. Zhao, X. F. Zhang, C. J. Cheng, and W. G. Sun, "Effect of indium ambient on electrical properties of Mg-doped $Al_xGa_{1-x}N$," Chin. Phys. Lett. **27**, 127304 (2010).
97. Z. Q. Liu, A. G. Melton, X. Y. Yi, J. W. Wang, B. Kucukgok, J. Kang, N. Lu, J. X. Wang, J. M. Li, and L. Ferguson, "Design of shallow acceptors in GaN through zinc-magnesium codoping: first-principles calculation," Appl. Phys. Express **6**, 042104 (2013).
98. J. C. Li, W. H. Yang, S. P. Li, H. Y. Chen, D. Y. Liu, and J. Y. Kang, "Enhancement of p-type conductivity by modifying the internal electric field in Mg- and Si-δ-codoped $Al_xGa_{1-x}N/Al_yGa_{1-y}N$ superlattices," Appl. Phys. Lett. **95**, 151113 (2009).
99. J. Simon, V. Protasenko, C. X. Lian, H. L. Xing, and D. Jena, "Polarization-induced hole doping in wide-band-gap uniaxial semiconductor heterostructures," Science **327**, 60–64 (2010).
100. L. Zhang, K. Ding, J. C. Yan, J. X. Wang, Y. P. Zeng, T. B. Wei, Y. Y. Li, B. J. Sun, R. F. Duan, and J. M. Li, "Three-dimensional hole gas induced by polarization in (0001)-oriented metal-face III-nitride structure," Appl. Phys. Lett. **97**, 062103 (2010).
101. T. C. Zheng, W. Lin, R. Liu, D. J. Cai, J. C. Li, S. P. Li, and J. Y. Kang, "Improved p-type conductivity in Al-rich AlGaN using multidimensional Mg-doped superlattices," Sci. Rep. **6**, 21897 (2016).
102. H. Kawanishi and T. Tomizawa, "Carbon-doped p-type (0001) plane AlGaN (Al = 6-55%) with high hole density," Phys. Status Solidi B **249**, 459–463 (2012).
103. X. W. Zhou, P. X. Li, S. R. Xu, and Y. Hao, "Growth and electrical properties of high-quality Mg-doped p-type $Al_{0.2}Ga_{0.8}N$ films," J. Semicond. **30**, 043002 (2009).
104. N. A. Sanford, L. H. Robins, A. V. Davydov, A. Shapiro, D. V. Tsvetkov, A. V. Dmitriev, S. Keller, U. K. Mishra, and S. P. DenBaars, "Refractive index study of $Al_xGa_{1-x}N$ films grown on sapphire substrates," J. Appl. Phys. **94**, 2980–2991 (2003).
105. N. A. Sanford, A. V. Davydov, D. V. Tsvetkov, A. V. Dmitriev, S. Keller, U. K. Mishra, S. S. Park, J. Y. Han, and R. J. Molnar, "Measurement of second order susceptibilities of GaN and AlGaN," J. Appl. Phys. **97**, 053512 (2005).

106. S. H. Park and J. I. Shim, "Carrier density dependence of polarization switching characteristics of light emission in deep-ultraviolet AlGaN/AlN quantum well structures," Appl. Phys. Lett. **102**, 221109 (2013).
107. T. M. Altahtamouni, J. Y. Lin, and H. X. Jiang, "Optical polarization in c-plane Al-rich AlN/$Al_xGa_{1-x}N$ single quantum wells," Appl. Phys. Lett. **101**, 042103 (2012).
108. J. Zhang, H. P. Zhao, and N. Tansu, "Effect of crystal-field split-off hole and HH bands crossover on gain characteristics of high Al-content AlGaN QW lasers," Appl. Phys. Lett. **97**, 111105 (2010).
109. I. Akasaki and H. Amano, "Conductivity control of AlGaN fabrication of AlGaN/GaN multi-heterostructure and their application to UV/blue light emitting devices," Mater. Res. Soc. Symp. Proc. **242**, 383 (1992).
110. J. Han, M. H. Crawford, R. J. Shul, J. J. Figiel, M. Banas, L. Zhang, Y. K. Song, H. Zhou, and A. V. Nurmikko, "AlGaN/GaN quantum well ultraviolet light emitting diodes," Appl. Phys. Lett. **73**, 1688–1690 (1998).
111. T. Nishida and N. Kobayashi, "346 nm emission from AlGaN multi-quantum-well light emitting diode," Phys. Status Solidi A **176**, 45–48 (1999).
112. A. Kinoshita, H. Hirayama, M. Ainoya, Y. Aoyagi, and A. Hirata, "Room-temperature operation at 333 nm of $Al_{0.03}Ga_{0.97}N/Al_{0.25}Ga_{0.75}N$ quantumwell light-emitting diodes with Mg-doped superlattices layers," Appl. Phys. Lett. **77**, 175–177 (2000).
113. H. Hirayama, Y. Enomoto, A. Kinoshita, A. Hirata, and Y. Aoyagi, "230 to 250 nm intense emission from AlN-AlGaN quantum wells," Phys. Status Solidi A **180**, 157–161 (2000).
114. Y. Taniyasu, M. Kasu, and T. Makimoto, "An aluminum nitride light-emitting diode with a wavelength of 210 nanometres," Nature **441**, 325–328 (2006).
115. H. Hirayama, "Growth techniques of AlN/AlGaN and development of high-efficiency deep-ultraviolet light-emitting diodes," in *III-Nitride Ultraviolet Emitters*, Vol. **227** of Springer Series in Materials Science (Springer, 2016).
116. M. Shatalov, W. H. Sun, A. Lunev, X. H. Hu, A. Dobrinsky, Y. Bilenko, J. W. Yang, M. Shur, R. Gaska, C. Moe, G. Garrett, and M. Wraback, "AlGaN deep-ultraviolet LEDs with external quantum efficiency above 10%," Appl. Phys. Express **5**, 082101 (2012).
117. M. Shatalov, J. W. Yang, Y. Bilenko, M. Shur, and R. Gaska, "AlGaN deep ultraviolet LEDs with external quantum efficiency over 10%," in *Conference on Lasers and Electro-Optics Pacific Rim (CLEO-PR)* (2013), paper MH1-2.
118. M. Shatalov, W. H. Sun, R. Jain, A. Lunev, and X. H. Hu, "High power AlGaN ultraviolet light emitters," Semicond. Sci. Technol. **29**, 084007 (2014).
119. M. Shatalov, R. Jaina, A. Dobrinskya, W. H. Suna, and Y. Bilenko, "High efficiency UV LEDs on sapphire," Proc. SPIE **9363**, 93631M (2015).
120. T. Takano, T. Mino, J. Sakai, N. Noguchi, K. Tsubaki, and H. Hirayama, "Deep-ultraviolet light-emitting diodes with external quantum efficiency higher than 20% at 275 nm achieved by improving light-extraction efficiency," Appl. Phys. Express **10**, 031002 (2017).
121. H. Hirayama, N. Maeda, S. Fujikawa, S. Toyoda, and N. Kamata, "Recent progress and future prospects of AlGaN-based high-efficiency DUV LEDs," Jpn. J. Appl. Phys. **53**, 100209 (2014).
122. J. R. Grandusky, J. F. Chen, S. R. Gibb, M. C. Mendrick, C. G. Moe, L. Rodak, G. A. Garrett, M. Wraback, and L. J. Schowalte, "270 nm pseudomorphic UV LEDs with over 60 mW continuous wave output power," Appl. Phys. Express **6**, 032101 (2013).

123. A. Khan, "AlInGaN-based deep ultraviolet light-emitting diodes and their applications technology," in *CS MANTECH Conference* (2013), Vol. **3**, pp. 41–44.
124. T. Kinoshita, K. Hironaka, T. Obata, T. Nagashima, R. Dalmau, R. Schlesser, B. Moody, J. Q. Xie, S. Inoue, Y. Kumagai, A. Koukitu, and Z. Sitar, "Deep-ultraviolet light-emitting diodes fabricated on AlN substrates prepared by hydride vapor phase epitaxy," Appl. Phys. Express **5**, 122101 (2012).
125. T. Kinoshita, T. Obata, T. Nagashima, H. Yanagi, B. Moody, S. Mita, S. Inoue, Y. Kumagai, A. Koukitu, and Z. Sitar, "Performance and reliability of DUV LEDs fabricated on AlN substrates prepared by hydride vapor phase epitaxy," Appl. Phys. Express **6**, 092103 (2013).
126. C. Pernot, M. Kim, S. Fukahori, T. Inazu, T. Fujita, Y. Nagasawa, A. Hirano, M. Ippommatsu, M. Iwaya, S. Kamiyama, I. Akasaki, and H. Amano, "Improved efficiency of 255–280 nm AlGaN-based light-emitting diodes," Appl. Phys. Express **3**, 061004 (2010).
127. S. Nagai, K. Yamada, A. Hirano, M. Ippommatsu, M. Ito, N. Morishima, K. Aosaki, Y. Honda, H. Amano, and I. Akasaki, "Development of highly durable deep-ultraviolet AlGaN-based LED multichip array with hemispherical encapsulated structures using a selected resin through a detailed feasibility study," Jpn. J. Appl. Phys. **55**, 082101 (2016).
128. A. Fujioka, T. Misaki, T. Murayama, Y. Narukawa, and T. Mukai, "Improvement in output power of 280-nm deep ultraviolet light-emitting diode by using AlGaN multi quantum wells," Appl. Phys. Express **3**, 041001 (2010).
129. "EpiTop claims DUV LED output record," LED Industry News, 2016, http://www.solidstatelighting.net/epitop-claims-duv-output-record.
130. S. Inoue, N. Tamari, and M. Taniguchi, "150 mW deep-ultraviolet light-emitting diodes with large-area AlN nanophotonic light extraction structure emitting at 265 nm," Appl. Phys. Lett. **110**, 141106 (2017).
131. N. Maeda and H. Hirayama, "Realization of high-efficiency deep-UV LEDs using transparent p-AlGaN contact layer," Phys. Status Solidi C **10**, 1521–1524 (2013).
132. J. F. Chen, J. R. Grandusky, C. G. Moe, M. C. Mendrick, M. Jamil, S. R. Gibb, and L. J. Schowalter, "High power pseudomorphic mid ultraviolet light emitting diodes with improved efficiency and lifetime," Proc. SPIE **8986**, 269–274 (2013).
133. H. Hirayama, T. Yatabe, N. Noguchi, T. Ohashi, and N. Kamata, "231-261 nm AlGaN deep-ultraviolet light realized using a thin quantum well and AlN buffer with reduced threading dislocation density," Appl. Phys. Express **1**, 051101 (2008).
134. H. Hirayama, T. Yatabe, N. Noguchin, and N. Kamata, "Development of 230–270 nm AlGaN-based deep-UV LEDs," Electron. Commun. Jpn. **93**, 24–33 (2010).
135. H. Hirayama, Y. Tsukada, T. Maeda, and N. Kamata, "Marked enhancement in the efficiency of deep-ultraviolet AlGaN light-emitting diodes by using a multiquantum-barrier electron blocking layer," Appl. Phys. Express **3**, 031002 (2010).
136. T. Mino, H. Hirayama, T. Takano, N. Noguchi, and K. Tsubaki, "Highly-uniform 260 nm-band AlGaN-based deep-ultraviolet light-emitting diodes developed by 2-inch × 3 MOVPE system," Phys. Status Solidi C **9**, 749–752 (2012).
137. N. Maeda and H. Hirayama, "Improvement of light-extraction efficiency of deep-UV LEDs using transparent p-AlGaN contact layer," in *Conference on Lasers and Electro-Optics Pacific Rim (CLEO-PR)* (2013), paper WH2-3.
138. W. H. Sun, J. P. Zhang, V. Adivarahan, A. Chitnis, M. Shatalov, S. Wu, V. Mandavilli, J. W. Yang, and M. A. Khan, "AlGaN-based 280 nm light-emitting

diodes with continuous wave powers in excess of 1.5 mW," Appl. Phys. Lett. **85**, 531–533 (2004).
139. J. P. Zhang, X. Hu, Y. Bilenko, J. Deng, A. Lunev, M. S. Shur, R. Gaska, M. Shatalov, J. W. Yang, and M. A. Khan, "AlGaN-based 280 nm light-emitting diodes with continuous-wave power exceeding 1 mW at 25 mA," Appl. Phys. Lett. **85**, 5532–5534 (2004).
140. W. H. Sun, V. Adivarahan, M. Shatalov, Y. Lee, and S. Wu, "Continuous wave milliwatt power AlGaN light emitting diodes at 280 nm," Jpn. J. Appl. Phys. **43**, L1419–L1421 (2004).
141. V. Adivarahan, S. Wu, W. H. Sun, V. Mandavilli, M. S. Shatalov, G. Simin, J. W. Yang, H. P. Maruska, and M. A. Khan, "High-power deep ultraviolet light-emitting diodes based on a micro-pixel design," Appl. Phys. Lett. **85**, 1838–1840 (2004).
142. V. Adivarahan, S. Wu, J. P. Zhang, A. Chitnis, M. Shatalov, V. Mandavilli, R. Gaska, and M. A. Khan, "High-efficiency 269 nm emission deep ultraviolet light-emitting diodes," Appl. Phys. Lett. **84**, 4762–4764 (2004).
143. V. Adivarahan, W. H. Sun, A. Chitnis, M. Shatalov, S. Wu, H. P. Maruska, and M. A. Khan, "250 nm AlGaN light-emitting diodes," Appl. Phys. Lett. **85**, 2175–2177 (2004).
144. H. W. Shin, K. R. Son, and T. G. Kim, "Localized surface plasmon-enhanced light emission using platinum nanorings in deep ultraviolet-emitting AlGaN quantum wells," Opt. Lett. **41**, 88–91 (2016).
145. I. H. Lee, L. W. Jang, and A. Y. Polyakov, "Performance enhancement of GaN-based light emitting diodes by the interaction with localized surface plasmons," Nano Energy **13**, 140–173 (2015).
146. M. Kneissl, T. Kolbe, C. Chua, V. Kueller, N. Lobo, J. Stellmach, A. Knauer, H. Rodriguez, S. Einfeldt, Z. Yang, N. M. Johnson, and M. Weyers, "Advances in group III-nitride-based deep UV light-emitting diode technology," Semicond. Sci. Technol. **26**, 014036 (2010).
147. Y. Shimahara, H. Miyake, K. Hiramatsu, F. Fukuyo, T. Okada, H. Takaoka, and H. Yoshida, "Fabrication of deep-ultraviolet-light-source tube using Si-doped AlGaN," Appl. Phys. Express **4**, 042103 (2011).
148. K. Watanabe, T. Taniguchi, T. Niiyama, K. Miya, and M. Taniguchi, "Far-ultraviolet plane-emission handheld device based on hexagonal boron nitride," Nat. Photonics **3**, 591–594 (2009).
149. O. Takao, G. B. Ryan, K. Ken, F. Mitsuru, and K. Yoichi, "100 mW deep-ultraviolet emission from aluminium-nitride-based quantum wells pumped by an electron beam," Nat. Photonics **4**, 767–770 (2010).
150. T. Matsumoto, S. Iwayama, T. Saito, Y. Kawakami, F. Kubo, and H. Amano, "Handheld deep ultraviolet emission device based on AlN QWs and graphene nanoneedle field emitters," Opt. Express **20**, 24320–24329 (2012).
151. F. Fukuyo, S. Ochiai, H. Miyake, K. Hiramatsu, H. Yoshida, and Y. Kobayashi, "Growth and characterization of AlGaN MQWs for electron-beam target for DUV light sources," Jpn. J. Appl. Phys. **52**, 01AF03 (2013).
152. S. V. Ivanov, V. N. Jmerik, D. V. Nechaev, V. I. Kozlovsky, and M. D. Tiberi, "E-beam pumped mid-UV sources based on MBE-grown AlGaN MQW," Phys. Status Solidi A **212**, 1011–1016 (2015).
153. X. Rong, X. Q. Wang, S. V. Ivanov, X. H. Jiang, G. Chen, P. Wang, W. Y. Wang, C. G. He, T. Wang, T. Schulz, M. Albrecht, V. N. Jmerik, A. A. Toropov, V. V. Ratnikov, V. I. Kozlovsky, V. P. Martovitsky, P. Jin, F. J. Xu, X. L. Yang, Z. X. Qin, W. K. Ge, J. J. Shi, and B. Shen, "High-output-power ultraviolet light source from quasi-2D GaN quantum structure," Adv. Mater. **28**, 7978–7983 (2016).

154. F. Tabataba-Vakili, T. Wunderer, M. Kneissl, Z. H. Yang, M. Teepe, M. Batres, M. Feneberg, B. Vancil, and N. M. Johnson, "Dominance of radiative recombination from electron-beam-pumped deep-UV AlGaN multi-quantum-well heterostructures," Appl. Phys. Lett. **109**, 181105 (2016).
155. M. Premaratne and G. Agrawal, *Light Propagation in Gain Media Optical Amplifiers* (Cambridge University, 2011).
156. G. Agrawal and N. K. Dutta, *Semiconductor Lasers* (Kluwer Academic, 1993).
157. R. Dingle, K. L. Shaklee, R. F. Leheny, and R. B. Zetterstrom, "Stimulated emission and laser action in gallium nitride," Appl. Phys. Lett. **19**, 5–7 (1971).
158. H. Amano, T. Asahi, and I. Akasaki, "Stimulated emission near ultraviolet at room temperature from a GaN film grown on sapphire by MOVPE using an AlN buffer layer," Jpn. J. Appl. Phys. **29**, L205–L206 (1990).
159. M. Shatalov, M. Gaevski, V. Adivarahan, and A. Khan, "Room-temperature stimulated emission from AlN at 214 nm," Jpn. J. Appl. Phys. **45**, L1286–L1288 (2006).
160. H. Amano, M. Kito, K. Hiramatsu, and I. Aksaki, "P-type conduction in Mg-doped GaN treated with low-energy electron beam irradiation (LEEBI)," Jpn. J. Appl. Phys. **28**, L2112–L2114 (1989).
161. S. Nakamura, T. Mukai, M. Senoh, and N. Iwasa, "Thermal annealing effects on p-type Mg-doped GaN films," Jpn. J. Appl. Phys. **31**, L139–L142 (1992).
162. H. Amano, N. Watanabe, N. Koide, and I. Aksaki, "Room-temperature low-threshold surface-stimulated emission by optical pumping from $Al_{0.1}Ga_{0.9}N$/GaN double heterostructure," Jpn. J. Appl. Phys. **32**, L1000–L1002 (1993).
163. T. J. Schmidt, X. H. Yang, W. Shan, J. J. Song, A. Salvador, W. Kim, Ö. Aktas, A. Botchkarev, and H. Morkoç, "Room-temperature stimulated emission in GaN/AlGaN separate confinement heterostructures grown by molecular beam epitaxy," Appl. Phys. Lett. **68**, 1820–1822 (1996).
164. T. Takano, Y. Narita, A. Horiuchi, and H. Kawanishi, "Room-temperature deep-ultraviolet lasing at 241.5 nm of AlGaN multiple-quantum-well laser," Appl. Phys. Lett. **84**, 3567–3569 (2004).
165. M. Kneissl, D. W. Treat, M. Teepe, N. Miyashita, and N. M. Johnson, "Continuous-wave operation of ultraviolet InGaN/InAlGaN multiple-quantum-well laser diodes," Appl. Phys. Lett. **82**, 2386–2388 (2003).
166. S. Masui, Y. Matsuyama, T. Yanamoto, T. Kozaki, S. Nagahama, and T. Mukai, "365 nm ultraviolet laser diodes composed of quaternary AlInGaN alloy," Jpn. J. Appl. Phys. **42**, L1318–L1320 (2003).
167. K. Lida, T. Kawashima, A. Miyazaki, H. Kasugai, S. Mishima, A. Honshio, Y. Miyake, M. Iwaya, S. Kamiyama, H. Amano, and I. Akasaki, "350.9 nm UV laser diode grown on low-dislocation-density AlGaN," Jpn. J. Appl. Phys. **43**, L499–L500 (2004).
168. H. Yoshida, Y. Takagi, M. Kuwabara, H. Amano, and H. Kan, "Entirely crack-free ultraviolet GaN/AlGaN laser diodes grown on 2-in. sapphire substrate," Jpn. J. Appl. Phys. **46**, 5782–5784 (2007).
169. H. Yoshida, Y. Yamashita, M. Kuwabara, and H. Kan, "Demonstration of an ultraviolet 336 nm AlGaN multiple-quantum-well laser diode," Appl. Phys. Lett. **93**, 241106 (2008).
170. H. Yoshida, Y. Yamashita, M. Kuwabara, and H. Kan, "A 342-nm ultraviolet AlGaN multiple-quantum-well laser diode," Nat. Photonics **2**, 551–554 (2008).

171. S. Zhao, X. Liu, S. Y. Woo, J. Kang, G. A. Botton, and Z. Mi, "An electrically injected AlGaN nanowire laser operating in the ultraviolet-C band," Appl. Phys. Lett. **107**, 043101 (2015).
172. K. H. Li, X. Liu, Q. Wang, S. Zhao, and Z. Mi, "Ultralow-threshold electrically injected AlGaN nanowire ultraviolet lasers on Si operating at low temperature," Nat. Nanotechnol. **10**, 140–144 (2015).
173. S. Zhao, S. Y. Woo, M. Bugnet, X. Liu, J. Kang, G. A. Botton, and Z. Mi, "Three-dimensional quantum confinement of charge carriers in self-organized AlGaN nanowires: a viable route to electrically injected deep ultraviolet lasers," Nano Lett. **15**, 7801–7807 (2015).
174. H. Yoshida, M. Kuwabara, Y. Yamashita, Y. Takagi, K. Uchiyama, and H. Kan, "AlGaN-based laser diodes for the short-wavelength ultraviolet region," New J. Phys. **11**, 125013 (2009).
175. Y. Aoki, M. Kuwabara, Y. Yamashita, Y. Takagi, A. Sugiyama, and H. Yoshida, "A 350-nm-band GaN/AlGaN multiple-quantum-well laser diode on bulk GaN," Appl. Phys. Lett. **107**, 151103 (2015).
176. M. Kuwabara, Y. Yamashita, K. Torii, and H. Yoshida, "Laser operation of nitride laser diodes with GaN well layer in 340 nm band," Jpn. J. Appl. Phys. **52**, 8–10 (2013).
177. H. C. Mary, A. A. Andrew, M. A. Andrew, L. S. Michael, and C. C. Karen, "Laser diodes with 353 nm wavelength enabled by reduced-dislocation-density AlGaN templates," Appl. Phys. Express **8**, 112702 (2015).
178. Q. Wang, Y. P. Gong, J. F. Zhang, J. Bai, F. Ranalli, and T. Wang, "Stimulated emission at 340 nm from AlGaN multiple quantum well grown using high temperature AlN buffer technologies on sapphire," Appl. Phys. Lett. **95**, 161904 (2009).
179. M. Kneissl, Z. H. Yang, M. Teepe, and M. J. Noble, "Ultraviolet laser diodes on sapphire and AlN substrates," Proc. SPIE **7230**, 72300E (2009).
180. T. Wunderer, C. L. Chua, Z. H. Yang, J. E. Northrup, N. M. Johnson, G. A. Garrett, H. Shen, and M. Wraback, "Pseudomorphically grown ultraviolet C photopumped lasers on bulk AlN substrates," Appl. Phys. Express **4**, 092101 (2011).
181. T. Wunderer, C. L. Chua, J. E. Northrup, Z. Yang, N. M. Johnson, M. Kneissl, G. A. Garrett, H. Shen, M. Wraback, B. Moody, H. S. Craft, R. Schlesser, R. F. Dalmau, and Z. Sitar, "Optically pumped UV lasers grown on bulk AlN substrates," Phys. Status Solidi C **9**, 822–825 (2012).
182. T. Wunderer, J. E. Northrup, and N. M. Johnson, "AlGaN-based ultraviolet laser diodes," in *III-Nitride Ultraviolet Emitters* (Springer, 2016), Chap. 8, pp. 193–217.
183. J. Q. Xie, S. Mita, Z. Bryan, W. Guo, L. Hussey, B. Moody, R. Schlesser, R. Kirste, M. Gerhold, R. Collazo, and Z. Sitar, "Lasing and longitudinal cavity modes in photo-pumped deep ultraviolet AlGaN heterostructures," Appl. Phys. Lett. **102**, 171102 (2013).
184. M. Martens, F. Mehnke, C. Kuhn, C. Reich, V. Kueller, A. Knauer, C. Netzel, C. Hartmann, J. Wollweber, J. Rass, T. Wernicke, M. Bickermann, M. Weyers, and M. Kneissl, "Performance characteristics of UV-C AlGaN-based lasers grown on sapphire and bulk AlN substrates," IEEE Photon. Technol. Lett. **26**, 342–345 (2014).
185. Z. Lochner, T. T. Kao, Y. S. Liu, X. H. Li, M. M. Satter, S. C. Shen, P. D. Yoder, J. H. Ryou, R. D. Dupuis, Y. Wei, H. Xie, A. Fischer, and F. A. Ponce, "Deep-ultraviolet lasing at 243 nm from photo-pumped AlGaN/AlN heterostructure on AlN substrate," Appl. Phys. Lett. **102**, 101110 (2013).

186. Y. S. Liu, Z. Lochner, T. T. Kao, M. M. Satter, X. H. Li, J. H. Ryou, S. C. Shen, P. D. Yoder, T. Detchprohm, R. D. Dupuis, Y. Wei, H. Xie, A. Fischer, and F. Ponce, "Optically pumped AlGaN quantum-well lasers at sub-250 nm grown by MOCVD on AlN substrates," Phys. Status Solidi C **11**, 258–260 (2014).
187. X. H. Li, T. Detchprohm, T. T. Kao, M. M. Satter, S. C. Shen, P. D. Yoder, R. D. Dupuis, S. Wang, Y. O. Wei, H. Xie, A. M. Fischer, F. A. Ponce, T. Wernicke, C. Reich, M. Martens, and M. Kneissl, "Low-threshold stimulated emission at 249 nm and 256 nm from AlGaN-based multiple-quantum-well lasers grown on sapphire substrates," Appl. Phys. Lett. **105**, 141106 (2014).
188. Y. D. Tian, J. C. Yan, Y. Zhang, X. Chen, Y. N. Guo, P. P. Cong, L. L. Sun, Q. J. Wang, E. Q. Guo, X. C. Wei, J. X. Wang, and J. M. Li, "Stimulated emission at 288 nm from silicon-doped AlGaN-based multiple-quantum-well laser," Opt. Express **23**, 11334–11340 (2015).
189. G. Morthier, "Influence of the carrier density dependence of the absorption on the harmonic distortion in semiconductor lasers," J. Lightwave Technol. **11**, 16–19 (1993).
190. D. Walker, X. Zhang, P. Kung, A. Saxler, S. Javadpour, J. Xu, and M. Razeghi, "AlGaN ultraviolet photoconductors grown on sapphire," Appl. Phys. Lett. **68**, 2100–2101 (1996).
191. B. W. Lim, Q. C. Chen, J. Y. Yang, and M. Asif Khan, "High responsivity intrinsic photoconductors based on $Al_xGa_{1-x}N$," Appl. Phys. Lett. **68**, 3761–3762 (1996).
192. K. H. Lee, P. C. Chang, S. J. Chang, Y. C. Wang, C. L. Yu, and S. L. Wu, "AlGaN/GaN Schottky barrier UV photodetectors with a GaN sandwich layer," IEEE Sens. J. **9**, 814–819 (2009).
193. H. Y. Liu, Y. H. Wang, and W. C. Hsu, "Suppression of dark current on AlGaN/GaN metal-semiconductor-metal photodetectors," IEEE Sens. J. **15**, 5202–5207 (2015).
194. T. Tut, S. Butun, B. Butun, M. Gokkavas, H. B. Yu, and E. Ozbay, "Solar-blind $Al_xGa_{1-x}N$-based avalanche photodiodes," Appl. Phys. Lett. **87**, 223502 (2005).
195. Z. Q. Huang, J. F. Li, W. L. Zhang, and H. Jiang, "AlGaN solar-blind avalanche photodiodes with enhanced multiplication gain using back-illuminated structure," Appl. Phys. Express **6**, 054101 (2013).
196. E. Monroy, F. Calle, E. Munoz, and F. Omnes, "AlGaN metal-semiconductor-metal photodiodes," Appl. Phys. Lett. **74**, 3401–3403 (1999).
197. I. S. Seo, I. H. Lee, Y. J. Park, and C. R. Lee, "Characteristics of UV photodetector fabricated by $Al_{0.3}Ga_{0.7}N$/GaN heterostructure," J. Cryst. Growth **252**, 51–57 (2003).
198. S. Butun, T. Tut, B. Butun, M. Gokkavas, H. B. Yu, and E. Ozbay, "Deep-ultraviolet $Al_{0.75}Ga_{0.25}N$ photodiodes with low cutoff wavelength," Appl. Phys. Lett. **88**, 123503 (2006).
199. S. V. Averine, P. I. Kuznetzov, V. A. Zhitov, and N. V. Alkeev, "Solar-blind MSM-photodetectors based on $Al_xGa_{1-x}N$/GaN heterostructures grown by MOCVD," Solid-State Electron. **52**, 618–624 (2008).
200. P. C. Chang, C. H. Chen, S. J. Chang, Y. K. Su, C. L. Yu, P. C. Chen, and C. H. Wang, "AlGaN/GaN MSM photodetectors with photo-CVD annealed Ni/Au semi-transparent contacts," Semicond. Sci. Technol. **19**, 1354–1357 (2004).
201. M. Brendel, M. Helbling, A. Knigge, F. Brunner, and M. Weyers, "Solar-blind AlGaN MSM photodetectors with 24% external quantum efficiency at 0 V," Electron. Lett. **51**, 1598–1600 (2015).
202. D. B. Li, X. J. Sun, H. Song, Z. M. Li, Y. R. Chen, G. Q. Miao, and H. Jiang, "Influence of threading dislocations on GaN-based metal-semiconductor-metal ultraviolet photodetectors," Appl. Phys. Lett. **98**, 011108 (2011).

203. X. J. Sun, D. B. Li, H. Jiang, Z. M. Li, H. Song, Y. R. Chen, and G. Q. Miao, "Improved performance of GaN metal-semiconductor-metal ultraviolet detectors by depositing SiO_2 nanoparticles on a GaN surface," Appl. Phys. Lett. **98**, 121117 (2011).
204. D. B. Li, X. J. Sun, H. Song, Z. M. Li, H. Jiang, Y. R. Chen, G. Q. Miao, and B. Shen, "Effect of asymmetric Schottky barrier on GaN-based metal-semiconductor-metal ultraviolet detector," Appl. Phys. Lett. **99**, 261102 (2011).
205. X. J. Sun, D. B. Li, Z. M. Li, H. Song, H. Jiang, Y. R. Chen, G. Q. Miao, and Z. W. Zhang, "High spectral response of self-driven GaN-based detectors by controlling the contact barrier height," Sci. Rep. **5**, 16819 (2015).
206. D. B. Li, X. J. Sun, H. Song, Z. M. Li, Y. R. Chen, H. Jiang, and G. Q. Miao, "Realization of a high-performance GaN UV detector by nanoplasmonic enhancement," Adv. Mater. **24**, 845–849 (2012).
207. G. H. Bao, D. B. Li, X. J. Sun, M. M. Jiang, Z. M. Li, H. Song, H. Jiang, Y. R. Chen, G. Q. Miao, and Z. W. Zhang, "Enhanced spectral response of an AlGaN-based solar-blind ultraviolet photodetector with Al nanoparticles," Opt. Express **22**, 24286–24293 (2014).
208. D. B. Li, X. J. Sun, Y. P. Jia, M. I. Stockman, H. P. Paudel, H. Song, H. Jiang, and Z. M. Li, "Direct observation of localized surface plasmon field enhancement by Kelvin probe force microscopy," Light Sci. Appl. **6**, e17038 (2017).
209. E. Monroy, M. Hamilton, D. Walker, P. Kung, F. J. Sánchez, and M. Razeghi, "High-quality visible-blind AlGaN *p-i-n* photodiodes," Appl. Phys. Lett. **74**, 1171–1173 (1999).
210. D. Walker, V. Kumar, K. Mi, P. Sandvik, P. Kung, X. H. Zhang, and M. Razeghi, "Solar-blind AlGaN photodiodes with very low cutoff wavelength," Appl. Phys. Lett. **76**, 403–405 (2000).
211. R. McClintock, A. Yasan, K. Mayes, D. Shiell, S. R. Darvish, P. Kung, and M. Razeghi, "High quantum efficiency AlGaN solar-blind pin photodiodes," Appl. Phys. Lett. **84**, 1248–1250 (2004).
212. E. Cicek, R. McClintock, C. Y. Cho, B. Rahnema, and M. Razeghi, "$Al_xGa_{1-x}N$-based back-illuminated solar-blind photodetectors with external quantum efficiency of 89%," Appl. Phys. Lett. **103**, 191108 (2013).
213. A. Osinsky, M. S. Shur, R. Gaska, and Q. Chen, "Avalanche breakdown and breakdown luminescence in p-π-n GaN diodes," Electron. Lett. **34**, 691–692 (1998).
214. R. McClintock and M. Razeghi, "Ultraviolet avalanche photodiodes," Proc. SPIE **9555**, 95550B (2015).
215. R. McClintock, A. Yasan, K. Minder, P. Kung, and M. Razeghi, "Avalanche multiplication in AlGaN based solar-blind photodetectors," Appl. Phys. Lett. **87**, 241123 (2005).
216. T. Tut, M. Gokkavas, A. Inal, and E. Ozbay, "$Al_xGa_{1-x}N$-based avalanche photodiodes with high reproducible avalanche gain," Appl. Phys. Lett. **90**, 163506 (2007).
217. L. Sun, J. L. Chen, J. F. Li, and H. Jiang, "AlGaN solar-blind avalanche photodiodes with high multiplication gain," Appl. Phys. Lett. **97**, 191103 (2010).
218. Y. Huang, D. J. Chen, H. Lu, K. X. Dong, R. Zhang, Y. D. Zheng, L. Li, and Z. H. Li, "Back-illuminated separate absorption and multiplication AlGaN solar-blind avalanche photodiodes," Appl. Phys. Lett. **101**, 253516 (2012).
219. M. J. Hou, Z. X. Qin, C. G. He, L. S. Wei, F. J. Xu, X. Q. Wang, and B. Shen, "Study on AlGaN P-I-N-I-N solar-blind avalanche photodiodes with

$Al_{0.45}Ga_{0.55}N$ multiplication layer," Electron. Mater. Lett. **11**, 1053–1058 (2015).
220. X. D. Wang, X. Y. Chen, L. W. Hou, B. B. Wang, W. Xie, and M. Pan, "Role of n-type AlGaN layer in photo response mechanism for separate absorption and multiplication (SAM) GaN/AlGaN avalanche photodiode," Opt. Quantum Electron. **47**, 1357–1365 (2015).
221. L. L. Gao, "Investigation of back-illuminated AlGaN avalanche photodiodes with p-type graded $Al_xGa_{1-x}N$ layer," Opt. Quantum Electron. **47**, 1933–1940 (2015).
222. Z. G. Shao, D. J. Chen, H. Lu, R. Zhang, D. P. Cao, W. J. Luo, Y. D. Zheng, L. Li, and Z. H. Li, "High-gain AlGaN solar-blind avalanche photodiodes," IEEE Electron Device Lett. **35**, 372–374 (2014).
223. J. Kim, M. H. Ji, T. Detchprohm, J. H. Ryou, R. D. Dupuis, A. K. Sood, and N. K. Dhar, "$Al_xGa_{1-x}N$ ultraviolet avalanche photodiodes with avalanche gain greater than 10^5," IEEE Photon. Technol. Lett. **27**, 642–645 (2015).
224. H. L. Wu, W. C. Wu, H. X. Zhang, Y. D. Chen, Z. S. Wu, G. Wang, and H. Jiang, "All AlGaN epitaxial structure solar-blind avalanche photodiodes with high efficiency and high gain," Appl. Phys. Express **9**, 052103 (2016).
225. R. McClintock, E. Cicek, Z. Vashaei, C. Bayram, M. Razeghi, and M. P. Ulmer, "III-nitride-based avalanche photo detectors," Proc. SPIE **7780**, 77801B (2010).
226. E. Bellotti and F. Bertazzi, "A numerical study of carrier impact ionization in $Al_xGa_{1-x}N$," J. Appl. Phys. **111**, 103711 (2012).
227. Q. G. Zhou, D. C. McIntosh, Z. W. Lu, J. C. Campbell, A. V. Sampath, H. Shen, and M. Wraback, "GaN/SiC avalanche photodiodes," Appl. Phys. Lett. **99**, 131110 (2011).
228. A. V. Sampath, R. W. Enck, C. S. Gallinat, H. Shen, and M. Wraback, "III-nitride/SiC avalanche photodetectors for enabling compact biological agent identification and detection," Proc. SPIE **8376**, 837600 (2012).
229. J. Miragliotta, D. K. Wickenden, T. J. Kistenmacher, and W. A. Bryden, "Linear- and nonlinear-optical properties of GaN thin films," J. Opt. Soc. Am. B **10**, 1447–1456 (1993).
230. C. K. Sun, S. W. Chu, S. P. Tai, S. Keller, U. K. Mishra, and S. P. Denbaars, "Scanning second-harmonic/third-harmonic generation microscopy of gallium nitride," Appl. Phys. Lett. **77**, 2331–2333 (2000).
231. J. L. P. Hughes, Y. Wang, and J. E. Sipe, "Calculation of linear and second-order optical response in wurtzite GaN and AlN," Phys. Rev. B **55**, 13630–13640 (1997).
232. P. Srivastava and S. Singh, "Linear and second-order optical response of different GaN nanowires," Physica E **40**, 2742–2746 (2008).
233. B. Taheri, J. Hays, J. J. Song, and B. Goldenberg, "Picosecond four-wave-mixing in GaN epilayers at 532 nm," Appl. Phys. Lett. **68**, 587–589 (1996).
234. Y. L. Huang, C. K. Sun, J. C. Liang, S. Keller, M. P. Mack, U. K. Mishra, and S. P. DenBaars, "Femtosecond Z-scan measurement of GaN," Appl. Phys. Lett. **75**, 3524–3526 (1999).
235. E. Fazio, A. Passaseo, M. Alonzo, A. Belardini, C. Sibilia, M. C. Larciprete, and M. Bertolotti, "Measurement of pure Kerr nonlinearity in GaN thin films at 800 nm by means of eclipsing Z-scan experiments," J. Opt. A **899**, L3–L4 (2007).
236. S. Krishnamurthy, K. Nashold, and A. Sher, "Two-photon absorption in GaN, GaInN, and GaAlN alloys," Appl. Phys. Lett. **77**, 355–357 (2000).
237. C. K. Sun, J. C. Liang, J. C. Wang, and F. J. Kao, "Two-photon absorption study of GaN," Appl. Phys. Lett. **76**, 439–441 (2000).

238. V. Pačebutas, A. Stalnionis, A. Krotkus, T. Suski, P. Perlin, and M. Leszczynski, "Picosecond *Z*-scan measurements on bulk GaN crystals," Appl. Phys. Lett. **78**, 4118–4120 (2001).
239. V. Pačebutas, A. Krotkus, T. Suski, P. Perlin, and M. Leszczynski, "Photoconductive Z-scan measurement of multiphoton absorption in GaN," J. Appl. Phys. **92**, 6930–6932 (2002).
240. Y. Toda, T. Matsubara, R. Morita, M. Yamashita, K. Hoshino, T. Someya, and Y. Arakawa, "Two-photon absorption and multiphoton-induced photoluminescence of bulk GaN excited below the middle of the band gap," Appl. Phys. Lett. **82**, 4714–4716 (2003).
241. E. Kioupakis, P. Rinke, A. Schleife, F. Bechstedt, and C. G. Van de Walle, "Free-carrier absorption in nitrides from first principles," Phys. Rev. B **81**, 241201 (2010).
242. D. Tonova, A. Paneva, and B. Pantchev, "Determination of refractive index profiles of gradient optical waveguides by ellipsometry," Opt. Commun. **150**, 121–125 (1998).
243. P. Chen, Y. H. Zuo, X. G. Tu, D. J. Cai, S. P. Li, J. Y. Kang, Y. D. Yu, J. Z. Yu, and Q. M. Wang, "Interaction between the intrinsic second- and third-order optical fields in an $Al_{0.53}Ga_{0.47}N$/GaN heterostructure," Appl. Phys. Lett. **92**, 161112 (2008).
244. W. Jiang, Y. Wu, W. Lin, S. Li, and J. Kang, "Electro-optic coefficient enhancement of $Al_xGa_{1-x}N$ via multiple field modulations," ACS Appl. Mater. Interfaces **7**, 17707–17712 (2015).
245. W. Lin, W. Jiang, N. Gao, D. J. Cai, S. P. Li, and J. Y. Kang, "Optical isotropization of anisotropic wurtzite Al-rich AlGaN via asymmetric modulation with ultrathin $(GaN)_m/(AlN)_n$ superlattices," Laser Photon. Rev. **7**, 572–579 (2013).
246. F. Wu, W. Tian, J. Zhang, S. Wang, Q. X. Wan, J. N. Dai, Z. H. Wu, J. T. Xu, X. Y. Li, Y. Y. Fang, and C. Q. Chen, "Double-resonance enhanced intersubband second-order nonlinear optical susceptibilities in GaN/AlGaN step quantum wells," Opt. Express **22**, 14212–14220 (2014).
247. S. E. Miller, "Integrated optics: an introduction," Bell Labs Tech. J. **48**, 2059–2069 (1969).
248. X. F. Chen and T. Song, "Research progress of photonic integrated circuits," Telecommun. Sci. **31**, 2015282 (2015).
249. M. Soltani, R. Soref, T. Palacios, and D. Englund, "AlGaN/AlN integrated photonics platform for the ultraviolet and visible spectral range," Opt. Express **24**, 25415–25423 (2016).
250. K. C. Zeng, L. Dai, J. Y. Lin, and H. X. Jiang, "Optical resonance modes in InGaN/GaN multiple-quantum-well microring cavities," Appl. Phys. Lett. **75**, 2563–2565 (1999).
251. T. N. Oder, J. Shakya, J. Y. Lin, and H. X. Jiang, "III-nitride photonic crystals," Appl. Phys. Lett. **83**, 1231–1233 (2003).
252. N. V. Trivino, M. Minkov, G. Urbinati, M. Galli, J. F. Carlin, R. Butte, V. Savona, and N. Grandjean, "Gallium nitride L3 photonic crystal cavities with an average quality factor of 16 900 in the near infrared," Appl. Phys. Lett. **105**, 231119 (2014).
253. T. T. Wu, S. Y. Lo, H. M. Huang, C. W. Tsao, T. C. Lu, and S. C. Wang, "High quality factor nonpolar GaN photonic crystal nanocavities," Appl. Phys. Lett. **102**, 191116 (2013).
254. A. W. Bruch, C. Xiong, B. Leung, M. Poot, J. Han, and H. X. Tang, "Broadband nanophotonic waveguides and resonators based on epitaxial GaN thin films," Appl. Phys. Lett. **107**, 141113 (2015).

255. I. Roland, Y. Zeng, X. Checoury, M. El Kurdi, S. Sauvage, C. Brimont, T. Guillet, B. Gayral, M. Gromovyi, J. Y. Duboz, F. Semond, M. P. de Micheli, and P. Boucaud, "Near-infrared III-nitride-on-silicon nanophotonic platform with microdisk resonators," Opt. Express **24**, 9602–9610 (2016).
256. C. Xiong, W. Pernice, K. K. Ryu, C. Schuck, K. Y. Fong, T. Palacios, and H. X. Tang, "Integrated GaN photonic circuits on silicon (100) for second harmonic generation," Opt. Express **19**, 10462–10470 (2011).
257. B. Thubthimthong, T. Sasaki, and K. Hane, "Asymmetrically and vertically coupled hybrid Si/GaN microring resonators for on-chip optical interconnects," IEEE Photon. J. **7**, 7801511 (2015).
258. X. Li, G. Y. Zhu, X. M. Gao, D. Bai, X. M. Huang, X. Cao, H. B. Zhu, K. Hane, and Y. J. Wang, "Suspended p–n junction InGaN/GaN multiple-quantum-well device with selectable functionality," IEEE Photon. J. **7**, 2701407 (2015).
259. W. Cai, Y. Yang, X. Gao, J. Yuan, W. Yuan, H. Zhu, and Y. Wang, "On-chip integration of suspended InGaN/GaN multiple-quantum-well devices with versatile functionalities," Opt. Express **24**, 6004–6010 (2016).
260. Y. Yang, J. Yuan, Y. Li, X. Gao, and Y. Wang, "On-chip integration for in-plane video transmission using visible light," Proc. SPIE **10019**, 1001912 (2016).
261. M. Tchernycheva, A. Messanvi, A. de Luna Bugallo, G. Jacopin, P. Lavenus, L. Rigutti, H. Zhang, Y. Halioua, F. H. Julien, J. Eymery, and C. Durand, "Integrated photonic platform based on InGaN/GaN nanowire emitters and detectors," Nano Lett. **14**, 3515–3520 (2014).
262. Y. Dong, B. Tian, T. J. Kempa, and C. M. Lieber, "Coaxial group III—nitride nanowire photovoltaics," Nano Lett. **9**, 2183–2187 (2009).
263. M. D. Brubaker, P. T. Blanchard, J. B. Schlager, A. W. Sanders, A. Roshko, S. M. Duff, J. M. Gray, V. M. Bright, N. A. Sanford, and K. A. Bertness, "On-chip optical interconnects made with gallium nitride nanowires," Nano Lett. **13**, 374–377 (2013).
264. C. Xiong, W. H. Pernice, and H. X. Tang, "Low-loss, silicon integrated, aluminum nitride photonic circuits and their use for electro-optic signal processing," Nano Lett. **12**, 3562–3568 (2012).
265. W. H. Pernice, C. Xiong, and H. X. Tang, "High Q micro-ring resonators fabricated from polycrystalline aluminum nitride films for near infrared and visible photonics," Opt. Express **20**, 12261–12269 (2012).
266. H. Jung, C. Xiong, K. Y. Fong, X. Zhang, and H. X. Tang, "Optical frequency comb generation from aluminum nitride microring resonator," Opt. Lett. **38**, 2810–2813 (2103).
267. H. Jung, R. Stoll, X. Guo, D. Fischer, and H. X. Tang, "Green, red, and IR frequency comb line generation from single IR pump in AlN microring resonator," Optica **1**, 396–399 (2014).
268. X. W. Liu, C. Z. Sun, B. Xiong, J. Wang, L. Wang, Y. J. Han, Z. B. Hao, H. T. Li, Y. Luo, J. C. Yan, T. B. Wei, Y. Zhang, and J. X. Wang, "Broadband tunable microwave photonic phase shifter with low RF power variation in a high-Q AlN microring," Opt. Lett. **41**, 3599–3602 (2016).
269. X. W. Liu, C. Z. Sun, B. Xiong, L. Wang, J. Wang, Y. J. Han, Z. B. Hao, H. T. Li, Y. Luo, J. C. Yan, T. B. Wei, Y. Zhang, and J. X. Wang, "Aluminum nitride-on-sapphire platform for integrated high-Q microresonators," Opt. Express **25**, 587–594 (2017).
270. D. F. Leonardis, R. A. Soref, M. Soltani, and V. M. Passaro, "Broadband biphoton generation and statistics of quantum light in the UV-visible range in an AlGaN microring resonator," Sci. Rep. **7**, 11387 (2017).

271. A. W. Bruch, K. Xiong, H. Jung, X. Guo, C. Zhang, J. Han, and H. X. Tang, "Electrochemically sliced low loss AlGaN optical microresonators," Appl. Phys. Lett. **110**, 021111 (2017).

Dabing Li is a professor at Changchun Institute of Optics, Fine Mechanics and Physics (CIOMP), Chinese Academy of Sciences (CAS). He received his Ph.D. in materials physics and chemistry from the Institute of Semiconductor of CAS, University of Chinese Academy of Sciences in 2004. From 2004 to 2008, he worked as a postdoctoral associate and JSPS fellow for foreigner at the Department of Electrical and Electronic Engineering, Mie University, Japan. In 2008, he joined in CIOMP, CAS. His research interests focus on materials and devices of III-nitrides. He is a senior member of the Optical Society of America. He was awarded the "Lu Jia-Xi Young Talent Award" from CAS (2009), Excellent Young Scientists Fund from the NSFC (2013), and National Science Fund for Distinguished Young Scholars (2017).

Ke Jiang received his bachelor's degree from Xiamen University, Xiamen, China, in 2014. From 2014 until now, he has studied as a doctoral course student at State Key Laboratory of Luminescence and Applications, CIOMP, CAS. His current research is related to AlGaN ultraviolet photodetectors.

Xiaojuan Sun is an associate professor at CIOMP, CAS. She received her bachelor's degree and master's degree from Dalian University of Technology, Dalian, China, in 2004 and 2007, respectively. From 2007 until now, she has worked at the Changchun Institute of Optics, Fine Mechanics and Physics (CIOMP), Chinese Academy of Sciences (CAS). In 2012, she received her Ph.D. from CIOMP, CAS. From 2015 to 2016, she worked at Georgia State University as a visiting scholar. Her research is in the field of AlGaN materials growth and their optoelectronic devices.

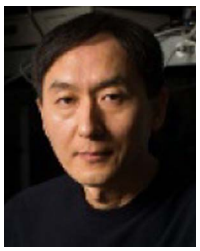

Chunlei Guo is a professor at the Institute of Optics at the University of Rochester and Changchun Institute of Optics, Fine Mechanics, and Physics. His research is in the area of laser–matter interactions and photonics. He received his BS from Changchun Institute of Optics and Fine Mechanics and Ph.D. from University of Connecticut, followed by postdoctoral training at Los Alamos National Laboratory before he joined Rochester as a faculty member in 2001. He is a fellow of the American Physical Society and Optical Society of America. Currently, he serves as the editor-in-chief for the CRC Handbook of Laser Technology and Applications (2nd Edition).